Coupled dynamics of colloids and immiscible fluids in porous media

Joanna Schneider

a dissertation
presented to the faculty
of princeton university
in candidacy for the degree
of Doctor of Philosophy

recommended for acceptance
by the Department of
Chemical and Biological Engineering

Advisers: Sujit S. Datta, Rodney D. Priestley

May 2023

© Copyright by Joanna Schneider, 2023. All rights reserved.

Abstract

A wide array of processes, from contaminant transport to carbon dioxide sequestration and groundwater remediation, involve interactions between colloidal particles and immiscible fluids. In these applications, colloidal particles and immiscible fluids must navigate complex, tortuous, three-dimensional (3D) pore spaces, such as in soils and rigid rocks. For simplicity, researchers typically study these interactions using individual particles in idealized geometries. While these studies help to elucidate the physics underlying these interactions—including colloidal interactions, hydrodynamics, and capillarity—in many cases, concentrated deposition of colloids and complex pore space geometries give rise to phenomena that cannot be described by simplified models. In this dissertation, I address this gap in knowledge by studying how colloidal deposition impacts immiscible fluid flow and mobilization in porous media by integrating experiments, simulations, and theory. First, by injecting colloids into a model porous medium containing trapped immiscible fluid droplets, I show that colloidal deposition can be controlled and harnessed to enhance removal of trapped droplets by reducing the medium's overall permeability. Building upon the theoretical framework developed to describe immiscible fluid mobilization, I next explore how structural heterogeneity within a porous medium may impact the accuracy of those predictions. Then, using this foundational understanding of colloidal flows and immiscible fluid trapping, I develop pore scale experiments and simulations that describe how immiscible fluid flow is altered by the ability of fluid-fluid interfaces to erode and redeposit colloidal particles. I show that colloidal particles can be driven to fluid interfaces by capillary forces, which results in the emergence of a new immiscible fluid flow regime and expands upon traditional models to describe immiscible fluid flow. Having extensively explored the interactions between colloids and immiscible fluids in porous media, I fabricate hybrid colloidal particles containing catalytically active metal nanoparticles and an organic, polymeric support, demonstrating a tunable method to produce hybrid nanoparticles for groundwater remediation. Finally, my ongoing work discusses how to study the efficacy of reactive particles for immiscible contaminant degradation in 3D porous media. These results present a unified chemical and physical approach to understanding how colloids interact with and impact immiscible fluid flow in porous media.

Contents

Abstract **iii**

1 Introduction **5**
- 1.1 Mechanisms of colloid-enhanced immiscible fluid mobilization 8
- 1.2 Novel nanomaterials and their limitations 12
- 1.3 Fabrication of complex colloids 14
- 1.4 Colloidal transport in 3D porous media 17

2 Harnessing colloidal deposition for trapped fluid mobilization **22**
- 2.1 Connecting pore scale deposition & macroscopic colloidal transport 25
- 2.2 Implications of dynamic deposition & erosion 30
- 2.3 Establishing an initial trapped fluid configuration 32
- 2.4 Enhanced mobilization of trapped oil by colloidal particles 36
- 2.5 Characteristics & features of colloidal deposition 37
- 2.6 Permeability reduction by colloidal deposition 41
- 2.7 Developing a model for deposition-induced mobilization 44
- 2.8 Implications of deposition-enhanced mobilization 50
- 2.9 Conclusions 54
- 2.10 Supplementary Movie Captions 55

3 Improving fluid mobilization predictions in stratified porous media **57**
- 3.1 Developing criteria for stratum-dependent mobilization 60
- 3.2 Comparison to averaged approximation of mobilization 64
- 3.3 Calculating residual oil saturation 66
- 3.4 Impacts of considering individual stratum properties 70
- 3.5 Conclusions 77

4 Visualizing capillarity-driven colloidal adsorption **79**
- 4.1 Materials and Methods 81

4.2 Interactions between deposited particles and immiscible fluids 85
4.3 Mechanism of adsorption to immiscible fluid interfaces 88
4.4 Dense deposition alters interfacial rheology 95
4.5 Conclusions and next steps 96
4.6 Supplementary Movie Captions 98

5 Predicting immiscible fluid flow in erodible porous media **103**
5.1 Model development 106
5.2 Model implementation 108
5.3 New drainage behaviors due to solid erosion & deposition 110
5.4 Origins of these new drainage behaviors 111
5.5 A unified state diagram for drainage in an erodible porous medium 115
5.6 Supplementary Information 116
5.7 Supplementary Movie Captions 119

6 Designing hybrid nanoparticles for groundwater remediation **121**
6.1 Materials and Methods 124
6.2 Gold nanocatalyst adsorption to polystyrene nanoparticles 126
6.3 Diffusion-based surface aggregation of gold nanocatalysts 131
6.4 Emergence of dispersed and internalized morphologies 138
6.5 Tuning catalytic reactions using hybrid nanoparticles 144
6.6 Conclusions 146
6.7 Supplementary Information 147

7 Outlook and future directions **149**
7.1 Immiscible fluid-enhanced erosion in 3D porous media 151
7.2 Removal and degradation of trapped immiscible fluids 157

Appendix A Relevant parameters **159**
A.1 Key dimensionless quantities 160

References **188**

Citations to Previously Published Work

Section 1.4 of Chapter 1 is based in part on a published textbook chapter by Navid Bizmark, Joanna Schneider, Emily de Jong, and Sujit S. Datta. Chapter 9: Transport of Polymer Colloids in Porous Media. In *Polymer Colloids: Formation, Characterization and Applications*, pages 289–321. Royal Society of Chemistry, 2020.[1]

Sections 2.1–2.2 of Chapter 2 have been adapted from published work by Navid Bizmark, Joanna Schneider, Rodney D. Priestley, and Sujit S. Datta. Multiscale dynamics of colloidal deposition and erosion in porous media. *Science Advances*, 6 (46):eabc2530, 2020.[2] **Author Contributions:** N.B. and S.S.D. designed the experiments; N.B. performed experiments; N.B., J.S., and S.S.D. analyzed the data; N.B. and S.S.D. developed the theoretical model; S.S.D. designed and supervised the overall project. All authors discussed the results and wrote the manuscript.

Sections 2.3–2.9 of Chapter 2 been adapted from published work by Joanna Schneider, Rodney D. Priestley, and Sujit S. Datta. Using colloidal deposition to mobilize immiscible fluids from porous media. *Physical Review Fluids*, 6 (1):014001, 2021.[3] **Author Contributions:** J.S. and S.S.D. designed the experiments; J.S. performed all experiments; J.S. and S.S.D. analyzed the data and developed/implemented the theoretical model; S.S.D. designed and supervised the overall project. All authors discussed the results and wrote the manuscript.

Chapter 3 has been adapted from unpublished work by Joanna Schneider, Nancy B. Lu, and Sujit S. Datta. **Author Contributions:** J.S. and N.B.L. developed the theory; J.S. analyzed the data and implemented the theoretical model. S.S.D. designed and supervised the overall project. All authors discussed the results and wrote the manuscript.

Chapter 4 has been adapted from unpublished work by Joanna Schneider and Sujit S. Datta. **Author Contributions:** J.S. and S.S.D. designed the experiments; J.S. performed all experiments; J.S. and S.S.D. analyzed the data. S.S.D. designed and supervised the overall project. J.S. and S.S.D. discussed the results and wrote the preliminary manuscript.

Chapter 5 has been adapted from a pre-print by Joanna Schneider, Christopher A. Browne, Malcolm Slutzky, Cecilia A. Quirk, Daniel B. Amchin, and Sujit S. Datta. Fluid drainage in erodible porous media. *arXiv pre-print*, arXiv:2303.01260, 2023.[4] **Author Contribu-**

tions: J.S., C.A.B., and D.B.A. designed simulations; J.S., M.S., and C.A.Q. performed all simulations; J.S., C.A.B., and S.S.D. designed and performed the theoretical analysis; S.S.D. designed and supervised the overall project. All authors discussed the results. J.S. and S.S.D. wrote the manuscript.

Chapter 6 has been adapted from published work by Joanna Schneider, Jason X. Liu, Victoria E. Lee, Robert K. Prud'homme, Sujit S. Datta, and Rodney D. Priestley. Tuning morphologies and reactivities of hybrid organic–inorganic nanoparticles. *ACS Nano*, 16 (10):16133-16142, 2022.[5] **Author Contributions:** J.S., V.E.L., and R.D.P. designed the experiments; J.S. and J.X.L. performed all experiments; J.S. analyzed the data; R.D.P. designed and supervised the overall project. All authors discussed the results. J.S., J.X.L., and R.D.P. wrote the manuscript.

Chapter 7 is based on ongoing unpublished work by Joanna Schneider and Sujit S. Datta. **Author Contributions:** J.S. and S.S.D. designed the experiments; J.S. performed preliminary experiments and analysis. S.S.D. designed and supervised the overall project.

All movies can be found online at https://github.com/joannaclaireschneider/dissertation-movies.

Citations to other work not included in this thesis

Christopher A. Browne*, Daniel B. Amchin*, Joanna Schneider*, Sujit S. Datta. Infection percolation: A dynamic network model of disease spreading. *Frontiers in Physics*, 9:645954, 2021.[6] (* denotes co-first authors) **Author Contributions:** C.A.B., D.B.A., and J.S. initiated the project. D.B.A. designed simulations. C.A.B. and J.S. performed all simulations. S.S.D. designed and performed the theoretical analysis and supervised the overall project. All authors designed the overall project, analyzed the data, discussed the results and implications, and wrote the manuscript.

To Samuel Schaffter, who taught me how to ask the right questions

Acknowledgments

The number of people who have played a role in my successful completion of this degree is not small. I feel lucky to have been pushed out of my comfort zone in so many ways over the past few years. I have also been provided with a safe space both to succeed and to fail, but most importantly, I have had the opportunity to be a part of an incredible community. I attribute all of this and more to Sujit Datta, who has always been an exemplary advisor, mentor, advocate, and friend. Sujit—you set the bar for every metric of a good person. I am honored that you chose me to help create the bones of this incredible lab.

To Rebecca Schulman and Sam Schaffter, without you, I would not have made it to Princeton. Thank you for your mentorship and advocacy. Sam, thank you for demonstrating how to do science in the most beautiful way. You have remained a role model for me all this time.

To Sujit and Rod, for allowing me to be your first co-advised graduate student and for taking a chance on a complicated project. You have both cultivated caring, compassionate, and bright research environments. Rod, thank you for letting me think big picture with you early on and for always providing a supportive space when I doubted myself. Sujit, thank you for being on the ground with me, for knowing when I needed help and when I needed to go it alone. Thank you both for always letting my passions guide the next project. Being co-advised wasn't always easy, but the lessons I have taken away have made it worth it.

To Ian Bourg and Howard Stone, for serving on my thesis committee during my time at Princeton, for always being available to meet about research or career advice, and for never failing to ask me a question I hadn't thought of before. Thank you for keeping me on my toes and for guiding my work in new directions. You are both evidence of the kind, collaborative, and inquisitive nature of the research community at Princeton.

To John Schreiber and Nan Yao in the Imaging & Analysis Center, for the invaluable service you provide to Princeton and the mountain of help you provided me as I learned how to operate a transmission electron microscope. To John, for all of the times something went awry, thank you for always finding a minute to help, even when you were in high demand.

To Karen Oliver, Jacqueline Armstrong, Mini Thomas, Phoebe Rivera, Pam Raney, Lisa Kraut, and Patti West. To Karen, I will miss you so much. You are an incredible source of knowledge and support in the department and you always say the right thing. To Jackie,

for always helping me find Rod in a pinch and for managing his schedule with grace and compassion for the needs of his students. To Mini and Phoebe, my newest friends—it has been such a joy getting to know both of you this year. And of course, to Pam, Lisa, and Patti: thank you so much for countless reimbursements, orders placed, and questions answered.

To Emre Turkoz, Billy Landuyt, and Wenting Xiao at ExxonMobil. Thank you for an incredible summer internship experience and for helping me to enter my final year of graduate school with clarity. Billy, thank you for teaching me that mentors exist outside of academia and for always encouraging me to think deeply about myself and my goals.

To every person who has passed through the Priestley and Datta labs during my time at Princeton. Thank you all for your incredible intelligence and support, and for being a part of this beautiful, complicated, stressful, thrilling experience. In particular, thank you to Daniel Amchin, Navid Bizmark, Christopher Browne, Nicholas Caggiano, Emily Chen, Sebastian Gonzalez La Corte, Anna Hancock, Victoria Lee, Jason Liu, Jean-François Louf, Nancy Lu, Shawn Maguire, Galen Mandes, Allyson McGaughey, Jenna Moore-Ott, Katie Randazzo, and Yejoon Seo for endless help (and refuge) from experiments. Chris and Emily, thank you for providing the support system one can only get from sharing the plight of air bubbles and pressure transducers. To my previous undergraduates, Kimberly Lu, Cecilia Quirk, Malcolm Slutzky, and Charlotte Tausche, thank you for teaching me how to teach and for sticking with me. Finally, to Sanjana Kamath, I hope you find joy and support in this amazing, ever-evolving group of people in the same way I did. I am excited to see all that you do.

To my cohort for being the best cohort in CBE. In particular, to Avery Agles, Alex Johnson, and Christopher Ushay. On the Border will never know a squad like ours again. And to Alex and Caroline—thank you for letting me invite myself over for chili every so often.

To what can only be described as the squad: Charles Argon, Isaac Breinyn, Christopher Browne, Drew Carson, Emily Chen, Jordana Composto, Jean-François Louf, Galen Mandes, & Evan Underhill. This group has changed countless times over the years, but 159 Nassau St will forever hold a special place in my heart: the best place to puzzle, grill, and make pasta beans. To Christopher Browne, I have always believed that our closest friends should be the people we admire most. That has never been truer than it has been with you.

To Michael Milizzo, you make me feel like I can do anything. You make me laugh harder than anyone. You are the kindest, most thoughtful, and compassionate person I know. Thank you for your endless support and patience. You teach me every day how to be a better person, but I am a work in progress. Thank you for helping me slow down and for feeding me grilled cheese. Most importantly, thank you for loving the cat. I love you more than you know.

And finally, to my mother, Rose Schneider, and sisters, Felicia & Emily Schneider. Thank you for always believing in my ability to see things through. Thank you for your unconditional love and for always being my *loudest* cheerleaders. To my mother, thank you for every sacrifice. You make the impossible possible. I hope to be half the woman you are one day.

So look see the days, the endless coloured ways,

And go play the game that you learnt

From the morning.

Nick Drake, From The Morning



Preface

The definition of a successful PhD will vary depending on the person you ask. To me, that definition has always been strongly linked with developing an ability to ask the right questions when you don't know an answer. This body of work shows my journey in learning how to ask those questions. While it was by no means a linear process, it was truly a joy.

No story sits by itself.

Sometimes stories meet at corners and sometimes

they cover one another completely,

like stones beneath a river.

Mitch Albom, The Five People You Meet In Heaven

1

Introduction

Nearly 50% of the United States gets its drinking water from groundwater aquifers. However, this statistic is in sharp conflict with the frequency with which they are contaminated. Approximately 1 in 5 water samples obtained from aquifers contains contaminants in concentrations above the Environmental Protection Agency's (EPA) designated maximum

contaminant levels (MCL). These contaminants take many forms: they can be man-made or naturally occurring, aqueous heavy metals or oils. Nearly 60% of the EPA's designated Superfund sites, which comprise the United States' most severely contaminated waste sites, contain organic or oil-based contaminants, which reflects the challenge of their removal.

Instead of flowing freely, immiscible oil-based contaminants get trapped by capillary forces in the small spaces between the rock grains that comprise our aquifers. Over time, these trapped contaminants leach into flowing water and spread, often long distances away from an initial contaminant plume. To curb the impacts of these contaminants on the water supply, technologies to improve and maintain the quality of our drinking water and agricultural water supplies are in constant use; prior to the 1990s, the dominant technologies were largely "pump & treat" remedies, in which contaminated water would be pumped above ground to physically remove or detoxify contaminants[7]. However, a variety of limitations to using this technology—from costly annual upkeep and maintenance to slow removal rates—has resulted in a push for alternative solutions[8–10].

This search for remedies to mitigate contamination at the source, or without the need for extraction, has led researchers more recently to *in situ* technologies, namely subsurface injection of colloidal nanomaterials (Fig. 1.1). This technique is particularly promising due to the capacity of these materials to travel long distances, pervade small aquifer pore spaces, and degrade contaminants *via* a number of chemical reactions[11–14]. However, most widely used nanomaterials, such as zero valent iron nanoparticles (nZVI) and metal oxides, aggregate over time scales on the order of minutes, reducing their reactivity and mobility in tortuous, confined pore spaces[15–17]. Others, like gold (Au) nanoparticles, are too expensive for widespread use due to the large amounts of material that need to be injected, also preventing

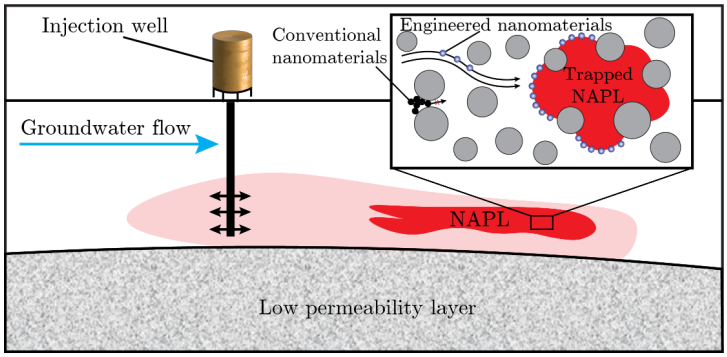


Figure 1.1: Schematic of *in situ* groundwater remediation using colloidal nanomaterials. Additives, such as colloidal nanomaterials, are injected into aquifers through an injection well. Nanomaterials flow from the injection well into contaminated regions, harnessing natural geological flow for transport. Oily, organic contaminants are referred to as non-aqueous phase liquids (NAPLs). The inset shows a NAPL (red) trapped between aquifer grains (gray circles). Conventional nanomaterials (black) often aggregate, preventing their ability to treat trapped NAPLs. We aim to understand what causes conventional nanomaterials to fail in three-dimensional (3D) porous media to inform design of more effective engineered nanomaterials (blue) that minimize aggregation and optimize transport to NAPL-water interfaces.

their widespread implementation [18]. To design more successful nanomaterials, we aim to understand *how* and *why* conventional nanomaterials fail in remediation efforts in real porous media. To accomplish this goal, this dissertation endeavors to provide a deeper understanding of how colloids interact with immiscible fluids and flow through a complex porous medium.

In this dissertation, I draw upon both physical and chemical approaches to aid in removal of trapped immiscible fluids from a porous medium to better understand how colloids may be harnessed to improve processes such as groundwater remediation. Specifically, I show that colloidal particle deposition can be *controlled* and *harnessed* to enhance removal of trapped immiscible fluid droplets from a tortuous, three-dimensional (3D) porous medium by reducing its permeability (Chapter 2). Building upon the theoretical framework developed to describe removal of those trapped droplets, I next explore how structural heterogeneity within a porous medium may impact the accuracy of those predictions (Chapter 3). Using this foundational understanding of colloidal flows and immiscible fluid trapping, I show ex-

perimentally at the pore scale (Chapter 4) and computationally at the macroscale (Chapter 5) how dense, multilayer colloidal deposition impacts immiscible fluid transport, which in turn impacts the resultant deposition within the pore space. Finally, I fabricate hybrid colloidal particles containing catalytically active metal nanoparticles and an organic, polymeric support (Chapter 6) and propose future work that harnesses their ability to treat immiscible contaminants *via* both physical removal and chemical degradation (Chapter 7).

1.1 Mechanisms of colloid-enhanced immiscible fluid mobilization

While groundwater remediation efforts often focus on the development of novel reactive materials to chemically detoxify or degrade contaminants without removing them, these colloids also have rich physical interaction with oil interfaces and pore spaces, which remain poorly characterized. Nevertheless, enhanced oil recovery (EOR) techniques suggest that physical remodeling of pore spaces can markedly alter the mobilization of oil ganglia, or discrete droplets. Like most chemical EOR techniques, nanoparticle EOR is analogous to a process called waterflooding, where water or brine is injected into a porous medium containing trapped oil, referred to as partially saturated porous medium. To further increase recovery, a nanoparticle-laden fluid, termed a nanofluid, is used instead of water. The primary mechanism promoting nanoparticle EOR is hypothesized to be interfacial tension (IFT) reduction, but though wettability alteration and structural disjoining pressure may also play a role.

To study how nanofluids may improve EOR, most studies utilize surface active silica or non-ferrous metal nanoparticles by injecting them into core samples at various concentra-

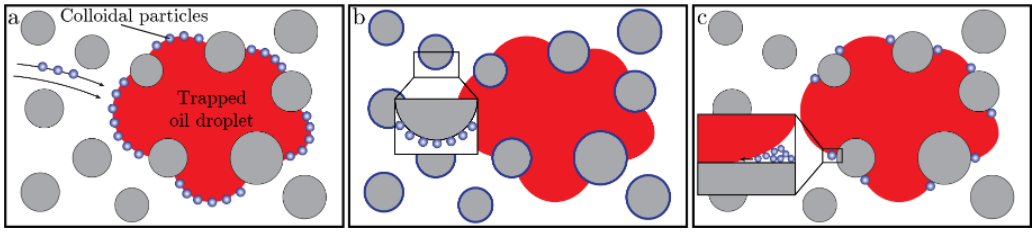


Figure 1.2: Schematics of postulated mobilization mechanisms in colloid enhanced oil recovery (EOR). (a) The mostly commonly hypothesized mobilization mechanism in colloid EOR is interfacial tension reduction, whereby surface active colloidal particles (blue) preferentially localize at oil-water interfaces. The trapped oil droplet is indicated in red and oil reservoir rock grains are represented by gray circles. (b) Wettability alteration likely occurs when colloidal particles deposit on the rock grains of an oil reservoir, effectively changing the chemical properties of rock surfaces. The blue outline on rock grains represents deposition of colloidal particles. The inset shows individual colloidal particles depositing to form a layer with new surface chemistry. (c) A change in the structural disjoining pressure arises when colloidal particles aggregate between the trapped oil droplet and rock grains, represented by colloidal particles at each of these intersections. The inset shows how colloidal particles gather at this interface, moving inward toward the bulk of the droplet to detach it from the solid rock grains.

tions. Surface active particles preferentially localize at immiscible fluid-fluid interfaces owing to their surface chemistry, thereby reducing the interfacial tension and weakening the capillary stresses that keep fluid trapped (Fig. 1.2a). In these studies, IFT reduction is usually reported as the dominant mechanism in trapped oil mobilization[19–25]. Pendant drop tensiometry or drope-shape analysis measures the interfacial tension between the nanofluid and oil; when lower IFT values are reported at the water-oil interface due to the presence of nanoparticles, studies have found that the strength of interfacial forces holding oil in place decreases. In several studies, aluminum or silicon oxides or a mixture thereof have been reported to be the most effective in increasing oil recovery *via* these mechanisms[22–24]. However, when non-surface active particles are injected, IFT reduction is not observed.

Other studies report that wettability alteration of a porous medium, or a reduction in the three-phase contact angle, θ, is the dominating mechanism in nanoparticle EOR (Fig. 1.2b). To reduce θ, the angle between immiscible fluids and the substrate that comprises the porous

medium, particles do not necessarily have to be surface active[26]. In one study, injection of hydrophilic silicon dioxide (SiO_2) nanoparticles promoted the transition of an oil wet system to neutral wet, resulting in increased oil recovery[27]. As the concentration of SiO_2 particles was increased, the wettability index did not change according to an Amott wettability index test, suggesting that this transition is not a strong function of nanofluid concentration. However, when wettability alteration is coupled to IFT reduction, as in the case of surface active SiO_2 particles, oil recovery increased as nanofluid concentration increased. Though it is clear that IFT reduction decreases capillary forces to mobilize oil, it is still unclear why changes in wettability also contribute to enhanced recovery.

Another subtle distinction from IFT reduction alone is a change in the structural disjoining pressure, where nanoparticles form a wedge-shaped film between a trapped oil ganglion and the porous medium (Fig. 1.2c). The disjoining pressure is an osmotic pressure that results from nanoparticles that form this wedge. Wedge formation and subsequent mobilization is a dewetting-type process that is not fully understood, but nanoparticles need not be surface active for these events to take place. However, similar to wettability alteration, the presence of nanoparticles with small contact angles enhances IFT reduction and results in increased disjoining pressures[28]. In one study, a sharp decrease in the three-phase contact angle is attributed to injection of the nanofluid, but the formation of a wedge film causes the disjoining pressure to dominate over IFT reduction and the nanofluid wedge film spread under a small contact angle to increase oil recovery from 17% to 55%[29].

Importantly, all of these mechanisms rely on the ability of colloidal particles to freely move through the heterogeneous pore space: deposition is thought to hinder the ability of particles to localize at target fluid interfaces[15,30], and potentially causes clogging that impedes subse-

quent flow[31–34]. As a result, researchers typically seek to minimize deposition of colloidal particles in porous media—for example, by tuning colloidal interactions or only using low concentrations of particles[35,36]. At high nanoparticle concentrations, studies suggest that adsorption of nanoparticles to the porous medium results in clogging or permeability reduction[33,34,37], which may push oil out by increasing the pressure drop across ganglia according to Darcy's law at a constant volumetric flowrate, Q,

$$\Delta P = -\frac{\mu(Q/A)L}{\kappa k} \tag{1.1}$$

where P is the local pressure in the fluid, μ is the viscosity of the injected fluid, A is the cross-sectional area of the porous medium, L is the ganglion length along the flow direction, κ is the relative permeability of the porous medium due to residual oil trapping, and k is the absolute permeability of the porous medium. The relative permeability, κ, is the result of residual oil trapping and minimizes the space that the flowing fluid can travel through, while the absolute permeability, k, is defined by the geometry of the pore space. Nanoparticle migration and deposition decreases the permeability of a porous medium and the porosity, or void space, φ[33,37]. In one study, the pressure drop across a Berea sandstone core increased suddenly from 20 to 50 kPa during injection of hydrophilic silica nanoparticle suspensions (0.1-0.5 wt%), suggesting that pores in the core sample were rapidly clogged. However, a ten-fold decrease in injection concentration resulted in no visible change in the pressure drop across the core sample, setting forth the possibility that mobilization had been enhanced by flow diversions due to clogging of individual pores without greatly impacting the macroscopic pressure drop[34].

Despite numerous studies of nanoparticle EOR, the primary mechanisms governing oil

mobilization remain highly debated. While IFT reduction is the most common explanation, structural disjoining pressure, changes in wettability, and decreased permeability all provide reasonable explanations for observed EOR. The types of particles used for EOR also complicate the results; silica particles of varying hydrophobicity and surface activity have been studied extensively. However, few studies have imaged *within* a three-dimensional (3D) porous medium to visualize and isolate the mechanisms by which nanoparticles mobilize immiscible fluids in porous media.

1.2 Novel nanomaterials and their limitations

While approaches to immiscible fluid removal in enhanced oil recovery tend to focus on physical mechanisms for removal, groundwater remediation efforts often focus of the development of new nanotechnologies, which focus on chemical mechanisms for removal. In 2003, the total global market for nanotechnology in environmental remediation was only $2.8 million; however, by 2014, this number had increased by a factor of almost 10,000 to $23.4 billion[38], and the market for environmental remediation technologies is expected to continue growing to an estimated $189.1 billion by 2025[39]. With a growing market for engineered nanomaterials, research on metals and metal oxides has revealed their versatility in reduction and adsorption of heavy metals, as well as degradation of organic compounds.

Zero valent iron nanoparticles (nZVI) are of particular interest because they are inexpensive and have the potential to aid in detoxification of a variety of contaminants, including heavy metals, inorganic ions, and halogenated organic compounds[12]. Reactions between

nZVI and As^{3+}, carbon tetrachloride, and trichloroethylene (TCE) are all well understood, in part because of the use of zero valent iron in permeable reactive barriers[40,41]. However, nZVI aggregation due to magnetic attraction between particles and high agglomeration rates prevent their widespread use because they are unable to reach contaminant plumes or trapped contaminants, often referred to as non-aqueous phase liquids (NAPLs)[30,42]. Furthermore, the inability of these particles to localize at NAPL-water interfaces requires injection of large amounts of material, which hastens aggregation and exacerbates this problem[43].

In an effort to mitigate rapid aggregation and sedimentation of nZVI, several studies have investigated the impact of polyelectrolyte and polymer coatings[42,44–46], and other surface modifications[47–49] on their stability, agglomeration, and deposition rates. Dispersions of anionic polyelectrolyte-coated commercial nZVI, or reactive nanoscale iron particles (RNIP), exhibit increased stability due to electrosteric repulsions between polyelectrolytes, while unmodified RNIP rapidly form micrometer-sized aggregates and later gel to form chains[44].

In addition to nZVI, other nanoparticles, such as bimetallic nanoparticles (BNPs) and metal oxides, have been explored for their uses in groundwater remediation. These materials also have the capacity to detoxify immiscible contaminants or adsorb heavy metals. BNPs are usually comprised of a reactive, corrosive metal and a noble metal that catalyzes and increases the rate of reaction. Iron and nickel (FeNi) BNPs have been shown to increase the rate of TCE degradation by almost two orders of magnitude compared to nZVI alone, but their short lifetimes make them impractical for long term use[50,51].

Alternatively, noble metals may provide a good model system. Like nZVI, some of these noble metals, including silver (Ag) and platinum (Pt), exhibit interesting chemistry. Ag nanoparticles can reduce dyes with various charges[52], while Pt nanoparticles have been shown

to reduce 4-nitrophenol, a toxic contaminant found in some soils, to 4-aminophenol[53]. Furthermore, they resist oxidation and form stable dispersions in the presence of stabilizers such as citric acid[54] or guar gum[55]. These characteristics make noble metal nanoparticles useful systems to study before considering the added complexity of aggregation.

1.3 Fabrication of complex colloids

Most research on the use of reactive nanoparticles has focused on their stabilization through the use of surfactants or polymer coatings[46,56–59]. However, another area of research focused on fabrication of hybrid materials may present an alternative solution to improve stability and efficacy of conventional nanomaterials. Hybrid materials, or materials containing both organic and inorganic components, are of significant interest in a broad range of applications ranging from drug delivery and bioimaging[60–64] to heterogeneous catalysis[65–68]. Several methods have been explored to produce nanostructured and phase separated polymeric colloids: in particular, methods such as self-assembly,[69–71] self-organized precipitation (SORP),[72–75] and Flash NanoPrecipitation (FNP)[76–78]. Furthermore, the capabilities of some of these methods have been expanded to produce hybrid nanoparticles (hNPs) that contain both an organic polymeric component and an inorganic metal component. While widespread use of some of these methods may be hindered by more complex, multi-step fabrication techniques[79–82], self-assembly[83,84], encapsulation in nano-shells or nanopores[85], and self-organized precipitation (SORP)[86–88] hold promise due to their ability to precisely place inorganic components on or within an organic component.

In particular, SORP presents a promising method for hNP production because it harnesses equilibrium phase separation to control metal nanoparticle placement within polymeric nanoparticles. In several studies, gold nanoparticles were stabilized using polymers so they could be readily incorporated into block copolymer solutions in the presence of a poor solvent, resulting in localization of gold nanoparticles in the same domain as its polymer stabilizer[86–88]. In some examples, gold nanoparticles were internalized in lamellae or localized atop polymer nanoparticles[74]. However, despite the success of this method in producing hybrid nanostructured particles, previously reported experimental methods require modification of the metal component to be compatible with the appropriate polymeric domain and require several days to produce the final particle suspensions, presenting opportunities for improvement in total production time, and simplified, scalable fabrication.

Flash NanoPrecipitation (FNP) presents an alternative pathway to simple, scalable fabrication of hNPs that addresses production time limitations presented by SORP. FNP is a continuous, scalable, one-step colloidal fabrication process that results in solvent exchange between a good solvent and a poor solvent, or anti-solvent. The solvent exchange process occurs on a time scale, τ, much faster than the aggregation time of the solute, so $\tau_{mixing} < \tau_{aggregation}$. The ratio of these two times is represented by the Damköhler number (Da); here, Da $\ll 1$. Using a confined impinging jet (CIJ) mixer, one syringe containing the solute in a good solvent and another containing the anti-solvent are expressed manually. The resulting jets hit each other at a velocity of approximately 1 m/s through 0.5 mm orifices, resulting in a turbulent Reynolds number of mixing of $\sim$3500[89] and fabrication times on the order of seconds.

The turbulent mixing engendered by the CIJ mixer allows for production of monodisperse colloidal particles, while tunability of polymer composition and concentration in the FNP

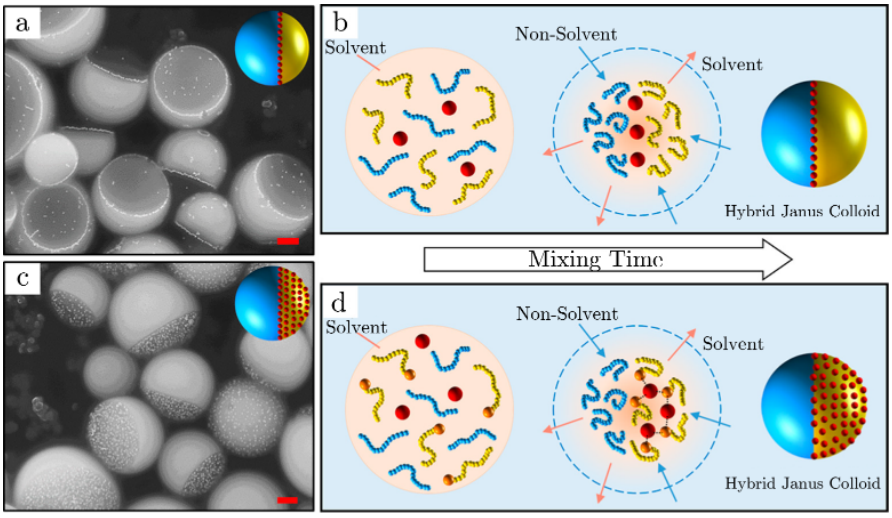


Figure 1.3: Hybrid structured colloids produced *via* Flash NanoPrecipitation (FNP). (a) Scanning electron microscopy (SEM) image of Janus particles comprised of polystyrene (PS) and polyisoprene (PI) display Au nanocatalysts aligned at the PS/PI interface. (b) Schematic shows that the neutral surfaces of Au nanocatalysts do not favor interactions with either homopolymer, resulting in the morphology shown in (a). (c) SEM image of Janus particles comprised of amine-terminated polystyrene (PS-NH_2) and PI show Au nanocatalysts dispersed exclusively on the PS-NH_2 domain. (d) Schematic shows that attractive electrostatic interactions between the amine groups of the PS-NH_2 polymer chains and citrate groups on the Au nanocatalyst result in the morphology observed in (c). In (a) and (b), osmium tetroxide-stained PI comprises the lighter domains, PS or PS-NH_2 comprise the darker domains, and small bright dots are Au nanocatalysts. The scale bar in all images is 200 nm. Reprinted (adapted) with permission from [76]. Copyright 2017 American Chemical Society.

inlet streams allow for facile production of a wide variety of colloidal morphologies, including hybrid [53] and structured colloids [76–78,90]. In one such study, a homopolymer blend was impinged against an aqueous suspension of metal nanocatalysts to produce Janus particles with surface decoration either on one hemisphere of the Janus particle or at its equator [76], as shown in Fig. 1.3. Another study produced hybrid nanoparticles by impinging a block copolymer solution against a metal salt; the resulting mixture was deposited into a reducing agent to precipitate metal nanocatalysts on polymeric nanoparticle surfaces [53]. The tunability of this platform thus presents a unique opportunity to develop fabrication methods to stabilize reactive nanoparticles, but limited work exists to address a method that also controls the

rate at which hNPs degrade contaminants, which is of critical importance in environmental remediation.

1.4 Colloidal transport in 3D porous media

Traditional studies of colloids in porous media are in saturated, or aqueous, two-dimensional micromodels or three-dimensional core samples. In two-dimensional studies, single pillars, or collectors, have been used to characterize the kinetics of deposition at varying values of the Péclet number[91,92], but in the absence of multi-collector networks and pore connectivity, they fail to capture key hydrodynamic parameters that govern behavior in real systems[93]. These hydrodynamic parameters, along with physical properties of the particles and properties of the porous medium, influence deposition and clogging events. To remedy the simplifications made in two-dimensional studies[94–98], three-dimensional experiments have been conducted using lab scale columns[99–102], revealing interesting phenomena that could not be observed in 2D. For example, one study showed that injection of higher particle concentrations results in pore space clogging that leads to subsequent flow redirection and particle motion transverse to the direction of flow[103], while another showed that salt concentration gradients not only control colloidal particle deposition naturally, but can be harnessed to select the location of deposition[104].

Section 1.4 of Chapter 1 is based in part on a published textbook chapter by Navid Bizmark, Joanna Schneider, Emily de Jong, and Sujit S. Datta. Chapter: Transport of Polymer Colloids in Porous Media. *Polymer Colloids: Formation, Characterization and Applications*, Royal Society of Chemistry, 2019.[1]

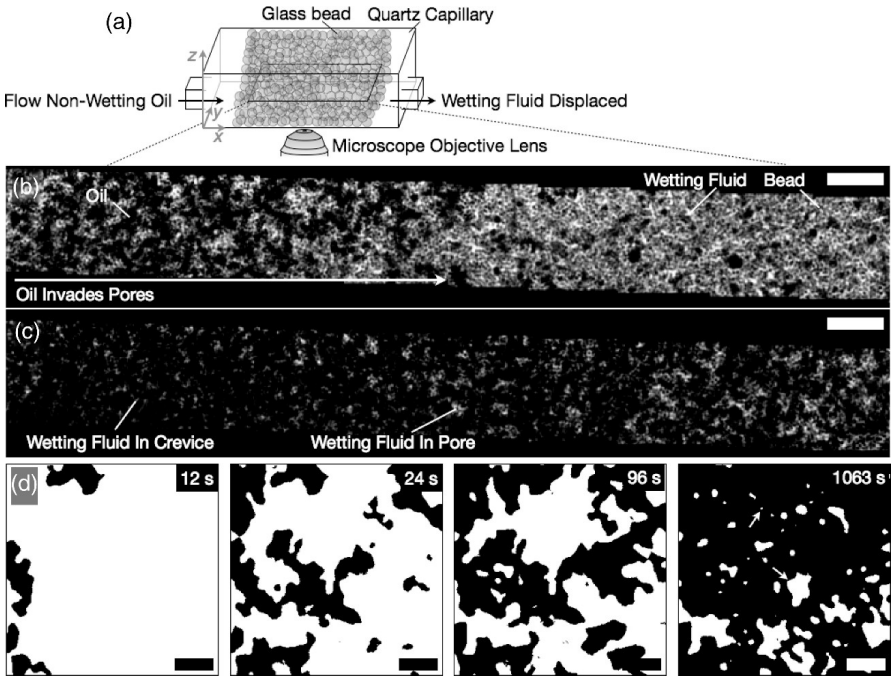


Figure 1.4: Use of refractive-index matching to image immiscible flows in three-dimensional (3D) model porous media. (a) Schematic of a non-wetting fluid displacing a wetting fluid in a model 3D porous medium. Flow within the medium is visualized using confocal microscopy. The pore space is initially saturated with a fluorescently dyed wetting fluid, which is displaced by an undyed non-wetting fluid. (b) Confocal micrograph showing a non-wetting fluid displacing a wetting fluid at a flowrate, $Q = 1$ mL/h. Bright regions indicate wetting fluid and black circles show cross sections of the beads comprising the porous medium. Additional black areas show the invading oil. The path taken by the oil varies spatially, as seen in the region spanned by the arrow. Scale bar is 500 μm. (c) Confocal micrograph of the same region shown in (b) after invasion of ≈ 9 pore volumes (PVs) of oil. Some wetting fluid remains trapped in the crevices and pores of the medium, as indicated. Scale bar is 200 μm. (d) Time sequence of zoomed confocal micrographs with the pore space subtracted; binary images show oil in black as it bursts into the pores. Upper and lower arrows in the last frame show wetting fluid trapped in a crevice or in a pore, respectively. Imposed flow direction in all images is from left to right. Reprinted from [105], with the permission of AIP Publishing.

While 3D setups provide a more accurate picture of real porous media, these setups come with their own problems. Because these media are usually opaque, pore-scale events cannot be monitored and are typically hypothesized based on differences between the influent and effluent particle concentrations[99,100]. To overcome this issue, magnetic resonance imaging and X-ray microtomography have been used to yield additional insights into the spatial distribution of particles in the pore space—for example, indicating that the distribution of deposited particles is sensitive to the particle charge[106], size[107], and imposed flow conditions[108]. However, such approaches typically do not capture pore-scale dynamics of colloidal transport and deposition due to limitations in spatial or temporal resolution. To address these limitations, refractive index matching has been used successfully to render 3D porous media transparent in three-dimensional fluidic devices[109]. This technique has been used to relate pore-scale events to macroscale observations in studies of both colloidal transport[110] and immiscible fluid flow[105], as shown in Fig. 1.4; however, this technique has not yet been used to study colloidal behavior in immiscible fluid flow.

In Chapter 2, I utilize this refractive index-matching technique to simultaneously visualize colloidal deposition and immiscible fluid droplets within the pore space for the first time. As the particles deposit on the solid matrix, increasing amounts of trapped fluid become mobilized, ultimately enabling removal of $\sim 70\%$ of the fluid. By analyzing the extent of deposition, as well as the geometry of trapped fluid droplets at the pore scale, I determine that deposition reduces the permeability of the medium—thereby enabling the viscous stresses on the trapped droplets to overcome the influence of capillarity keeping them trapped without excessively restricting the fluid flow.

In Chapter 3, I further explore how the competition between viscous stresses and cap-

illarity may be used to estimate mobilization of immiscible fluids from a stratified porous medium. Specifically, I examine how the existence of stratified layers within a porous medium alters theoretical mobilization predictions. I find that mean-field approaches that average the properties of a stratified medium frequently overpredict the total amount of non-wetting fluid removed from the medium when compared to predictions that consider strata independently. By generalizing my findings over a range of structural parameters, I provide quantitative guidelines to produce better predictions of non-wetting fluid mobilization in stratified porous media.

Building upon the knowledge of immiscible and colloidal flows developed in Chapters 2 and 3, I study how colloidal deposition and immiscible flows alter each other's behavior in Chapters 4 and 5. In these chapters, I use both experimental and computational tools to observe how capillary stresses at immiscible fluid interfaces force static colloidal deposits to be eroded. I show that the ability of these fluid interfaces to erode and redeposit colloidal particles in systems with dense multilayer deposition has the capacity to change macroscale immiscible flow patterns and visualize this process using pore-scale experiments.

Having extensively explored the interactions between colloids and immiscible fluids in porous media, in Chapter 6, I demonstrate a method of producing stable hybrid nanoparticles with tunable morphologies using a two-step technique that harnesses Flash NanoPrecipitation. I find that gold adsorption to polystyrene nanoparticles is enabled by the presence of a good solvent for polystyrene, establishing a criterion for their formation. Systematic exploration of a variety of molecular and process parameters shows that this technique can control both the resulting hybrid nanoparticle morphologies as well as the rate at which they degrade contaminants, which has important implications for environmental remediation.

Finally, in Chapter 7, I discuss future directions for this work. Specifically, I discuss how the hybrid nanoparticles developed in Chapter 6 could be implemented in a three-dimensional porous medium, such as those described in Chapter 2. I hypothesize that dilute deposition of hybrid nanoparticles could be harnessed for reduction of aqueous contaminants, which could be treated as they flow over deposited particles, while the same process could be utilized for immiscible contaminants to force adsorption of these reactive particles to their interfaces, as we see in Chapter 4. This chapter provides a framework for potential next steps that could be taken by a student interested in building upon the knowledge built in this dissertation.

If you're not changing, you're not growing;

you're not being present.

Change is essential.

Maggie Rogers

2

Harnessing colloidal deposition for trapped fluid mobilization

Colloids have gained increasing popularity over the last 30 years for groundwater remediation efforts due to their ability to be implemented *in situ*, or directly into subsurface

aquifers to treat flowing or trapped contaminants. Non-aqueous contaminants are of particular interest to the general public because of the risks they pose to human health [111,112], as well as to physics and engineering communities due to the challenge of capillary stresses that keep these contaminants trapped [8]. In an effort to overcome this challenge, researchers have begun to explore the benefits of injecting colloidal suspensions into porous aquifers to improve removal of immiscible contaminants [19,113,114]. However, to improve the efficacy of this approach, it is critically important to be able to predict *whether* and *how* nano- and micro-scale particles can help mobilize trapped immiscible fluids from a heterogeneous pore space.

There are several mechanisms by which colloidal particles have been hypothesized to help mobilize trapped fluids from the pore space. One such mechanism is through colloidal surface activity, which causes particles to preferentially localize at immiscible fluid-fluid interfaces owing to their surface chemistry. Colloidal adsorption at immiscible fluid-fluid interfaces reduces their interfacial tension and weakens the capillary stresses that keep fluid trapped [19–25]. However, non-surface active colloids have also been postulated to enhance immiscible fluid mobilization—for example, through their ability to reduce fluid slip [115] or enhance disjoining pressure *via* the formation of thin films [28,29].

Importantly, all of these mechanisms rely on the ability of colloidal particles to freely move through the pore space without depositing on the solid matrix: deposition hinders the ability of particles to localize at target fluid interfaces, [15,30] and potentially causes clogging that impedes subsequent flow [31–34]. As a result, researchers typically seek to minimize deposition of colloidal particles in porous media—for example, by tuning colloidal interactions or only using low concentrations of particles [35,36]. However, different flow conditions and colloidal chemistries strongly influence colloidal transport and deposition; while some studies suggest

that colloids suppress transport by reducing the permeability of the medium [31,33,56,116], others report that colloids can enhance the transport of chemicals through a porous medium [117–119].

In this chapter, we address both the challenges of studying colloidal transport and deposition systematically in complex, three-dimensional porous media as well as the complexities introduced by the presence of a non-aqueous fluid to address the question: can colloidal deposition be harnessed to enhance immiscible fluid mobilization from porous media?

To accomplish this goal, we first unravel the physics that underlie how colloidal particles are transported and deposit within a saturated 3D porous medium. Using confocal microscopy, we directly visualize colloidal transport and deposition. Our results show that the macroscopic distribution of colloidal particles within a porous medium can be controlled solely by imposed pressure. At high injection pressures, particles deposit in and erode from the pore space continually, enabling them to deposit throughout the entire medium. Conversely, at low pressures, the relative influence of erosion is suppressed, causing particles to be localized near the inlet of the medium.

Next, we demonstrate that deposition can, surprisingly, *promote* mobilization of a trapped fluid from a porous medium without requiring any surface activity. In this dissertation, we define surface activity to mean that colloidal particles spontaneously attach and stick to immiscible fluid interfaces under quiescent conditions. Using confocal microscopy, we directly visualize both colloidal particles and trapped immiscible fluid within a transparent, three-dimensional porous medium. We find that as non-surface active particles deposit on the solid matrix, increasing amounts of trapped fluid become mobilized. By analyzing the extent of deposition and the geometry of trapped fluid droplets at the pore scale, we find that deposition increases the viscous stresses on trapped droplets, overcoming the influence of capillarity that

keeps them trapped. Given an initial distribution of trapped fluid, this analysis enables us to predict the extent of fluid mobilized through colloidal deposition, revealing a new way by which colloids can be harnessed to mobilize trapped fluid from a porous medium.

2.1 Connecting pore scale deposition & macroscopic colloidal transport

To begin developing an understanding of colloidal transport and deposition in 3D porous media, we first investigate the injection of a dilute suspension (0.05 vol%) of positively charged, amine-functionalized polystyrene (PS-NH_2) particles into a saturated porous medium under a large imposed pressure drop, $\Delta P = 260$ kPa. Here, we hypothesize that particle deposition will be localized near the inlet of the medium due to strong electrostatic attraction between the positively charged particles and negatively charged borosilicate glass beads that comprise the medium [119,120]. However, we instead observe the formation of an extended deposition profile of particles that spans the entire length of the porous medium, (Fig. 2.1a, Movie S1). This profile persists over the course of injection: the amount of deposition at each position along the flow direction–quantified by the fraction of the initial pore space area $A_{pore,0}$ occupied by deposited particles having total area A_d–steadily grows in time, (Fig. 2.1b).

Inspection of particle deposition at the pore scale provides insight into the mechanism un-

Sections 2.1–2.2 of this chapter have been adapted from published work by Navid Bizmark, Joanna Schneider, Rodney D. Priestley, and Sujit S. Datta. Multiscale dynamics of colloidal deposition and erosion in porous media. *Science Advances*, 6, 2020.[2] **Author Contributions:** N.B. and S.S.D. designed the experiments; N.B. performed experiments; N.B., J.S., and S.S.D. analyzed the data; N.B. and S.S.D. developed the theoretical model; S.S.D. designed and supervised the overall project. All authors discussed the results and wrote the manuscript.

derlying extended deposition. Because Pe $\gg 1$ and particle-bead interactions are attractive, we expect fluid flow to advect particles toward the upstream faces of the beads, forcing them to initially attach. Consistent with this expectation, some particles initially deposit on the upstream surfaces of the pristine beads (Fig. 2.2a, top panel). As particle injection continues, these deposits continue to grow (Movie S2) suggesting that the hydrodynamic stresses due to fluid flow are sufficient to overcome electrostatic repulsion between like-charged particles. This observation is consistent with previous findings in 2D media[94–98,121], although nanoscale heterogeneity in colloidal interactions may also play a role[122].

While some deposits grow monotonically, these dynamics are not universal. In many cases, single and multi-particle deposits are eroded and abruptly removed by fluid flow, as predicted by recent simulations[123]. An example is shown in the bottom panel of Fig. 2.2a and in Movie S3. Here, eroded particles are re-deposited in other pores downstream. This process of deposition, erosion, and re-deposition progresses continuously over the course of injection, enabling particles to be deposited throughout the entire medium. Moreover, while substantial, erosion does not completely balance deposition: the instantaneous rate of pore-scale deposition is slightly larger than the rate of erosion (Fig. 2.2b). This difference results in net deposition throughout the entire medium that progressively increases over time (Fig. 2.2c, top panel). Therefore, we hypothesize that pore-scale erosion generates the extended macroscopic deposition profile shown in Fig. 2.1a.

To quantify this hypothesis, we analyze the stresses on colloidal particles at the pore scale. Because the imposed pressure drop is large, we expect that hydrodynamic stresses are large enough to drive erosion. To quantify this hypothesis, we use Darcy's law to estimate the characteristic viscous pressure drop across an isolated deposit of diameter D, $\Delta P_D = \mu Q D/(Ak)$,

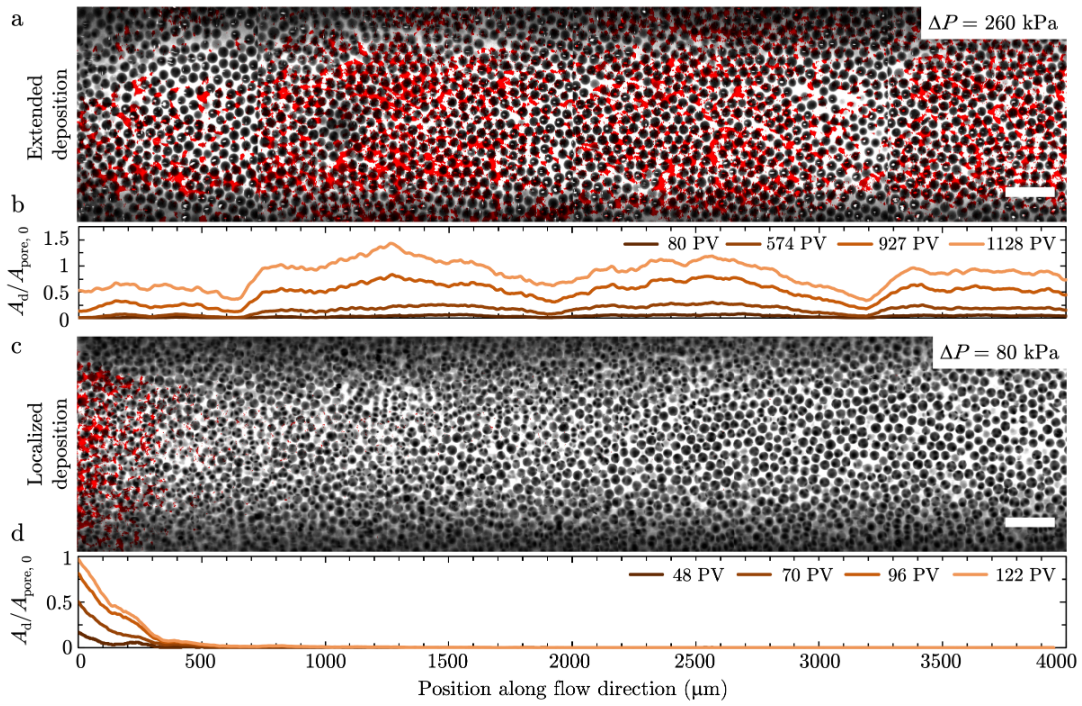


Figure 2.1: Macroscopic deposition profile of positively charged colloidal particles is tuned by injection pressure. Confocal micrographs show extended (a) and localized (c) deposition profiles after t=3.1 and 1.9 h for amine-functionalized polystyrene particles injected at 260 or 80 kPa, respectively. Black circles show cross sections through the beads making up the porous medium, white space shows pore space, and red shows deposited colloidal particles. Corresponding line traces in (b) and (d) show the amount of deposition at each position along the flow direction, quantified by $A_d/A_{pore,0}$, where A_d is the laterally averaged area occupied by deposited particles and $A_{pore,0}$ is the pore space area before colloidal particle injection. Traces show A_d with a running average over every 100 μm along the length of the medium to minimize noise; different traces are shown for images obtained every 2 min in (b) and 3 min in (d), which we represent by the total number of suspension PVs injected. The traces exhibit some spatial fluctuations that likely reflect the influence of packing heterogeneities in the disordered media. In some cases, $A_d/A_{pore,0}$ slightly exceeds one due to the non-zero thickness of the optical slice. The flow direction is from left to right, and scale bars represent 200 μm.

at $t = 0$; here, μ is the fluid dynamic shear viscosity and k is the permeability of the porous medium, measured previously for a pristine medium [124]. For deposits of size D ranging from one to four particle diameters (Movie S3), ΔP_D ranges from $\sim$ 10–60 Pa. We conjecture that this characteristic pressure drop is larger than the yield stress required to fluidize dense colloidal aggregates with slight interparticle attraction, σ_y, which we estimate to be between $\sim$ 1–10 Pa based on previous shear rheology measurements [125]. Thus, we expect that fluid flow drives erosion, as observed in experiments. This balance of pressures neglects spatiotemporal variations in flow as well as the full details of colloid-colloid and colloid-bead interactions; it therefore provides an order-of-magnitude estimate of the onset of erosion.

As particles continue to deposit, the permeability of the medium and the volumetric flow rate decrease (Fig. 2.2c, middle panel). The interstitial flow speed $v(t) \equiv Q(t)/[\varphi(t)A]$, calculated by directly estimating the time-dependent porosity $\varphi(t) = \varphi_0[1 - A_d(t)/A_{pore,0}]$ from our micrographs, concomitantly decreases as shown in the bottom panel of Fig. 2.2c; this quantity provides a measure of the magnitude of the characteristic interstitial flow velocity. However, even at these lower flow rates and flow speeds, $\Delta P_D \gtrsim \sigma_y$, enabling erosion to continue to progress. Thus, particles continue to deposit, erode, and re-deposit in the entire porous medium over the course of the experiment, driving extended deposition throughout.

Our analysis also suggests that the relative contribution of erosion can be tuned by the imposed pressure drop. To test this prediction, we repeat the previously described experiment at a lower $\Delta P = 80$ kPa. Under these conditions, we expect hydrodynamic stresses—and thus the relative magnitude of erosion—to be less dominant, likely resulting in different deposition behavior. Consistent with this expectation, we observe starkly different deposition behavior: instead of particles depositing throughout the entire porous medium, as in the high

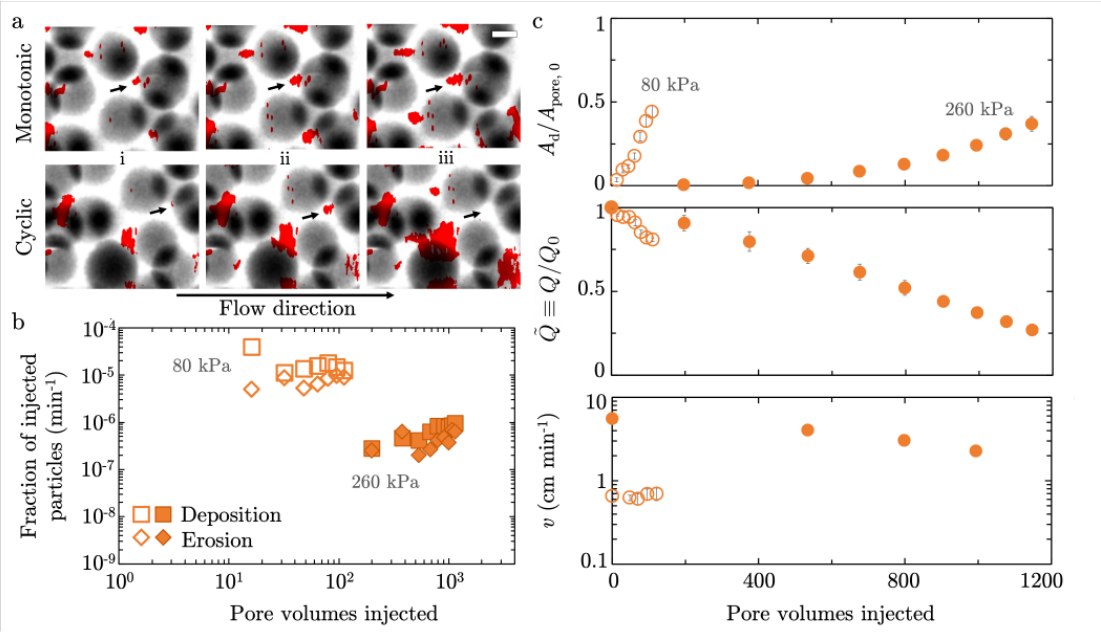


Figure 2.2: Deposition and erosion of positively charged colloidal particles at the pore scale. (a) Arrows in the upper and lower sequences of micrographs show monotonic deposition and cyclic deposition–erosion of particles upstream of a bead, respectively, at 260 kPa. (i) to (iii) show micrographs after the injection of 675, 903, and 1074 total PVs of the colloidal suspension. Black circles show cross sections through the beads making up the porous medium, white space shows pore space, and red shows deposited colloidal particles. Scale bar is 20 µm. (b) Rates of particle deposition (squares) and erosion (diamonds), calculated by subtracting successive images, are shown as a function of total PVs injected for 260 and 80 kPa, indicated by the filled and open symbols, respectively. (c) Top, middle, and bottom panels show the fraction of the pore space area occupied by deposited particles $A_d/A_{pore,0}$, the volumetric flow rate Q normalized by its initial value (1.5 mL/h for 260 kPa and 0.15 mL/h for 80 kPa), and the interstitial flow speed, respectively, as they vary with the total PVs injected. Experiments at 260 and 80 kPa are indicated by filled and open symbols, respectively. Error bars in (c) reflect uncertainty arising from binarizing the micrographs or from variation in flow rate measurements. Error bars not observable in (c) are smaller than the symbol size.

pressure case, particles only deposit locally near the inlet (Fig. 2.1c, Movie S4). We quantify this observation in Fig. 2.1d, which shows that the fraction of the pore space that is occupied by particles no longer spans the entire length of the medium but instead appears to decay exponentially, approaching zero at a distance L_d approximately 7% of its length.

As expected, these differences in macroscopic deposition reflect strong differences in pore-scale deposition and erosion, in addition to previously documented differences in particle transport at different pressures[108]. For $\Delta P = 80$ kPa, the instantaneous rates of particle deposition and erosion—as well as the difference between them—are one order of magnitude larger than at $\Delta P = 260$ kPa (Fig. 2.2b). This difference results in a larger fraction of particles depositing in the medium over a shorter amount of time (Fig. 2.2c, top panel). As a result, the volumetric flow rate decreases, indicating that localized deposition at the inlet "chokes off" the flow (Fig. 2.2c, middle panel). The corresponding interstitial flow speed is nearly an order of magnitude lower than that of the high pressure case (Fig. 2.2c, bottom panel). Consequently, the viscous pressure drop across a deposit, $\Delta P_D \sim 1$–6 Pa, is insufficient to overcome the deposit yield stress, estimated as $\sigma_y \sim 1$–10 Pa, and erosion is suppressed.

2.2 Implications of dynamic deposition & erosion

These results directly connect the dynamic processes of colloidal deposition and erosion at the pore scale to their resulting deposition profiles at the macroscopic scale. Surprisingly, we find that particles deposit throughout the entire medium at large pressures *via* continual erosive bursts despite large Pe and attractive interactions between particles and the beads that

comprise the porous medium. Erosion has previously been theorized to occur using pore-scale simulations[123], and indirect signatures of erosion have been detected using bulk transport measurements[126]; our results provide a connection between these pore-scale events and macroscopic deposition behavior. Furthermore, they highlight the importance of hydrodynamic interactions in determining colloidal transport and deposition. Specifically, these results suggest that erosion plays a dominant role in distributing particles throughout the pore space when the viscous pressure drop, ΔP_D, across deposited particles exceeds a threshold value, which we conjecture is given by the deposit yield stress, σ_y.

Diverse applications require control over colloidal deposition in porous media. In some cases, localized deposition is essential. For example, in groundwater remediation, deposition of catalytically active particles for *in situ* treatment of heavy metal contaminants has been explored[104]. Here, colloidal deposition is required, but only at specific locations of the medium. Other examples include filtration and containment of pathogens or waste materials, which require effective capture near the inlet of the medium[127]. In the following sections of this chapter, we harness this newfound control over the colloidal deposition process to explore how *extended* deposition profiles may be used. Critically, many of these applications require an understanding of how colloidal transport and deposition processes may be altered by the presence of an immiscible fluid. Key examples are enhanced oil recovery[29], in which injected particles must be able to reach residual oil in a reservoir and nanoparticle-assisted groundwater remediation[42,128,129], in which injected particles must be able to reach trapped contaminants in an aquifer log distances from an injection site. To accomplish this goal, we develop experiments in which we first create an initial configuration of trapped fluid before assessing how deposition may alter immiscible fluid mobilization from a 3D porous medium.

2.3 Establishing an initial trapped fluid configuration

We prepare a model 3D porous medium by lightly sintering a dense packing of borosilicate glass beads at 1,000 °C for 3.5 min in a quartz capillary tube with a square cross-sectional area $A = 9$ mm^2. The beads have radii $a = 62$–75 μm and the packing spans a length $\ell = 2.6$ cm. Light scattering from the solid matrix formed by the beads typically renders the medium opaque, precluding imaging of flow and transport in the pore space. To overcome this limitation, we formulate a wetting fluid of 50 wt% dimethyl sulfoxide (DMSO), 30 wt% glycerol, and 20 wt% deionized water, dyed with Rhodamine Red, that has the same refractive index as the solid matrix; thus, infiltrating the pore space with this fluid renders the medium completely transparent. Further, this fluid enables the colloidal particles used in our experiment to remain stable in suspension over an experimental time scale of > 18 hours, as verified by confocal microscopy at single-particle resolution. To investigate immiscible fluid trapping and mobilization, we formulate another fluid, an oily mixture of aliphatic and aromatic hydrocarbons (*Cargille* refractive index liquids), that has the same refractive index as the wetting fluid and the solid matrix, but is non-wetting. Measurements performed on a similar fluid pair indicate that the three-phase contact angle between the wetting fluid and glass in the presence of the non-wetting oil is $\theta \approx 5°$ [124]. The interfacial tension between the two liquids is $\gamma \approx 13$ mN/m as measured previously [105] and the dynamic shear viscosities of the wetting and non-wetting fluids are $\mu_w = 10.8$ mPa·s and $\mu_{nw} = 16.8$ mPa·s, respectively, measured using a cone-plate rheometer. Before saturating the pore space with fluid, we pull vacuum and push CO_2 through the medium. We then saturate the pore space with deionized

water to dissolve any remaining CO_2. Finally, we pull vacuum once more before saturating the pore space with the dyed particle-free wetting fluid—preventing trapping of any residual air bubbles in the medium.

We then use a *Nikon* A1R+ confocal fluorescence microscope to characterize the pore space structure, as schematized in Fig. 2.3a. Specifically, we obtain images, each spanning 1,024 μm × 1,024 μm in the *xy* plane at a single depth within the porous medium centered at $z = 135$ μm, with an optical thickness of 14 μm. A magnified view from one image is shown in Fig. 2.3b. The brightness in the image reflects the fluorescent signal from the dyed wetting fluid in the pore space, with primary excitation and emission at 560 and 580 nm respectively, enabling identification of the glass beads by their contrast with the dyed wetting fluid and shown by the dark circles in the bottom of the image. Together, the tiled images span the entire cross-section of the medium and therefore reproduce a two-dimensional (2D) slice of the pore space. Using adaptive binarization of the images and restricting all analysis to approximately 5 bead diameters away from the inlet and outlet to minimize the influence of boundaries, we measure the initial porosity of the pristine medium, $\varphi_0 = 0.38 \pm 0.06$, in good agreement with previous measurements[124].

We introduce the non-wetting oil into the pore space using a *Harvard Apparatus* Pump 11 Elite syringe pump, injecting approximately 30 pore volumes (PVs) at a fixed volumetric flow rate $Q_{nw} = 15$ mL/h; here, the number of PVs injected after a duration of time t is given

---

Sections 2.3–2.9 of this chapter have been adapted from published work by Joanna Schneider, Rodney D. Priestley, and Sujit S. Datta. Using colloidal deposition to mobilize immiscible fluids from porous media. *Physical Review Fluids*, 6, 2021.[3] **Author Contributions:** J.S. and S.S.D. designed the experiments; J.S. performed all experiments; J.S. and S.S.D. analyzed the data and developed/implemented the theoretical model; S.S.D. designed and supervised the overall project. All authors discussed the results and wrote the manuscript.

by $Q_{nw}t/\left(\varphi_0 A\ell\right)$. We simultaneously acquire tiled images spanning the entire cross-section of the medium successively. Because the oil is undyed, it appears dark in the confocal micrographs, as indicated in the top of Fig. 2.3b. Thus, comparing the micrographs to those obtained during initial characterization of the pore structure provides a 2D map of the oil configurations at sub-pore resolution. Due to the high flow rate Q_{nw}, oil saturates the majority of the pore space. The measured residual oil saturation, S_{OR}, defined as the fraction of the pore space area occupied by oil, is 0.75. We normalize all subsequent measurements of S_{OR} by this maximal value, as indicated by the first data point in Fig. 2.3c.

We then re-inject approximately 55 PVs of the particle-free wetting fluid at a rate of $Q_w =$ 0.15 mL/h, emulating flow conditions in many subsurface formations[130]; in this case, PV $\equiv$ $\int_0^t Q/\left(A\ell\varphi(t)\right)\,\mathrm{d}t$ and the time-dependent porosity $\varphi(t)$ measured directly from the confocal micrographs accounts for the fraction of the pore space accessible to the wetting fluid, which changes as oil is mobilized from the porous medium. Under these conditions, the wetting fluid flow leads to the formation of discrete droplets, or ganglia, of the non-wetting oil. While some of these ganglia become mobilized by the wetting fluid, approximately 72% of the original oil in place remains trapped by capillarity[105,131], as indicated by the decrease in S_{OR}, shown by the black circles in Fig. 2.3c, within the first approximately 6 PVs of fluid injection. The wetting fluid then continues to flow around them. This protocol thus establishes an initial steady-state configuration of trapped ganglia, as indicated by the circles for 6–50 PVs in Fig. 2.3c and exemplified by the micrograph in Fig. 2.3d. As is frequently the case in confined and stratified media[132,133], most of the trapped ganglia are located near the boundaries of the medium, with smaller ganglia closer to the center of the pore space.

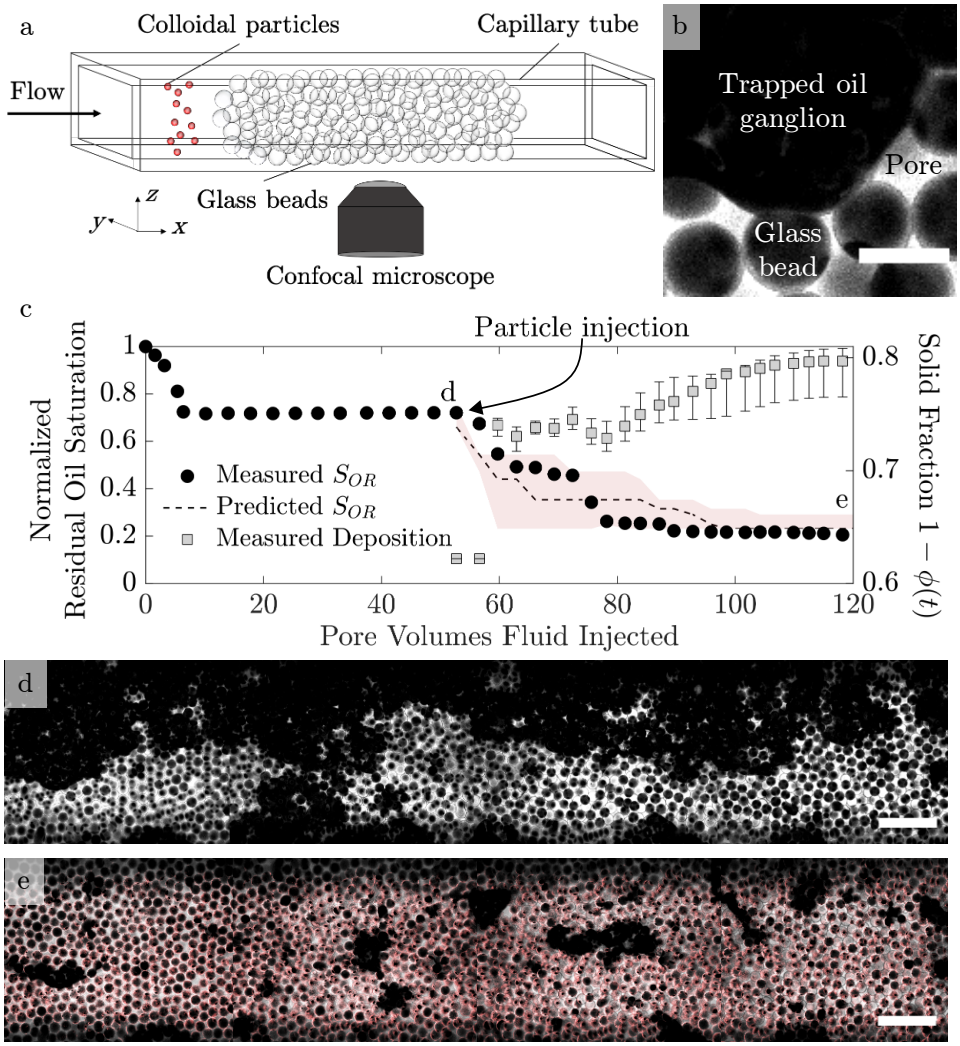


Figure 2.3: Colloidal deposition promotes oil mobilization. (a) Schematic of the porous medium composed of glass beads packed in a capillary tube. Fluid flow is imposed along $+x$ and micrographs are taken at a fixed depth z within the medium. (b) Magnified micrograph showing trapped oil before particles are injected. Fluorescent signal from the dyed wetting fluid appears as white; hence, white indicates pore space, black circles show the beads, and additional black shows a trapped oil ganglion. Scale bar represents 150 μm. (c) Black points show the variation of the residual oil saturation S_{OR}, normalized by its maximal value 0.75, over the course of the experiment. Injecting particle-free wetting fluid results in an initial slight decrease in S_{OR}. We then inject the particle suspension at the time indicted by the arrow, which results in a further decrease in S_{OR}. Grey points show the increase in the solid fraction $1-\varphi(t)$ over time due to deposition measured from the micrographs. Error bars show differences in the calculated solid area fraction for $\pm 20\%$ of the image binarization threshold. Dashed line shows our theoretical prediction of S_{OR}, and the red region shows uncertainty in the prediction arising from heterogeneities in deposition as described in Fig. 4. Panels (d) and (e) show images of the porous medium before and after colloidal injection, respectively, as indicated in (c), showing that particle deposition—indicated by red—mobilizes trapped oil. Scale bars represent 750 μm. Imposed flow direction is from left to right.

2.4 Enhanced mobilization of trapped oil by colloidal particles

To explore whether and how colloidal particles can help mobilize the trapped oil, we next inject a suspension of positively charged, amine-terminated polystyrene particles (*Sigma Aldrich*) of diameter $d_p = 1\,\mu$m into the medium. The particles are fluorescently labeled, with primary excitation and emission at 470 and 505 nm respectively; these values are distinct from those of the wetting fluid, enabling multiplexed imaging of both particles and wetting fluid simultaneously. The spatial resolution of the imaging is 3 μm, and thus, each pixel comprises up to 3 particles. We first homogenize a concentrated 2.5 vol% aqueous suspension of the particles by vortexing for 10–15 min, and then redisperse the particles in the wetting fluid at a concentration of 8×10^{-3} vol%. We then inject this suspension into the porous medium directly following the particle-free wetting fluid injection, at the same flow rate $Q_w = 0.15$ mL/h. The initiation of particle injection is indicated by the arrow in Fig. 2.3c. As injection progresses, the particles gradually deposit onto the negatively-charged glass matrix throughout the medium due to electrostatic attraction[2], indicated by the red in Fig. 2.3e. The measured solid area fraction averaged over the entire medium, $1 - \varphi(t)$, increases due to deposition and eventually plateaus after $\approx$ 40 PVs of the suspension are injected, as shown by the grey squares in Fig. 2.3c, likely due to electrostatic repulsion between like-charged particles[2].

By constricting the pore space, this process of deposition is usually thought to detrimentally hinder fluid flow. Unexpectedly, however, we find that trapped ganglia are mobilized from the medium: the residual oil saturation decreases as deposition progresses, ultimately reaching only $\approx 30\%$ of its initial steady-state value after $\approx$ 30 PVs of suspension are injected,

as shown by the black circles for ≈ 50–80 PVs in Fig. 2.3c and exemplified by the micrograph in Fig. 2.3e. Clearly, particle deposition *promotes*, not hinders, trapped oil mobilization.

2.5 Characteristics & features of colloidal deposition

Why does particle deposition promote oil mobilization? Two possible mechanisms are (i) colloidal surface activity, which reduces the fluid-fluid interfacial tension and thereby reduces the strength of capillarity keeping ganglia trapped, and (ii) selective clogging of some pores redirecting the fluid flow toward trapped ganglia. We use our pore-scale visualization to examine the influence of these mechanisms in our experiment.

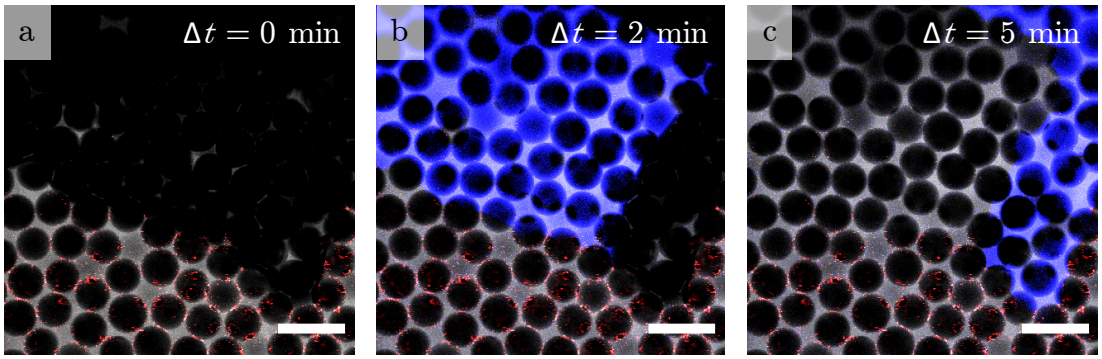


Figure 2.4: Oil mobilization does not occur due to colloidal surface activity. Magnified views of confocal micrographs show an oil ganglion (a) before, (b) during, and (c) after mobilization. White regions show pore space, black circles show the bead matrix, additional black regions show oil, with the additional red showing colloidal particles. Some particles appear inside the ganglion due to the non-zero optical slice thickness. Particles are deposited on the bead surfaces, but do not localize at the ganglion surface, indicating that they are not surface active. Blue regions in (b) and (c) show portions of the ganglion that are mobilized between (a–b) and (b–c). Scale bars represent 250 µm. Imposed flow direction is from left to right.

Next, we consider the possibility of flow redirection as a result of pore clogging. In particular, as particles deposit on the bead matrix, they may constrict and even occlude tight

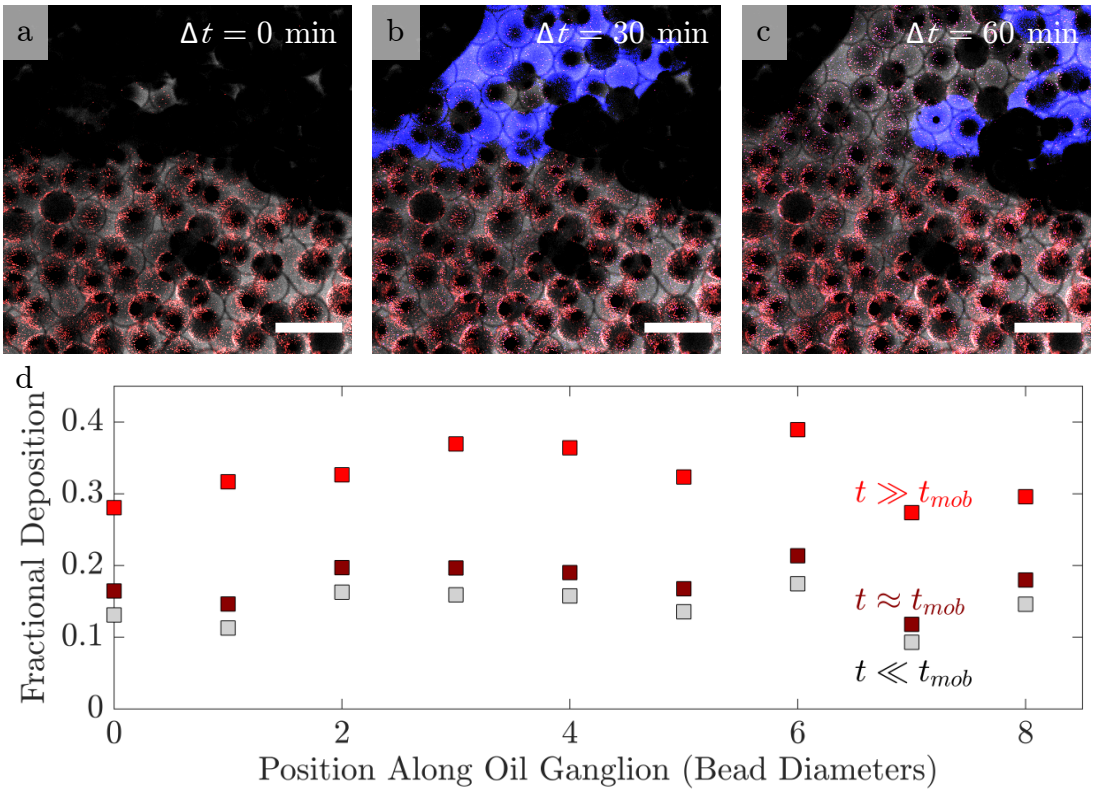


Figure 2.5: Oil mobilization does not occur due to selective clogging of pores driving flow redirection. Magnified views of confocal micrographs show an oil ganglion (a) before, (b) during, and (c) after mobilization. White regions show pore space, black circles show the bead matrix, additional black regions show oil, with the additional red showing colloidal particles. Some particles appear inside the ganglion due to the non-zero optical slice thickness. The appearance of glass beads that are not completely black and have a shaded outline is a result of imperfect index matching between the wetting fluid and the beads. Particles are uniformly deposited on the bead surfaces both along and transverse to the ganglion; we do not observe selective clogging of pores. Blue regions in (b) and (c) show portions of the ganglion that are mobilized between (a–b) and (b–c). Scale bars represent 250 µm. Imposed flow direction is from left to right. (d) Data showing the fraction of the pore space immediately transverse to the ganglion that is occupied by deposited particles, measured using the confocal micrographs at three different times. Grey points correspond to (a), maroon points correspond to (b), and red points correspond to the end of the experiment, shown in Fig. 1e. In all cases, the deposition is uniform across pores.

constrictions, possibly redirecting subsequent flow through the pore space. However, previous studies indicate that this behavior requires a considerable amount of deposition[95,134], which is unlikely to occur given the dilute volume fraction of particles ($< 10^{-2}$ vol%) used in our experiment and the limited overall duration of particle injection. Indeed, as previously determined using experiments on single pores[95], the total number of particles that must flow through each pore to clog it, N^*, can be estimated using the empirical scaling relation $N^* \approx 5,000(2a_t/d_p)^4$, where $2a_t$ and d_p are the diameter of a pore constriction (a "throat") and a particle, respectively. In our experiment, $a_t \approx 0.16a = 11$ μm[135,136] and $d_p = 1$ μm, yielding a threshold number of particles required to clog each pore, $N^* \approx 1 \times 10^9$. By contrast, the characteristic number of particles that flow through each pore over the entire experimental duration—calculated using the imposed flow rate $Q = 0.15$ mL/h, the maximal amount of time during which particles flow through the system $t \approx 10$ h, the number of pore volumes of particle suspension flowed over that time PVs ≈ 65, the suspension volume fraction of 8×10^{-3} vol%, and the individual particle diameter of 1 μm—is $N_{tot} \approx 4 \times 10^8$, much smaller than the estimated N^*. Moreover, the number of particles that flow through each pore before the onset of oil mobilization is even smaller than this value. Thus, clogging is not likely to occur in our experiment.

This expectation is again confirmed by direct inspection of the distribution of particles during ganglion mobilization: we do not observe pore clogging or strong variations in deposition in the different pores away from trapped ganglia, as exemplified by the micrograph shown in Fig. 2.3e, as well as the magnified views of ganglia mobilization shown in Figs. 2.4 and 2.5. The dark region in the top of Fig. 2.5a again shows a portion of a ganglion immediately before it is mobilized; in this case, the ganglion is still trapped in the porous medium 2 h,

or after 13 PVs of further fluid injection, after that shown in Fig. 2.4 is mobilized, resulting in more deposition on the surrounding beads. We again observe little to no particle localization at the ganglion surface, consistent with the results shown in Fig. 2.4. Notably, we do not observe appreciable variations in particle deposition from pore to pore, either along the flow direction or laterally. Further, though they are increasingly constricted, the individual pores still permit fluid flow through them; particles only occupy $< 20\%$ of the available pore space area, as shown by the grey points in Fig. 2.5d determined directly from the confocal micrographs. These features are also apparent in Figs. 2.5b–c, which again show mobilized portions of the ganglion in blue. After the ganglion at the top of the micrograph is mobilized, new particles are re-deposited in its wake, shown by the additional red in the upper region of Fig. 2.5c, helping to even out the spatial variations in permeability. Indeed, during and well after mobilization, we again find that particle deposition is nearly uniform across pores, as shown by the maroon and red points in Fig. 2.5d, consistent with previous findings[137]. Thus, mobilization of trapped oil is not due to selective clogging of pores.

Our visualization of particle deposition reveals that it constricts but does not clog pores throughout the medium—and that the extent of oil mobilization is correlated with the extent of deposition. These observations hint at a different mechanism of oil mobilization. We hypothesize that deposition reduces the permeability of the medium, thereby enabling the viscous stresses exerted by the flowing wetting fluid on the trapped ganglia to overcome the influence of capillarity keeping ganglia trapped. To test this hypothesis, we use our micrographs to estimate the permeability reduction, thereby providing an estimate of how the local viscous stresses are modified, as detailed in the following section.

To accomplish this goal, we first establish the connection between the position- and time-dependent porosity of the medium, $\varphi(x,t)$, and the thickness of the layer of particles deposited on the bead matrix, $\varepsilon(x,t)$; here, x is the position along the imposed flow direction as indicated in Fig. 2.3a and both quantities are averaged laterally over the y direction. In our experiment, we acquire data at a single z-location and assume that φ and ε are uniform in the z-direction, since the medium is randomly packed and previous experiments and simulations have shown the flow to be statistically uniform throughout[138,139].

Our pore-scale visualization of deposition shown in Figs. 2.4, 2.5, and 2.6a indicates that particles are deposited in thin, nearly uniform layers around the spherical glass beads. We rationalize this uniform pore-scale deposition profile by calculating the particle Péclet number, which describes the ratio of advective to diffusive transport, $\mathrm{Pe} \equiv (Q_w/A)/(\mathscr{D}/d_p)$, where Q_w is the imposed flow rate, A is the cross-sectional area of the porous medium, $\mathscr{D}$ is the particle diffusivity, and d_p is the particle diameter. We calculate $\mathscr{D}$ using the Stokes-Einstein equation, $\mathscr{D} = k_B T/3\pi\mu_w d_p$, where k_B is Boltzmann's constant and $T = 300$ K is the temperature of the fluid, yielding $\mathrm{Pe} \approx 100$ for our experiment. While this calculation indicates that advective transport by the mean flow slightly dominates over diffusive transport of single particles, it does not fully capture the complicated flow in a porous medium. Previous measurements indicate that the flow velocities deviate strongly from the mean, in many cases being much smaller[140], particularly upstream of each bead[141], potentially leading to uniform deposition around the beads. This expectation has been confirmed in recent exper-

iments investigating polystyrene particle transport in glass bead packings, which reveal that the interplay between particle interactions and flow limit deposition on the upstream faces of the beads and promote uniform deposition around each bead surface, even at Pe $\gtrsim 100$ [121]. Thus, for simplicity, we approximate deposition at the pore scale to be uniform around the individual beads, with a deposition thickness ε, as schematized in Fig. 2.6b. This thickness is then given by

$$\varepsilon(x,t) \approx a\left[\left(\frac{1-\varphi(x,t)}{1-\varphi_0}\right)^{1/3} - 1\right] \tag{2.1}$$

where φ_0 is the initial porosity before particle injection. We obtain $\varphi(x,t)$ for the oil-free regions of the medium directly from the confocal micrographs using adaptive binarization, restricting all analysis to approximately 5 bead diameters away from the inlet and outlet to minimize the influence of boundaries. Further, to reduce noise, we smooth the porosity measurements by segmenting the porous medium into representative elementary volumes (REV) ≈ 10 bead diameters in length, following common practice [142]. This level of smoothing provides a coarse-grained approach that results in a more realistic permeability estimate, but maintains enough fine-grained detail to incorporate any variations in deposition along the length of the medium. We thereby obtain $\varepsilon(x,t)$, which ranges from 0 to ~ 6 μm over the course of the experiment, from Eq. 2.1.

Next, we use $\varphi(x,t)$ and $\varepsilon(x,t)$ to estimate the permeability, $k(x,t)$, of the oil-free regions of the medium. Because ε is more than an order of magnitude smaller than a, we do this by modifying the classic Kozeny-Carman model, which reasonably predicts the permeability of bead packings similar to those used in our experiment [124,143]. Specifically, following typical convention [144], we model the pore space as a parallel bundle of cylindrical tubes of radius R and length $\ell' > \ell$, where $(\ell'/\ell)^2$ is defined as the hydrodynamic tortuosity τ. The mean flow

speed in each tube, $\langle v \rangle$, is then given by the Hagen-Poiseuille equation:

$$\langle v \rangle \equiv \frac{Q}{\varphi A} = \frac{R^2 \Delta P}{8 \mu_w \ell'} \tag{2.2}$$

where Q is the imposed volumetric flow rate through the entire medium, A is the cross-sectional area of the mediun, φ is the medium porosity, and ΔP is the pressure drop across the entire medium. This mean flow speed is also given by Darcy's law:

$$\langle v \rangle \equiv \frac{Q}{\varphi A} = \frac{k \Delta P}{\varphi \mu_w \ell} \tag{2.3}$$

where k is the overall permeability of the medium. Equating Eqs. 2.2 and 2.3 thus yields a general expression for the permeability:

$$k = \frac{\varphi R^2}{8\tau}. \tag{2.4}$$

Following typical convention [144], we solve for R by equating the hydraulic radii R_h of the tube bundle and the porous medium composed of beads of radius $a + \varepsilon$. For the tube bundle, this quantity is given by the ratio between the pore space cross-section and the wetted perimeter, $R_h = \frac{\pi R^2}{2\pi R} = R/2$. For the porous medium, this quantity is given by the ratio between the pore space volume and the wetted surface area, $R_h = \frac{\varphi A \ell}{N \times 4\pi (a+\varepsilon)^2}$, where $N = \frac{(1-\varphi) A \ell}{\frac{4}{3}\pi (a+\varepsilon)^3}$ is the number of beads in the medium. Thus, equating both expressions for R_h yields

$$R = \frac{2\varphi \, (a + \varepsilon)}{3 \, (1 - \varphi)} \tag{2.5}$$

Finally, substituting Eq. 2.5 into Eq. 2.4 and applying Eq. 2.1 yields the relation

$$k(x,t) = \frac{a^2}{18\tau}\left(\frac{1-\varphi(x,t)}{1-\varphi_0}\right)^{2/3}\frac{\varphi(x,t)^3}{(1-\varphi(x,t))^2} \tag{2.6}$$

where τ is the tortuosity of the pore space, assumed to be equal to 2 for simplicity[140]. This relation quantifies the intuition that as deposition progresses and φ decreases, k decreases as well. Thus, from our measurements of $\varphi(x,t)$, we determine $k(x,t)$ *via* Eq. 2.6.

2.7 Developing a model for deposition-induced mobilization

How does a deposition-induced reduction in permeability promote oil mobilization? To answer this question, we examine the competition between the viscous stress exerted by the flowing wetting fluid on a ganglion and the capillary pressure threshold that must be overcome to displace the ganglion. The gradient in the wetting fluid pressure P_v is given by Darcy's law: $\frac{\partial P_v}{\partial x} = \frac{\mu_w(Q_w/A)}{\kappa k(x,t)}$, where the relative permeability κ is an empirical parameter ≤ 1 used to quantify the modified transport through the medium due to the presence of trapped oil[142]. The viscous pressure drop ΔP_v across a ganglion of length L along the imposed flow direction and with upstream end located a distance x_0 from the inlet can then be approximated as

$$\Delta P_v \approx \frac{\mu_w\,(Q_w/A)}{\kappa}\int_{x_0}^{x_0+L}\frac{\mathrm{d}x}{k(x,t)} \tag{2.7}$$

where the ganglion spans $x_0 \leq x \leq x_0 + L$ as schematized in Fig. 2.6c. To mobilize the ganglion, this viscous pressure drop must be large enough to squeeze the ganglion through the

pores of the medium. Specifically, the ganglion must displace the wetting fluid from a downstream pore, requiring it to overcome the capillary pressure threshold $2\gamma\cos\theta/a_t$, where a_t is the radius of the downstream pore constriction, known as a "throat", schematized in Fig. 2.6b. The ganglion must also be displaced by the wetting fluid from an upstream pore, requiring the capillary pressure within the pore to fall below the threshold $2\gamma\cos\theta/a_b$, where a_b is the radius of the upstream pore, known as a "body". Thus, to mobilize a ganglion from the medium, ΔP_v must exceed the capillary pressure threshold

$$\Delta P_c \approx 2\gamma\cos\theta\left[\frac{1}{a_t(x_0,t)} - \frac{1}{a_b(x_0+L,t)}\right]. \tag{2.8}$$

In previous studies, increasing the viscous stresses on ganglia was accomplished by increasing the wetting fluid flow rate, Q_w, to promote mobilization [105]. Here, we examine another way of increasing these viscous stresses: by depositing particles in the pore space and thereby locally reducing permeability.

In the particle-free case, k, a_t, and a_b are independent of position and time; Eq. 2.7 then reduces to $\Delta P_v \approx \mu_w\,(Q_w/A)\,L/\,(\kappa k_0)$, with the pristine medium permeability k_0 given by substituting $\varphi = \varphi_0$ into Eq. 2.6, and Eq. 2.8 reduces to $\Delta P_c \approx 2\gamma\cos\theta\,(1/a_t - 1/a_b)$. As a simplifying first step—motivated by the fact that our bead packings are comprised of beads with a narrow distribution of sizes—we adopt a mean-field approach for the pristine medium where a_t and a_b are averaged with $a_t \approx 0.16a$ and $a_b \approx 0.24a$ [135,136] instead of explicitly considering the pore-to-pore variation of the pore geometry. Ganglia are only mobilized if

$\Delta P_v \geq \Delta P_c$, or equivalently, if their normalized length $\tilde{L}$ exceeds a threshold value

$$\tilde{L}_{max} = \frac{\kappa k \cos\theta}{a \cdot \mathrm{Ca}} \left(\frac{1}{a_t} - \frac{1}{a_b} \right); \tag{2.9}$$

here, overtildes indicate ganglion lengths that have been normalized by the bead diameter $2a$ and the Capillary number, defined as $\mathrm{Ca} \equiv \mu_w \left(Q_w / A \right) / \gamma$, quantifies the competition between viscous and capillary stresses at the pore scale. This definition is based on the typical convention established in previous studies of flow through porous media [145,146]; it represents a global quantity defined using macroscopically-imposed injection conditions, and in our experiment, $\mathrm{Ca} \approx 4 \times 10^{-6}$ is held constant. Previous permeability measurements performed in a similar porous medium using nearly identical fluids and flow conditions indicate that $\kappa \ll 0.1$ for the range of residual oil saturations explored here [105]. Furthermore, other relative permeability measurements suggest that κ varies only minimally in this range of oil saturations [147–150]. Therefore, for simplicity, we approximate the relative permeability as $\kappa \approx 0.02$—a value that is both consistent with these previous findings and yields the best fit to our data. Using these experimental values, we expect that before particle injection, all ganglia longer than $\tilde{L}_{max} \approx 44$ are mobilized—eventually establishing the initial steady-state configuration of trapped oil shown for $\approx$ 6–50 PVs in Fig. 2.3c and exemplified by the micrograph in Fig. 2.3d. Direct analysis of the confocal micrographs yields excellent agreement with this expectation: we find $\tilde{L}_{max} = 48$ for this steady-state configuration in our experiment, as shown by the first data point in Fig. 2.6d, with all larger ganglia being mobilized in the first $\approx$ 6 PVs of wetting fluid injection. Thus, oil mobilization in a particle-free medium can be quantitatively described through our balance of viscous and capillary stresses.

After particle injection is initiated, k, a_t, and a_b are no longer constant; $k(x,t)$ is given by

Eq. 2.6, while $a_t(x,t) \approx 0.16a - \varepsilon(x,t)$ and $a_b(x,t) \approx 0.24a - \varepsilon(x,t)$, with $\varepsilon(x,t)$ given by Eq. 2.1. In this case, ganglia are again only mobilized if $\Delta P_v \geq \Delta P_c$, but now with ΔP_v and ΔP_c given by Eqs. 2.6 and 2.8, respectively. Thus, we expect that ganglia are mobilized when their length L exceeds a threshold value L_{max} given by the solution to the following integral equation:

$$\int_{x_0}^{x_0+L_{max}} \frac{\mathrm{d}x}{k(x,t)} = \frac{2\kappa\cos\theta}{\mathrm{Ca}} \left[\frac{1}{a_t\left(x_0 + L_{max}, t\right)} - \frac{1}{a_b\left(x_0, t\right)} \right]. \tag{2.10}$$

This equation quantifies the intuition that as colloidal deposition progresses, permeability reduction in the medium increases the viscous stresses on ganglia, decreasing L_{max} and enabling increasingly smaller ganglia to be mobilized from the medium.

We again use our experimental measurements to test this prediction. Because particle deposition is nearly uniform throughout the medium, as shown in Figs. 2.3, 2.4, and 2.5, we average the values of $k(x,t)$ and $\varepsilon(x,t)$ predicted by Eqs. 2.6 and 2.1, respectively, over the entire medium; the averaged values are given by $\overline{k}(t) \equiv \ell^{-1}\int_0^\ell k(x,t)\mathrm{d}x$ and $\overline{\varepsilon}(t) \equiv \ell^{-1}\int_0^\ell \varepsilon(x,t)\mathrm{d}x$, respectively. Substituting these averages in Eq. 2.10 yields a more simplified prediction for the maximal length of a trapped ganglion:

$$\tilde{L}_{max}(t) = \frac{\kappa\overline{k}(t)\cos\theta}{a\cdot\mathrm{Ca}} \left(\frac{1}{\overline{a}_t(t)} - \frac{1}{\overline{a}_b(t)} \right), \tag{2.11}$$

where $\overline{a}_t(t) \approx 0.16a - \overline{\varepsilon}(t)$ and $\overline{a}_b(t) \approx 0.24a - \overline{\varepsilon}(t)$. As before, $\mathrm{Ca} \approx 4\times10^{-6}$ and we choose $\kappa = 0.02$, based on previous measurements obtained for a similar experimental system [105], and consistent with other studies [147–150]. Therefore, substituting the experimental values into Eq. 2.11, we expect that as particles are injected into the porous medium, all

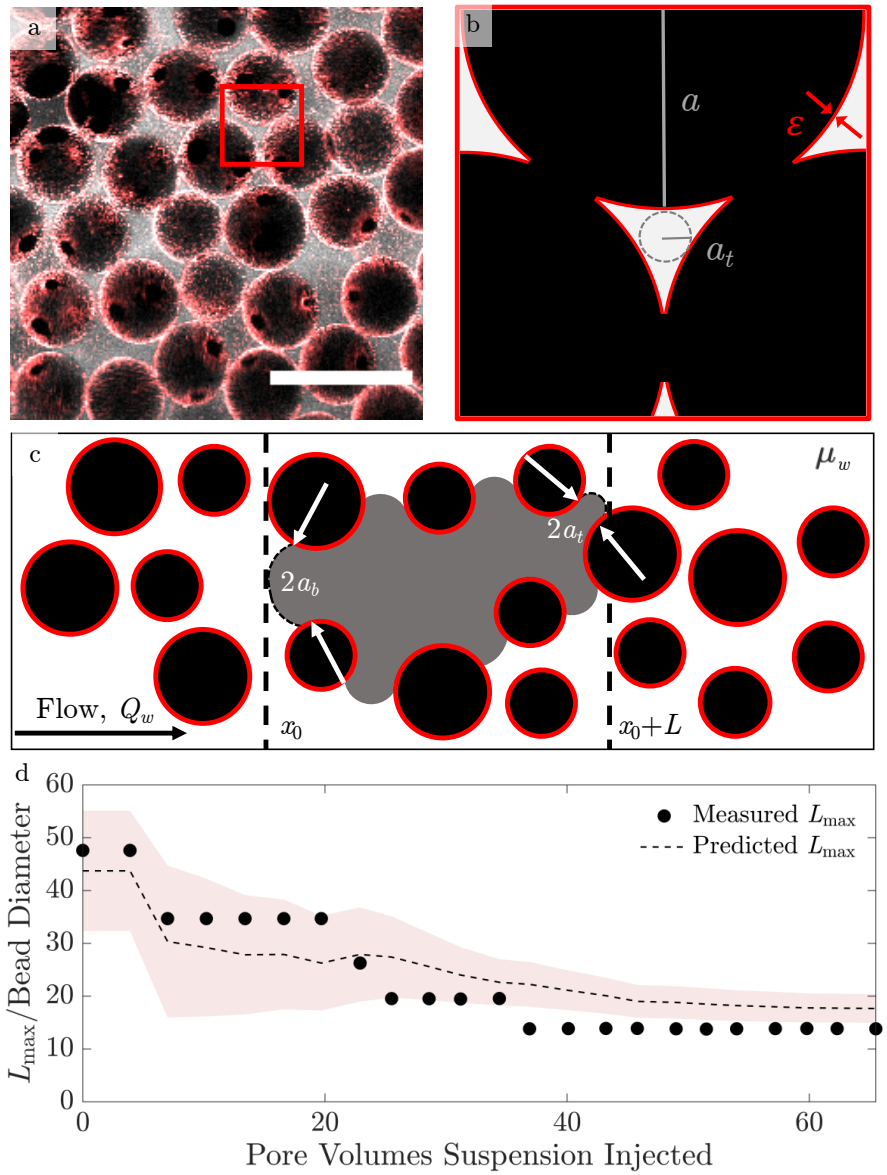


Figure 2.6: Permeability reduction due to colloidal deposition promotes oil mobilization. (a) Magnified view of a confocal micrograph of colloidal deposition. Gray regions show pore space, black circles show the bead matrix, and red indicates deposited colloidal particles. Scale bar represents 250 μm. Imposed flow direction is from left to right. (b) Schematic of a pore throat of radius a_t, showing a uniform layer of deposited particles of thickness ε. (c) Schematic of a trapped oil ganglion. The grains that comprise the porous medium are shown black with red outlines to indicate deposition. The pore body and pore throat diameters, $2a_b$ and $2a_t$, are indicated at the upstream and downstream ends of the trapped ganglion. We also indicate the wetting fluid flow rate, Q_w and viscosity, μ_w. (d) Confocal measurements of the maximal length along the flow direction of trapped ganglia, L_{max}, over the course of colloidal injection. The initial point corresponds to Fig. 2.3d. As deposition progresses, smaller ganglia are mobilized from the medium. Dashed line shows our theoretical prediction of L_{max} from Eqs. Eq. 2.10 and 2.11. The red region shows uncertainty in the prediction arising from heterogeneities in the deposition profile.

ganglia longer than $\tilde{L}_{max}$ are mobilized, with $\tilde{L}_{max}$ decreasing from $\approx$ 44 to $\approx$ 18 as deposition progresses, indicated by the dashed line in Fig. 2.6d. That is, with increasing amounts of colloidal deposition, we expect that increasingly smaller ganglia can be mobilized from the medium. Direct analysis of the confocal micrographs again yields excellent agreement with this expectation: remarkably, we find that $\tilde{L}_{max}$ decreases from 48 to 15 over the course of the experiment, as shown by the data points in Fig. 2.6d, reaching the final steady state after $\approx$ 40 PVs of suspension are injected. Thus, the configurations of ganglia mobilized through colloidal deposition can be quantitatively described through our balance of viscous and capillary stresses.

The approach to steady state in Fig. 2.6d is strikingly similar to that shown by the black points in Fig. 2.3c. Indeed, as a final test of our theory, we predict not just the maximal length of trapped ganglia, but the total amount of trapped oil, S_{OR}. We do this using our confocal micrographs by summing the pore space area occupied by all ganglia with lengths $\tilde{L}$ less than the $\tilde{L}_{max}$ value predicted by Eq. 2.11, at each experimental time point. The predicted S_{OR} is shown by the dashed line in Fig. 2.3c. We again observe excellent agreement between the measured and predicted S_{OR}; both decrease over the course of colloidal injection and deposition, ultimately leading to $S_{OR} \approx 20\%$ of its maximal value. Thus, the extent of deposition-induced oil mobilization can also be quantitatively described through our balance of viscous and capillary stresses.

2.8 Implications of deposition-enhanced mobilization

This chapter reveals that particle deposition can promote mobilization of trapped oil ganglia from a porous medium. In particular, by reducing the local permeability, particle deposition increases the viscous stresses on ganglia, enabling them to overcome the influence of capillary stresses that keep them trapped. To identify the essential physics of this problem, our theory adopts a mean-field representation of the medium as a simplifying first step. Nevertheless, it yields predictions for the size and amount of mobilized fluid. Both of these quantities are in good agreement with the experimental measurements; however, incorporating spatial variations in pore geometry will be a useful next step that builds on the current work.

To highlight the impact of permeability reduction on enhanced mobilization, we can also contrast a porous medium in which particle deposition alters the porosity to that of a medium in which the pores have simply become uniformly smaller. If we consider the case of a pristine porous medium with smaller pores, the viscous pressure drop across a trapped ganglion of length L, given by $\Delta P_v \propto L/k$, is larger because k scales as a^2, where a is the bead radius. However, it is important to note here that the capillary pressure threshold that must be overcome to mobilize the ganglion, given by $\Delta P_c \propto 1/a$, is also larger in a medium with smaller pores. Balancing the two confirms that the normalized threshold ganglion length, $L_{max}/2a$, is a constant and is thus unchanged when pore size is reduced, as one may expect. However, in the case of a porous medium in which particle deposition has altered both the effective grain size a and the porosity φ, the permeability decreases more than the capillary pressure threshold due to its dependence on porosity. The capillary pressure threshold increases as $1/(a + \varepsilon)$; however, this increase is not sufficient to overcome the increase in the viscous

pressure drop due to the decrease in permeability, which decreases as $(a+\varepsilon)^2\varphi^3/(1-\varphi)^2$. Specifically, $\Delta P_v \propto \frac{L}{(a+\varepsilon)^2}\frac{(1-\varphi)^2}{\varphi^3}$ and $\Delta P_c \propto a/(a+\varepsilon)$; balancing the two in this case yields a normalized threshold ganglion length $\frac{L_{max}}{2(a+\varepsilon)} \propto \frac{\varphi^3}{(1-\varphi)^2}$ that is not a constant, but also reduces when porosity is reduced.

It is also worth noting that our analysis only describes the *onset* of ganglion mobilization, but does not consider subsequent ganglion dynamics. For example, we assume that as ganglia are mobilized, they do not interact with other ganglia as they traverse the porous medium, though coalescence is possible. As a result, ganglia that are smaller than the threshold predicted by our theory could be mobilized, potentially explaining the slight mismatch between our predicted values and measurements of the residual oil saturation at later times: specifically, our theory slightly over-predicts the measurements shown by the black points for $\sim 80-100$ injected PVs in Fig. 2.3c. Additionally, it is possible that despite the strong attractive interactions between particles and glass beads, mobilized ganglia can remove some deposited particles *via* capillary forces. This removal would result in a temporary increase in local permeability until particles re-deposit there; we then expect that after sufficient re-deposition of particles, new ganglia can be mobilized, potentially enabling this process to repeat itself. We explore this ability of traveling fluid interfaces to remove deposited colloidal particles *via* capillary forces later in this dissertation, in Chapters 4 and 5.

This cyclic process could underlie the fluctuations in the overall amount of deposition measured at early times in our experiment, shown by the slight oscillations in the grey points for $\sim 60-80$ injected PVs in Fig. 2.3c. It could also explain the slight mismatch between the predicted values and experimental measurements of the residual oil saturation at these times, shown by the dashed line and black points, respectively: because removal of particles

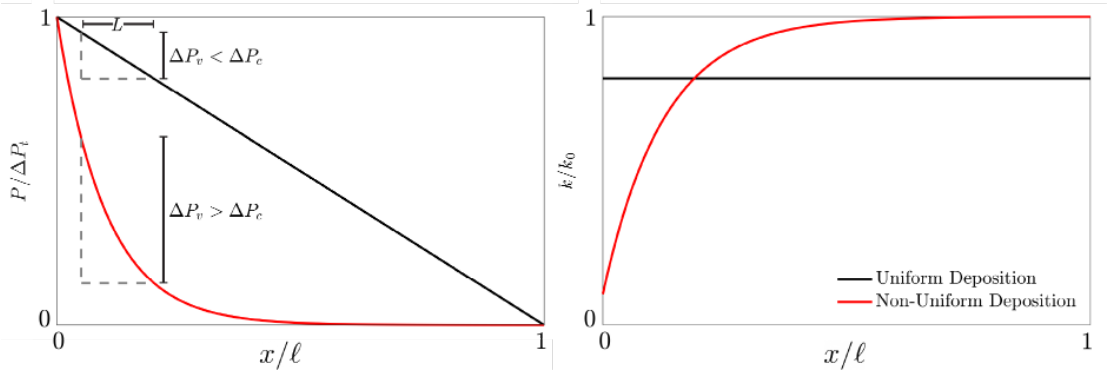


Figure 2.7: Non-uniform deposition promotes mobilization under constant pressure drop ΔP_t. (left) Fluid pressure normalized by the pressure drop ΔP_t. A ganglion of length L has ΔP_v less than ΔP_c when particle deposition is spatially uniform at a low fixed ΔP_t (black). However, a non-uniform deposition profile obtained at the same constant ΔP_t can result in an increase of ΔP_v greater than ΔP_c (red). (right) The corresponding profiles of normalized permeability, k/k_0, are shown over the length of the porous medium, x/ℓ.

through ganglion mobilization would result in a temporary increase in local permeability until particles re-deposit there, mobilization of subsequent ganglia could be under-predicted by our theory, or could take longer than we predict. Elucidating these complex dynamics will be an important direction for future work.

Finally, we note that while this chapter has focused on the flow rate-controlled case, our results can also be modified to consider pressure-controlled flow. To modify our theory for the case of a constant imposed pressure drop, ΔP, we consider both uniform and non-uniform deposition of particles along the flow direction. Though we do not expect to see enhanced mobilization in the case of uniform particle deposition under a constant imposed pressure drop, particle deposition may still induce mobilization in the case of non-uniform (*i.e.*, localized) deposition. An example is sketched in Fig. 2.7. Here, we contrast a uniform deposition profile (black curves) under a constant total pressure drop across the medium, ΔP_t, with a non-uniform deposition profile in which more particles are deposited near the inlet of the medium (red curves). The corresponding permeability curves, k/k_0, where k_0 is the perme-

ability of the pristine medium, are shown in the lower panel of the figure; uniform deposition corresponds to a uniform k along the medium (black curve), while non-uniform deposition results in lower k near the inlet (red curve), where x is the position along the medium and ℓ is its length. The resultant variation of the fluid pressure $P/\Delta P_t$ along the porous medium is shown by the plot in the top panel.

In the case of uniform deposition at constant ΔP_t, the flow rate Q decreases concomitantly with increasing deposition. As a result, the viscous stress over a ganglion would not vary considerably, and thus new ganglia are not likely to be mobilized once deposition begins. An example of a ganglion of length L is shown by the horizontal dashed line in the top panel of the figure; the vertical bar indicates the viscous pressure drop across it, ΔP_v, which in this case is not sufficient to exceed the capillary pressure drop ΔP_c, and it remains trapped. As uniform deposition progresses, this viscous pressure drop does not change, and the ganglion still remains trapped. However, in the case of a non-uniform deposition profile, due to the non-uniform pressure gradient along the medium, the viscous pressure drop along the same ganglion is much larger and exceeds ΔP_c, as indicated by the lower vertical bar. In this case, the ganglion becomes mobilized. Thus, even in pressure-controlled flow, particle deposition can induce mobilization when it is non-uniform.

While our experiments focus on the flow-controlled case, our theoretical analysis can be adopted to model the case of mobilization under pressure-controlled flow due to non-uniform deposition. Specifically, Eq. 2.7 would be modified:

$$\Delta P_v = \frac{\mu_w}{A} \int_{x_0}^{x_0+L} \frac{Q_w(x,t)}{k'(x,t)} \mathrm{d}x \tag{2.12}$$

where $k'(x,t) = \kappa(x,t)k(x,t)$. Here, we have two unknowns, Q and k'. However, we also

have another relationship that comes from the overall constant pressure drop criterion as follows:

$$\Delta P_t = \text{const.} = \frac{\mu_w}{A} \int_0^\ell \frac{Q_w(x,t)}{k'(x,t)} \mathrm{d}x \tag{2.13}$$

Using these modified equations with Eq. 2.8 would then provide a modified criterion for ganglion mobilization *via* particle deposition under a constant imposed pressure drop.

2.9 Conclusions

Colloidal deposition in porous media is often considered to be a critical problem or, at best, a nuisance for applications including groundwater remediation and enhanced oil recovery; the permeability reduction resulting from deposition is thought to detrimentally impede subsequent flow and particle transport. This chapter revealed that colloidal deposition can in fact be harnessed to mobilize and remove trapped immiscible fluids from a porous medium. In particular, we found that through deposition, a dilute ($< 10^{-2}$ vol%) suspension of particles can mobilize and remove an additional $\sim 70\%$ of trapped fluid from a porous medium. Pore-scale visualization demonstrated that this mechanism of mobilization does not require colloidal surface activity or selective clogging of pores; instead, by reducing the local permeability, deposited particles increased the viscous stresses exerted on trapped fluid droplets by the surrounding fluid, enabling them to become mobilized. By analyzing the colloidal deposition profile and the pore-scale fluid stresses, we developed a geometric model that predicts which fluid droplets become mobilized, depending on their size (Eq. 2.10)—in excellent agreement with our experimental results. Further, for a given starting distribution of trapped

droplet sizes, this model enabled us to predict the extent of fluid that is mobilized as deposition progresses—again in excellent agreement with our experimental results. In the future, this model can also be used to guide applications requiring a target amount of trapped fluid to be mobilized: given a desired value of S_{OR}, Eqs. 2.6 and 2.10 can be inverted to determine the extent of colloidal deposition required. Thus, in addition to shedding light on a new way by which colloids can mobilize trapped fluid from a porous medium, this chapter provides quantitative guidelines for applying this mechanism. Because it does not require specialized physico-chemical characteristics, we expect this mechanism could be utilized in diverse media of different structures, and applicable to colloids of differing chemistry and physical characteristics, including naturally-occurring organic and inorganic colloids e.g., "fines".

2.10 Supplementary Movie Captions

The movies corresponding to data in this chapter can be found with the online version of Bizmark *et al* (DOI: 10.1126/sciadv.abc2530)[2], and are duplicated in the repository at: https://github.com/joannaclaireschneider/dissertation-movies.

Movie S1. Extended deposition of amine-functionalized polystyrene particles injected at 260 kPa. Black circles show cross sections through the beads making up the porous medium, white space shows pore space, and red shows deposited colloidal particles. For clarity, we only show the deposition profile for the first 4,000 μm of the medium. Flow direction is from left to right.

Movie S2. Monotonic deposition of amine-functionalized polystyrene particles upstream of a bead during injection at 260 kPa. Black circles show cross sections through the beads making up the porous medium, white space shows pore space, and red shows deposited colloidal particles. Flow direction is from left to right.

Movie S3. Cyclic deposition and erosion of amine-functionalized polystyrene particles upstream of a bead during injection at 260 kPa. Black circles show cross sections through the beads making up the porous medium, white space shows pore space, and red shows deposited colloidal particles. Flow direction is from left to right.

Movie S4. Localized deposition of amine-functionalized polystyrene particles injected at 80 kPa. Black circles show cross sections through the beads making up the porous medium, white space shows pore space, and red shows deposited colloidal particles. For clarity, we only show the deposition profile for the first 4,000 μm of the medium. Flow direction is from left to right.

Sometimes there is dogma in baking

and sometimes there is not,

you just have to know when to break the rules

and when to follow them.

Claire Saffitz

3

Improving fluid mobilization predictions in stratified porous media

In Chapter 2, we demonstrated one mechanism by which colloids may be used to aid in mobilization of an immiscible fluid from a porous medium. By harnessing colloidal

deposition, we showed that the viscous pressure drop across a trapped droplet, or ganglion, increases due to a decrease in the medium's overall permeability. Thus, the maximum length of trapped ganglia, L_{max}, decreases because $L_{max} \propto k$. Of course, decreasing the permeability of a porous medium is not the only way to decrease L_{max}. Most approaches that have been developed to enhance mobilization of trapped fluids focus on tactics to lower L_{max} by increasing the capillary number, Ca, because $L_{max} \propto 1/\mathrm{Ca}$.

Increasing Ca indicates that viscous forces due to flow become more prominent and thus dominate over capillary forces at the pore scale, ultimately allowing trapped ganglia to be mobilized [105,145,146,151–153]. For example, colloids that can localize at immiscible fluid interfaces decrease the interfacial tension between the fluids, γ, and thereby increase Ca. However, in the absence of colloids or other additives, a common approach taken for immiscible fluid mobilization in energy and environmental applications is simply to inject water at the highest achievable Ca in a process called "water-flooding." The impact of changing Ca on overall trapped oil mobilization can then be measured over time by quantifying the amount of the pore space occupied by the non-wetting fluid, or the residual oil saturation (S_{OR}).

This method of water-flooding is often successful in homogeneous porous media, which have randomly distributed pore sizes centered around a single mean and lack spatial correlations between neighboring pores [105,154–156]. These features also allow for averaged approximations of their physical characteristics to be made; however, when applied to heterogeneous media, this method often exhibits varying degrees of success. One case where this approach

---

This chapter has been adapted from unpublished work by Joanna Schneider, Nancy B. Lu, and Sujit S. Datta. **Author Contributions:** J.S. and N.B.L. developed the theory; J.S. analyzed the data and implemented the theoretical model. S.S.D. designed and supervised the overall project. All authors discussed the results and wrote the manuscript.

is not as effective is in heterogeneous media comprised of stratified layers parallel to the flow direction. These stratified media are ubiquitous in nature and are formed by geological processes. Here, each stratum is characterized by its own distinct mean pore size [157–160] and the existence of distinct strata can impact interfacial dynamics in complex ways [157–164]. For example, oil recovery is often not as efficient as predicted when oil reservoirs are stratified because water breaks through earlier in higher permeability regions [165].

The inability of this averaged approach to capture immiscible, or non-wetting ganglia mobilization in stratified media suggests that averaging the properties of individual strata is not sufficient to describe the stratified porous medium's properties or the physical processes that occur within them. Therefore, obtaining better predictions of non-wetting fluid mobilization in stratified porous media is of both fundamental and practical importance. Thus, in this chapter, we address the limitations of averaging geometric properties of stratified porous media, by developing a theoretical model that considers the properties of both strata individually as well as the coupling between them. We then examine the mobilization of trapped non-wetting fluid ganglia from each stratified layer, comparing the predicted steady state S_{OR} to that predicted by the averaged model.

Importantly, we find that averaging the properties of a stratified medium frequently *overpredicts* the total amount of non-wetting fluid removed from the medium when compared to predictions that consider strata independently. We generalize our findings by exploring a wide range of three key structural parameters: the grain size ratio between strata, a_c/a_f, the width ratio between strata, W_c/W_f, and the non-dimensional length of the porous medium, ℓ/W. This chapter thus provides quantitative guidelines to produce better predictions of non-wetting fluid mobilization in stratified porous media with a wide range of properties,

which is of critical importance for recovering trapped immiscible fluid in stratified oil reservoirs and groundwater aquifers.

3.1 Developing criteria for stratum-dependent mobilization

To theoretically study non-wetting fluid mobilization from a stratified porous medium, we adapt established criteria for mobilization in homogeneous porous media. Critically, we account for the distinct properties of each stratum in the stratified medium by considering two homogeneous media in parallel (Fig. 3.1a). Each stratum is defined by a set of known parameters, including its cross-sectional area, A_i, grain radius, a_i, absolute permeability, k_i, and relative permeability, κ_i, where each layer i is described by its own distinct structural parameters. We denote one stratum as the "fine" stratum and the other as the "coarse" stratum, in which the fine stratum has a grain radius smaller than that of the coarse stratum, $a_f < a_c$. Because we consider each stratum separately, we can employ a simple stress balance on trapped non-wetting ganglia in each stratum to determine the threshold length of droplets that remain trapped in each stratum, L_{max}. To establish this criterion, we set the viscous pressure drop across a trapped ganglion, ΔP_v, equal to the capillary pressure threshold that holds it in place, ΔP_c.

The gradient in the wetting fluid pressure P_v is given by Darcy's law: $\frac{\partial P_v}{\partial x} = -\frac{\mu_w (Q_w/A)}{\kappa k}$, where the relative permeability κ is ≤ 1 and is defined by an empirical relationship[150], $\kappa = \left(\frac{0.915 - S_{OR}}{0.915}\right)^{2.394}$, the permeability k is given by the Kozeny-Carman model[166,167], $k = \frac{a^2}{45\tau}\frac{\varphi^3}{(1-\varphi)^2}$, where φ is the porosity of the system, τ is the tortuosity, and a is the mean grain radius within

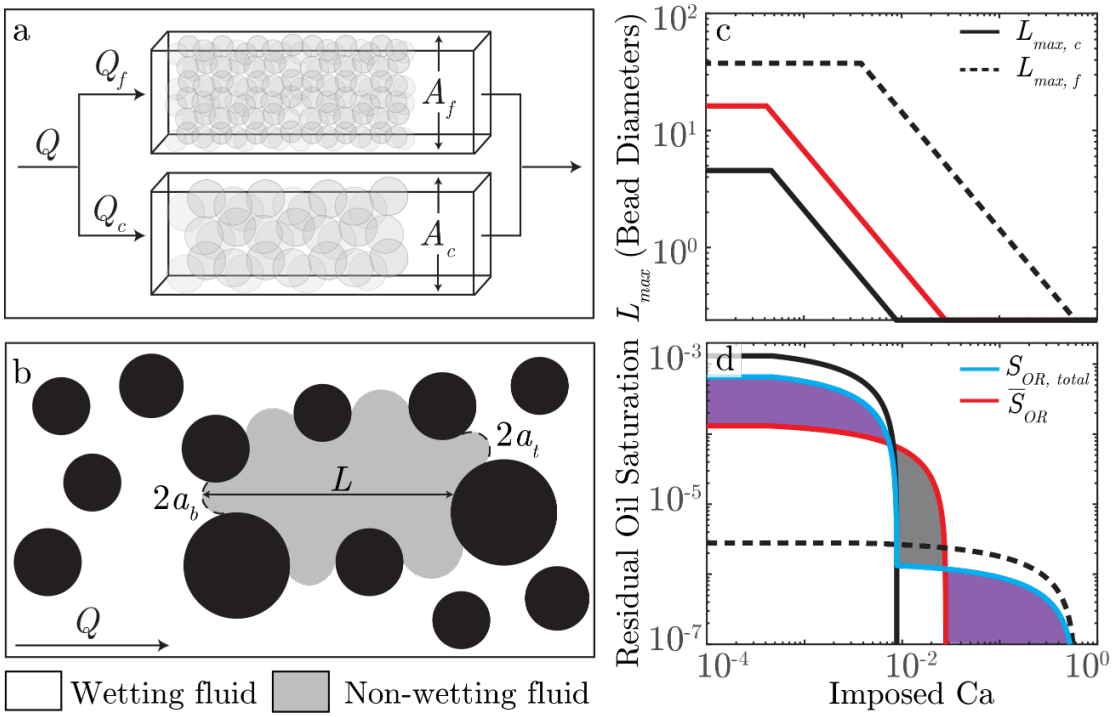


Figure 3.1: Setup of a theoretical model and discrepancies between predictions using averaged versus stratified properties. (a) The stratified medium is modelled as two independent, homogeneous porous media with an imposed flowrate Q, that is distributed across the fine and coarse strata as Q_f and Q_c, respectively. Each stratum, i, is described using structural parameters $A_i, r_i, k_i, \kappa_i, \varphi_i$, where A_i is the cross-sectional area of a stratum, a_i is its mean grain radius, k_i is its absolute permeability, κ_i is its relative permeability, and φ_i is its porosity. (b) Schematic of a trapped non-wetting fluid ganglion. A trapped non-wetting fluid ganglion with length L along the flow direction is shown in gray, with pore body and pore throat diameters, $2a_b$ and $2a_t$, respectively, indicated at the upstream and downstream ends of the trapped ganglion by black dashed lines. (c) Predicted $L_{\max}$ as a function of imposed Ca. Calculating L_{max} with averaged properties (red line) overpredicts coarse stratum mobilization (solid black line) and underpredicts fine stratum mobilization (dashed black line). (d) Residual non-wetting fluid saturation (S_{OR}) as a function of imposed Ca. Comparing the predicted stratified total S_{OR} (blue line) with the predicted averaged total S_{OR} (red line) reveals imposed Ca ranges where averaging overpredicts (purple) and underpredicts (gray) mobilization.

that stratum. By assuming a constant pressure gradient, we approximate the viscous pressure drop ΔP_v across a ganglion of length L along the imposed flow direction as $\Delta P_v \approx \frac{\mu_w (Q_w/A) L}{\kappa k}$.

As detailed in Chapter 2 and established experimentally[105,145,146], we define the capillary pressure threshold, ΔP_c, as the difference between P_c at the trapped ganglion's downstream- and upstream-most pores. At its most downstream position, flow must overcome a capillary pressure $2\gamma \cos\theta / a_t$, where θ is the three-phase contact angle and $a_t \approx 0.16a$ is the radius of the downstream pore constriction, known as a pore "throat". At its most upstream position, P_c within the pore must fall below the threshold $2\gamma \cos\theta / a_b$, where $a_b \approx 0.24a$ is the radius of the upstream pore, known as a pore "body". The capillary pressure threshold ΔP_c across a ganglion of length L is then defined as $\Delta P_c \approx 2\gamma \cos\theta \left[\frac{1}{a_t} - \frac{1}{a_b}\right]$.

When $\Delta P_v > \Delta P_c$ trapped non-wetting fluid ganglia whose lengths exceed the threshold set by the flow conditions and system geometry are mobilized, while those whose lengths fall below that threshold remain trapped, as schematized in Fig. 3.1c. We solve for this threshold length, L_{max} by setting $\Delta P_v = \Delta P_c$,

$$L_{max}(\mathrm{Ca}) = \frac{2\kappa k \cos\theta}{\mathrm{Ca}} \left(\frac{1}{a_t} - \frac{1}{a_b}\right) \tag{3.1}$$

where L_{max} is a function of the Capillary number, $\mathrm{Ca} \equiv \mu_w (Q/A)/\gamma$, which describes the ratio of viscous to capillary forces exerted on a trapped non-wetting fluid ganglion. Here, μ_w is the wetting fluid dynamic shear viscosity, Q is the volumetric flowrate in the porous medium, and γ is the interfacial tension between the wetting and non-wetting fluids. Importantly, as Ca increases, we predict that L_{max} will decrease. In this system, we set the maximum value of L_{max} to be equal to the width of the medium, W, because a trapped ganglion in a stratified medium cannot be larger than its smallest dimension and $W \ll \ell$, where ℓ is the length of

the porous medium in the direction of flow.

To isolate the resultant decrease in L_{max} in each stratum, we must calculate Q_{eff} from the imposed flowrate Q for both the fine and coarse strata. Since the pressure drop is imposed along the length of the porous medium and we consider stratification along the flow direction, we can define the following relationship from Darcy's law

$$\frac{\mu_w(Q_i/A_i)}{\kappa_i k_i} = \ldots = \frac{\mu_w(Q_n/A_n)}{\kappa_n k_n} \tag{3.2}$$

where the imposed flowrate, Q, must be equal to the sum of the flowrates in each stratum, $\sum_{i=1}^{n} Q_i$. As a respresentative example, we consider the case of two strata, which allows us to extract Q_f and Q_c as functions of the medium's structural properties and the imposed flowrate, Q.

$$Q_f = \frac{Q}{\frac{A_c\kappa_c k_c}{A_f\kappa_f k_f} + 1} \tag{3.3a}$$

$$Q_c = Q\left(1 - \frac{1}{\frac{A_c\kappa_c k_c}{A_f\kappa_f k_f} + 1}\right) \tag{3.3b}$$

This relationship allows us to explicitly solve for L_{max} in both the fine and coarse strata individually to obtain $L_{max,f}$ and $L_{max,c}$, respectively. Again, as a respresentative example, we choose experimental values from our previous work in which the width ratio of strata $W_c/W_f = 1$, the grain size ratio between strata $a_c/a_f = 8$, and the non-dimensional length $\ell/W = 0.2$ [168]. When we compare the predicted values of L_{max} for each stratum to each other, we observe that the fine stratum requires $\mathrm{Ca} \approx 4 \times 10^{-3}$ to begin mobilizing ganglia with lengths smaller than W, while ganglia smaller than W in the coarse stratum only begin

to get mobilized at Ca over an order of magnitude higher, at Ca $\approx 5 \times 10^{-4}$ (Fig. 3.1c). Furthermore, the values of Ca required for complete mobilization in the fine and coarse strata (*i.e.*, $L_{max} \leq 2a_b$) differ by a factor of nearly 10^2.

3.2 Comparison to averaged approximation of mobilization

The differences in mobilization criteria between the fine and coarse strata become even more apparent when we compare these results to what we obtain for a medium whose properties are a weighted average of the coarse and fine stratum's properties. To obtain averaged properties, the porous medium is assumed to have a permeability, $\overline{k}$, which is a weighted average of the permeabilities, k, of both strata based on their cross-sectional area

$$\overline{k} = \frac{\sum_{i=1}^{n} k_i A_i}{\sum_{i=1}^{n} A_i} \tag{3.4}$$

where n is the number of strata, k_i is the permeability of stratum i as defined by the Kozeny-Carman model, and A_i is its cross-sectional area. The average grain size, $\overline{a}$, is defined similarly as a weighted average of grain sizes in the medium based on cross-sectional area

$$\overline{a} = \frac{\sum_{i=1}^{n} a_i A_i}{\sum_{i=1}^{n} A_i} \tag{3.5}$$

where a_i is the grain radius of stratum i. We can now use the averaged structural properties of the medium, $\overline{k}$ and $\overline{a}$, to calculate $\overline{L}_{max}$ using Eq. 3.1 as follows

$$\overline{L}_{max} = \frac{2\kappa\overline{k}\cos\theta}{\mathrm{Ca}}\left(\frac{1}{\overline{a}_t} - \frac{1}{\overline{a}_b}\right) \tag{3.6}$$

where Ca is calculated using the imposed flowrate Q and the total cross-sectional area A, $\overline{a}_t = 0.16\overline{a}$ is the averaged pore throat size, and $\overline{a}_b = 0.24\overline{a}_b$ is the averaged pore body size.

Using Eq. 3.6 to approximate a stratified medium as a homogeneous porous medium with averaged structural properties predicts that $\overline{L}_max$ at Ca $\approx 4 \times 10^{-3}$ is only 2 grain diameters in length, while the stratified model reveals that ganglia in the fine stratum will still be almost 40 grain diameters in length. This discrepancy is also mirrored when the averaged model predicts complete mobilization; here, the averaged model predicts complete mobilization at Ca $\approx 3 \times 10^{-2}$, while the stratum-specific analysis reveals that ganglia in the fine stratum will still be approximately 5 grain diameters long.

This analysis points to important implications for the predicted values of residual oil saturation (S_{OR}), which quantifies the fraction of the fluid space occupied by non-wetting fluid in the porous medium. Overprediction in L_{max} corresponds to overprediction in the amount of trapped non-wetting fluid mobilized and thus an underprediction of the residual oil saturation. Our subsequent theory presents a mathematical link between predicted L_{max} values as a function of Ca and the resultant S_{OR}, which quantifies the impact of averaging structural properties of a stratified porous medium on the accuracy of S_{OR} predictions.

To calculate the residual oil saturation, S_{OR}, as a function of L_{max}, we assume that the volume of a ganglion, s, can be related to its length, L, by a power law, such that $s \propto L^{\alpha}$, where α is a scaling exponent. Then, we establish a probability density function (*p.d.f.*) to describe the volume distribution of trapped ganglia within a porous medium, which has previously been shown to result in a power law distribution at steady state[105,169–174]. We define this probability density function $p(s) \propto s^{-\tau}$, where τ is also a scaling exponent.

We develop explicit equations for each of these proportionalities by assuming $s = s_0 L^{\alpha}$ and $p(s) = p_0 s^{-\tau}$, where s_0 and p_0 are scalar normalization constants. We first obtain s_0 using a physical constraint of the system: we know the minimum trapped ganglion volume, $s_{min} = V_{body}$, where V_{body} is the volume of a pore body. Thus, we can solve for s_0, which occurs when $s(L = L_{min}) = V_{body}$. We then obtain the following explicit equation for s:

$$s = V_{body} \left(\frac{L}{L_{min}} \right)^{\alpha} \tag{3.7}$$

where L_{min} is a pore body diameter, $2a_b$. Next, we solve for p_0 using the criterion for establishing a probability density function: $\int_0^{\infty} p(s) \mathrm{d}s = 1$. Here, we define $p(s)$ as a piece-wise function because $p(s)$ is bounded by a minimum volume $s_{min} = V_{body}$ and a maximum vol-

ume $s_{max} = s(s = L_{max})$, where $L_{max} = W$.

$$p(s) = \begin{cases} 0 & s < s_{\min} \\ p_0 s^{-\tau} & s_{\min} \leq s \leq s_{\max} \\ 0 & s > s_{\max} \end{cases} \tag{3.8}$$

We can now solve for p_0 explicitly by integrating $p(s)$ from s_{min} to s_{max} to obtain a final expression for the volume distribution of trapped ganglia in a porous medium of length ℓ.

$$p(s) = \frac{1-\tau}{V_{body}^{1-\tau}\left(\left(\frac{W}{2a_b}\right)^{\alpha(1-\tau)} - 1\right)} s^{-\tau} \tag{3.9}$$

With explicit expressions for s (Eq. 3.7) and $p(s)$ (Eq. 3.9), we can solve for the total volume of non-wetting fluid, V_{nw}, and therefore the residual oil saturation, S_{OR}. We obtain V_{nw} by solving for the expected value of the volume of non-wetting fluid, $\mathrm{E}[V_{nw}]$,

$$V_{nw} = \int_{s_{min}}^{s_{max}} s p(s) \mathrm{d}s \tag{3.10}$$

where $s_{min} = V_{body}$ and $s_{max} = s\,(L = L_{max}(\mathrm{Ca}))$. Using the appropriate bounds and substituting Eq. 3.9 for $p(s)$ yields an equation for for V_{nw}

$$V_{nw} = \frac{1-\tau}{V_{body}^{1-\tau}\left(\left(\frac{W}{2a_b}\right)^{\alpha(1-\tau)} - 1\right)} \int_{V_{body}}^{V_{body}\left(\frac{L_{max}(\mathrm{Ca})}{2a_b}\right)^{\alpha}} s^{1-\tau} \mathrm{d}s \tag{3.11}$$

which we can solve as a function of $L_{max}(\mathrm{Ca})$ as follows,

$$V_{nw} = V_{body}\frac{1-\tau}{2-\tau}\left(\frac{\left(\frac{L_{max}(\mathrm{Ca})}{2a_b}\right)^{\alpha(2-\tau)}-1}{\left(\frac{W}{2a_b}\right)^{\alpha(1-\tau)}-1}\right) \tag{3.12}$$

Percolation theory predicts that $\alpha = 3/(\tau-1)$ and $\tau \approx 2.2$ [105,169–171], so Eq. 3.12 can be simplified

$$V_{nw} = V_{body}\frac{1-\tau}{2-\tau}\left(\frac{\left(\frac{L_{max}(\mathrm{Ca})}{2a_b}\right)^{3(2-\tau)/(\tau-1)}-1}{\left(\frac{W}{2a_b}\right)^{-3}-1}\right) \tag{3.13}$$

where $\tau \approx 2.2$. The volume of trapped non-wetting fluid present in the porous medium (Eq. 3.13) can then easily be related to S_{OR} by normalizing V_{nw} by the volume of the enitre fluid space, $\varphi A\ell$, where φ is the porosity of the porous medium, A is its cross-sectional area, and ℓ is its length.

$$S_{OR} = \frac{\sum_{i=1}^{n} V_{nw,i}}{\varphi A\ell} \tag{3.14}$$

Here, i represents each individual stratum and n is the total number of stratum. For a porous medium containing one fine and one coarse stratum, the above equation becomes

$$S_{OR} = \frac{V_{nw,f} + V_{nw,c}}{\varphi A\ell} \tag{3.15}$$

where f and c represent the fine and coarse stratum, respectively.

Using Eq. 3.1, we can now compute the predicted residual oil saturation for a stratified medium using the properties of its individual strata versus a weighted average of stratum properties. At low imposed Ca, we observe that averaging overpredicts the amount of non-

wetting fluid removed from the medium when compared to the prediction that accounts for individual strata by approximately a factor of 5 until it reaches the threshold for complete mobilization in the coarse stratum, Ca_c^* (Fig. 3.1d). At this threshold, Ca is less than the critical Ca required to mobilize all non-wetting fluid from the fine stratum (Ca_f^*) and greater than the critical Ca required to mobilize all non-wetting fluid in the coarse stratum (Ca_c^*), so averaging underpredicts mobilization because this model cannot take into account that all non-wetting fluid has been removed from the coarse stratum. However, once $\mathrm{Ca} > \mathrm{Ca}_f^*$, averaging overpredicts mobilization once again because the averaged grain radius, $\overline{a}$, is always larger than the fine stratum's grain radius, a_f. Moreover, using the averaged model predicts complete mobilization at a value of Ca nearly 20 times lower than the real value of Ca required.

While the quantitative differences for predicted non-wetting fluid mobilization from a stratified porous medium using a stratified versus averaged model are specific to the properties of individual strata, we always predict regions of overpredicted mobilization by the averaged model for $\mathrm{Ca} < \mathrm{Ca}_c^*$ and $\mathrm{Ca} > \overline{\mathrm{Ca}}^*$ and underpredicted mobilization in between, when $\overline{\mathrm{Ca}}^* > \mathrm{Ca} > \mathrm{Ca}_c^*$. By exploring structural relationships between strata, such as the width ratio, W_c/W_f, the grain size ratio, a_c/a_f, and the dimensionless length of the porous medium, ℓ/W, we establish differences between averaged and stratified model predictions of S_{OR} that can be applied to stratified media with a wide range of properties.

To generalize our results over a wider parameter space, we identify three dimensionless structural parameters to describe a stratified porous medium with one coarse and one fine stratum: the grain size ratio, a_c/a_f, the stratum width ratio, W_c/W_f, and the dimensionless length of the porous medium, ℓ/W. Keeping all other descriptors of the porous medium constant using the values listed in Table 3.1, we isolate the impact of varying these key structural parameters and compare them to predictions made by averaging the structural properties of each stratum.

Physical Parameter	Variable	Value	Units
Cross-Sectional Area	A	9×10^{-6}	m^2
Wetting Fluid Viscosity	μ_w	2.7×10^{-3}	Pa·s
Non-Wetting Fluid Viscosity	μ_{nw}	16.8×10^{-3}	Pa·s
Interfacial Tension	γ	13×10^{-3}	N/m
Contact Angle	θ	0	°
Fine Stratum Cross-Sectional Area	A_f	4.5×10^{-6}	m^2
Coarse Stratum Cross-Sectional Area	A_c	4.5×10^{-6}	m^2
Tortuosity	τ	2.5	
grain Radius of Fine Stratum	r_f	20×10^{-6}	m
grain Radius of Coarse Stratum	r_c	165×10^{-6}	m
Porosity	φ	0.34	
Length of Medium	ℓ	6×10^{-4}	m
Flowrate	Q	$2.8 \times (10^{-11}$ to $10^{-2})$	m^3/s

Table 3.1: Characteristics of an example stratified porous medium. The values given in this table come from previous experimental work in a 3D model porous medium[168] and are used for the theoretical predictions made in this work.

Varying the Grain Size Ratio Between Strata. First, we observe the impact of changing the average grain size ratio between strata. The grain size ratio between strata is a particularly important parameter because high permeability strata in shales are frequently in contact with low permeability strata with grain size ratios $a_c/a_f \geq 10$[160]. We keep a_c constant and vary

a_f, so Ca_c^* remains constant. For all a_c/a_f values explored in this study, we observe the three distinct regimes observed in the base case: overprediction of mobilization by the averaged model for imposed $\mathrm{Ca} < \mathrm{Ca}_c^*$, subsequent underprediction for $\mathrm{Ca}_c^* < \mathrm{Ca} < \overline{\mathrm{Ca}}^*$, followed by another region of overprediction when $\overline{\mathrm{Ca}}^* < \mathrm{Ca} < \mathrm{Ca}_f^*$.

We first look at a grain size ratio $a_c/a_f = 2$ (Fig. 3.2a). Initially, we note that the predicted S_{OR} using an averaged model overpredicts by a factor of 2 when compared to the stratified model while the difference in Ca required for complete mobilization predicted the averaged model is only 2 times lower than the required to Ca for complete mobilization in the fine stratum. Furthermore, the underpredicted region spans a very small Ca range, from 9.7×10^{-3} to 1.5×10^{-2}. Meanwhile, when we increase a_c/a_f to 10, we observe much more striking differences in predictions from each model (Fig. 3.2b). Here, the initial S_{OR} predictions differ by a factor of 7, while the difference in Ca predicted for complete mobilization using the averaged model is 10 times lower than what the stratified model predicts. We also see a large increase in the imposed Ca range over which the averaged model underpredicts mobilization, from 8.8×10^{-3} to 2.8×10^{-2}. Comparing the plots of S_{OR} for $a_c/a_f = 2$ and $a_c/a_f = 10$ reveals an important trend. As a_c/a_f increases, the imposed Ca range over which mobilization is underpredicted increases. However, because we hold a_c constant, smaller and smaller a_f require that more non-wetting fluid be housed in the coarse stratum. As a result, for very high a_c/a_f, when the imposed $\mathrm{Ca} > \mathrm{Ca}_c^*$, the majority of residual non-wetting fluid is removed.

We clearly observe this predicted difference in non-wetting fluid removal in the state diagram of grain size ratio a_c/a_f versus imposed Ca (Fig. 3.2c), which shows the difference between S_{OR} predicted *via* an averaged versus stratified model, $\Delta S_{OR} = \overline{S}_{OR} - S_{OR,total}$. When ΔS_{OR} is negative, $\overline{S}_{OR}$ overpredicts mobilization, while a positive ΔS_{OR} indicates that $\overline{S}_{OR}$ un-

derpredicts mobilization. We see that the largest discrepancy in predictions, or the largest $|\Delta S_{OR}|$, occurs when the imposed $\mathrm{Ca} < \mathrm{Ca}_c^*$. The magnitude of this difference is indicated by the deeper saturation in the purple region observed on the left half of the plot, which suggests that an imposed $\mathrm{Ca} > \mathrm{Ca}_c^*$ would provide the largest improvement in mobilization. Furthermore, even though the width of this overpredicted region increases as a_c/a_f increases, its magnitude always remains quite low ($< 1 \times 10^{-4}$), as indicated by the weaker saturation in the gray region when compared to the magnitude of overprediction below Ca_c^*. The state diagram also illustrates that the order of magnitude of ΔS_{OR} in the final region of overprediction, $\overline{\mathrm{Ca}}^* < \mathrm{Ca} < \mathrm{Ca}_f^*$, is much lower than that of either preceding region, as indicated by the lack of saturation by either color ($|\Delta S_{OR}| < 10^{-5}$).

Taken together, this state diagram reveals that for $a_c/a_f \sim \mathcal{O}(1)$, the imposed Ca should be $\geq \mathrm{Ca}_f^*$, because comparable quantities of non-wetting fluid will be present in both strata. However, for $a_c/a_f \gg 1$, significant mobilization occurs as long as the imposed $\mathrm{Ca} > \mathrm{Ca}_c^*$, because diminishing quantities of non-wetting fluid are present in the fine stratum as a_c/a_f increases. Even though the underpredicted mobilization region exhibits an expanded Ca range, the total additional amount of non-wetting fluid mobilized by operating at $\mathrm{Ca} > \overline{\mathrm{Ca}}^*$ is small when compared to the amount mobilized by operating above Ca_c^*.

Varying the Width Ratio of Strata. Next, we investigate the impact of changing the stratum width ratio. In our predictions, we assume that the cross-sectional area, A, and the height, H, of the overall porous medium remain constant so we can vary the width, W, of each stratified layer, and therefore the cross-sectional area of each stratified layer. While ratios of cross-sectional area, A_c/A_f, between adjacent strata in gas reservoirs exhibit a wide range, from 0.05 to 20[175], we investigate a similar width ratio range, W_c/W_f from 0.01 to 10 at a

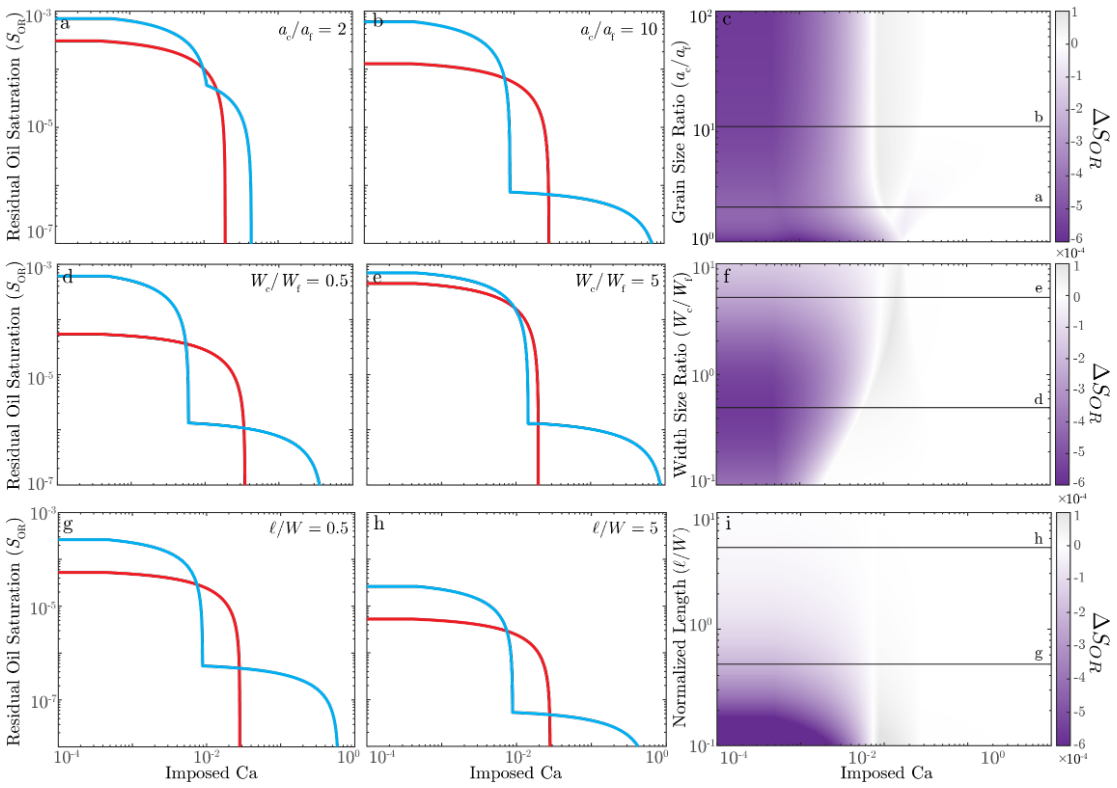


Figure 3.2: Influence of key structural parameters on S_{OR} in a stratified porous medium. (a-c) Grain size ratio. Plot of S_{OR} using a stratified model (blue) versus an averaged model (red) for (a) $a_c/a_f = 2$ and (b) $a_c/a_f = 10$. (c) State diagram of ΔS_{OR} for a wide range of grain size ratios, where $\Delta S_{OR} = \overline{S}_{OR} - S_{OR,total}$ shows regions where the averaged model overpredicts mobilization (purple) and underpredicts mobilization (gray). Black lines indicated a_c/a_f for (a) and (b), respectively. (d-f) Stratum width ratio. Plot of S_{OR} using a stratified model versus an averaged model for (d) $W_c/W_f = 0.5$ and (e) $W_c/W_f = 5$. (f) State diagram of ΔS_{OR} for a wide range of stratum width ratios shows regions of overprediction and underprediction. Black lines indicate W_c/W_f for (d) and (e). (g-i) Normalized porous medium length. Plot of S_{OR} using a stratified model versus an averaged model for (g) $\ell/W = 0.5$ and (h) $\ell/W = 5$. (i) State diagram of ΔS_{OR} for a wide range of normalized porous medium lengths shows regions of overprediction and underprediction. Black lines indicate ℓ/W for (g) and (h).

constant grain size ratio $a_c/a_f = 8$. For strata with varying $a_c/a_f \gg 1$ at a constant W_c/W_f, the amount of residual non-wetting fluid in the fine stratum becomes increasingly negligible as a_c/a_f increases, an important consideration as we observe the differences in predicted non-wetting fluid mobilization for varying W_c/W_f.

At a stratum width ratio $W_c/W_f = 0.5$, we first observe a ten-fold overprediction in non-wetting fluid mobilization by the averaged model for $\mathrm{Ca} < \mathrm{Ca}_c^*$, which also propagates the same order of magnitude of underprediction for $\mathrm{Ca}_c^* < \mathrm{Ca} < \overline{\mathrm{Ca}}^*$ and further overprediction into the regime where $\overline{\mathrm{Ca}}^* < \mathrm{Ca} < \mathrm{Ca}_f^*$ (Fig. 3.2d). This ten-fold discrepancy in the predicted imposed Ca is important because the predicted $\overline{\mathrm{Ca}}^*$ is 10 times larger than the imposed Ca necessary to mobilize all non-wetting fluid from the coarse stratum, but is 10 times smaller than the imposed Ca necessary to mobilize all non-wetting fluid in the fine stratum. Critically, this finding suggests that using the averaged model would yield greater mobilization than expected, but would unnecessarily employ Ca values an order of magnitude larger than what would be needed to completely clear the coarse stratum. Furthermore, the remaining non-wetting fluid in the fine stratum would never be recovered. While the amount of non-wetting fluid in the fine stratum would only constitute change in residual oil saturation of $\sim 10^{-6}$, this non-wetting fluid would remain unaccounted for in the porous medium.

When the stratum width ratio increases to $W_c/W_f = 5$, we observe a striking difference in the disagreement between the averaged and stratified models (Fig. 3.2e). Specifically, because $W_c \gg W_f$, the averaged model begins to return results that are increasingly skewed toward the properties of the coarse stratum. Thus, while the averaged model predicts mobilization that is fairly consistent with the stratified model in the coarse stratum, it creates a

large discrepancy between predictions from the averaged model versus the stratified model in the fine stratum. Here, the coarse stratum comprises approximately 80% of the medium, so $\mathrm{Ca}_c^* \approx \overline{\mathrm{Ca}}^*$, and the amount of non-wetting fluid mobilized from the coarse stratum using the averaged model becomes roughly equal to that mobilized using the stratified model without imposing excessively high values of Ca. However, because the averaged model almost solely encapsulates coarse stratum mobilization, $\overline{\mathrm{Ca}}^*$ underpredicts Ca_f^* by a factor of approximately 40, meaning that almost no mobilization will occur in the fine stratum.

Once again, we can generalize these observations over a wide range of W_c/W_f, as shown by the state diagram in Fig. 3.2f. While the largest magnitude in ΔS_{OR} between the averaged and stratified models occurs for imposed $\mathrm{Ca} < \mathrm{Ca}_c^*$, as evidenced by the saturation of the purple region, we also see that as W_c/W_f increases, the saturation in the underpredicted region decreases, consistent with what we see when $\mathrm{Ca} < \mathrm{Ca}_c^*$ in Figs. 3.2d and 3.2e. We also see that the overpredicted mobilization region tapers in width but increases in saturation as W_c/W_f increases. When $W_c/W_f < 1$, $\mathrm{Ca}_c^* \ll \overline{\mathrm{Ca}}^*$, and thus any enhanced mobilization that occurs in the stratified medium when the imposed $\mathrm{Ca} = \overline{\mathrm{Ca}}^*$ comes from the fine stratum, which does not constitute a significant amount of non-wetting fluid. However, as W_c/W_f increases to values greater than 1, S_{OR} predicted from the averaged model begins to approach that of the coarse stratum. As long as $W_f \neq 0$, $\overline{\mathrm{Ca}}^*$ will always be slightly larger than Ca_c^*, so any enhanced mobilization from the fine stratum that occurs as a result is condensed over a smaller Ca range, as evidenced by the saturation of the gray region at high W_c/W_f. Finally, as in the state diagram of ΔS_{OR} for varying a_c/a_f, we see that any overprediction in mobilization by $\overline{\mathrm{Ca}}^*$ that does not account for additional non-wetting fluid still present in the fine stratum is over an order of magnitude lower than overprediction when $\mathrm{Ca} < \mathrm{Ca}_c^*$.

Varying Porous Medium Length. The final structural parameter we investigate in this chapter is porous medium's length, which we non-dimensionalize using the width of the porous medium, W. The normalized lengths of oil reservoirs often exceed ℓ/W values of over 100[176]. Here, we explore two decades of dimensionless length, from 0.1 to 10, keeping the overall width of the porous medium, W, constant. The structural parameter ℓ/W does not vary with the properties of individual strata, so its impact on the magnitude of differences in averaged versus stratified predictions of non-wetting fluid mobilization is solely based on the difference in the starting predicted S_{OR} values. Importantly, changing ℓ/W while keeping W constant does not impact V_{nw} (Eq. 3.13), because $V_{nw} \neq f(\ell)$. The ratio of ℓ/W only changes S_{OR} (Eq. 3.15) because $S_{OR} = f(\ell)$. As a result, we expect that all predicted S_{OR} values will vary only in magnitude from one another, but Ca_c^*, $\overline{\mathrm{Ca}}^*$, and Ca_f^* will all remain the same for constant a_c/a_f and W_c/W_f.

Indeed, when we plot S_{OR} versus imposed Ca for $l/W = 0.5$ (Fig. 3.2g) and $l/W = 5$ (Fig. 3.2h), we verify our hypothesis. The only difference we detect as ℓ/W increases is in the amount of non-wetting fluid trapped in the porous medium, rather than changes in the sizes of overpredicted and underpredicted regions or in the magnitude of ΔS_{OR}. Simply, we see that $S_{OR} \propto 1/\ell$. This finding is also illustrated in the state diagram of ΔS_{OR} as a function of ℓ/W and imposed Ca (Fig. 3.2i). We see that the widths of the overpredicted and underpredicted regions remain constant. Only the magnitude of ΔS_{OR} changes as ℓ/W increases. Since $S_{OR} \propto 1/\ell$, we see larger S_{OR} values when $\ell \ll 1$, as reflected by the saturation in both the overpredicted and underpredicted regions at the bottom of Fig. 3.2i. However, as ℓ increases, the overall magnitude of S_{OR} becomes increasingly small, so the resultant ΔS_{OR} becomes smaller.

3.5 Conclusions

Frequently, predictions of trapped non-wetting fluid mobilization in a stratified porous medium are made by treating the medium as non-stratified and homogeneous simply by averaging the structural properties of each stratum. While this method can sometimes be used to obtain order-of-magnitude estimates for mobilization, the success of this method is highly dependent on the differences between strata. Specifically, we find that when distinct strata occupy comparable amounts of space in a porous medium and have significantly different structural properties, this method of averaging properties falls short in its ability to predict both the magnitude of non-wetting fluid mobilization in a stratified porous medium and the imposed Capillary number necessary to mobilize all non-wetting fluid from the porous medium.

In this chapter, we demonstrated a simple method to quantify how flow is split between stratified layers in a porous medium based on their structural properties and derived an expression to describe the threshold lengths of trapped non-wetting fluid ganglia in each stratum, L_{max}, as the imposed Ca in the medium increases. We then developed expressions to quantify the total residual oil saturation in a stratified porous medium, S_{OR}, using our calculated L_{max} values and compared S_{OR} calculated using the structural properties of a stratified medium to that calculated by considering a homogeneous medium whose properties are a weighted average of the two strata. Importantly, we revealed that mobilization in the coarse stratum is always initially overpredicted by the averaged model, and mobilization of non-wetting fluid from the entire medium is often overpredicted to occur at Ca more 10 times lower than what is truly required for the stratified medium.

This chapter highlights how stratification fundamentally alters the mobilization of non-wetting fluid in a porous medium. It represents a key step toward capturing the physics that underly these complex mobilization processes. It is also important to note that residual trapping and mobilization of a non-wetting fluid are history dependent, so the quantitative details of our calculations rely strongly on the structural parameters chosen in this study. However, we anticipate that our qualitative observations can still help guide mobilization processes where an injected wetting fluid is used to displace non-wetting fluid from heterogeneous subsurface media. Prominent examples include pump-and-treat remediation techniques[157,177] and enhanced oil recovery[157,158,160,178,179]. Future work in this area may explore different initial conditions, such as the non-wetting fluid being present in only one stratum, or non-uniform invasion into each stratum. Another extension of this work could combine the theory presented here with heterogeneous imbibition dynamics[168] to establish mobilization with more complex initial non-wetting fluid saturations.

Science, my boy, is made up of mistakes,

but they are mistakes which it is useful to make,

because they lead little by little to the truth.

Jules Verne, Journey to the Center of the Earth

4

Visualizing capillarity-driven colloidal adsorption

Now that we have explored colloidal transport and immiscible fluid trapping in Chapters 2 and 3, we endeavor to gain a deeper understanding of the impacts of the cou-

pling between these two processes. In Chapter 2, we injected colloidal particles into a porous medium containing previously trapped immiscible fluid, providing a good approximation of processes such as groundwater remediation and enhanced oil recovery. We visualized for the first time how colloids impact the distribution of trapped immiscible fluids in a 3D porous medium, presenting an important first step to understanding how immiscible fluid flow and colloidal deposition impact one another. However, in these experiments, we did not observe the dynamics of interactions between the *traveling* droplets and deposited particles due to the temporal resolution of our experimental setup.

To understand the impacts of deposited colloids on immiscible fluid flow processes, previous experimental and simulation works have explored single and dilute particle interactions with a traveling immiscible fluid [180–183]. While these studies provide crucial physical information about interactions between colloidal particles and immiscible fluids, they do not consider new complexities that arise in the presence of dense, multilayer deposition that exists in real geological media. In fact, few studies exist that demonstrate how dense, multilayer colloidal deposition may alter immiscible fluid flow, which is of critical importance for understanding processes such as groundwater contamination, oil migration and recovery, gas venting from sediments, CO_2 sequestration, soil drying, and fluid transport in porous membranes [184–200].

To address this gap in knowledge, in this chapter, we present preliminary data that show how an immiscible fluid droplet interacts with densely deposited, non-surface active colloidal

This chapter has been adapted from unpublished work by Joanna Schneider and Sujit S. Datta. **Author Contributions:** J.S. and S.S.D. designed the experiments; J.S. performed all experiments; J.S. and S.S.D. analyzed the data. S.S.D. designed and supervised the overall project. J.S. and S.S.D. discussed the results and wrote the preliminary manuscript.

particles at the pore scale. As defined in Chapter 2, surface activity means that colloidal particles spontaneously attach and stick to immiscible fluid interfaces under quiescent conditions. Specifically, by using cylindrical channels to approximate single pores within a porous medium, we show that immiscible fluid droplets have the propensity to both pick up non-surface active colloidal particles from solid surfaces and drop them off when they reach some finite "carrying capacity." We hypothesize that the primary mechanism of colloidal adsorption to fluid interfaces in the absence of surface activity occurs when capillary forces holding particles at the fluid interface exceed attachment forces of colloidal particles to each other and to the walls of the capillary tube upon which they are deposited. We thus call this ability of colloidal particles to localize at immiscible fluid interfaces due to flow "capillarity-induced surface activity." Finally, we show that this phenomenon can result in strong adsorption of colloidal particles to immiscible fluid interfaces, which may alter their rheology and trigger the onset of qualitatively more solid-like than fluid-like behavior.

4.1 Materials and Methods

We perform flow experiments in cylindrical quartz capillary tubes with an inner diameter $d = 1\,\text{mm}$. To ensure clean, negatively charged, hydrophilic surfaces, we place capillary tubes in a piranha solution comprised of 80% sulfuric acid (H_2SO_4) and 20% hydrogen peroxide (H_2O_2) at 75 °C for approximately one hour. In experiments with pre-deposited particles, we create a thick layer of densely deposited particles on the inner walls of a capillary tube by injecting a concentrated suspension (0.5 vol% or 2.5 vol%) of fluorescent amine-terminated

polystyrene (PS-NH_2) colloids in water with a diameter $d_p = 1$ μm (*Sigma Aldrich*). These colloidal particles are positively charged, encouraging them to stick to the cleaned quartz capillary tube walls. The injected volume of the colloidal suspension corresponds to the capillary tube volume, or pore volume, PV $= \frac{\pi}{4} d^2 \ell$, where ℓ is the length of the capillary tube. Here, ℓ ranges from 9–15 mm and the resultant injected volume of PS-NH_2 colloids ranges from approximately 7–13 μL. We then seal both ends of the capillary tube to prevent evaporation and drying effects and place the colloidal suspension-filled capillary on a rotary mixer to gently agitate the suspension for 18–24 h. PS-NH_2 colloids with $d_p = 1$ μm have a settling speed $v \approx 0.01$ mm/h in water, so this step helps to prevent biased deposition and settling of the particles in the capillary tube.

Next, we gently push excess, un-deposited particles out of the capillaries using air before injecting an aqueous wetting fluid comprised of 40% glycerol, 53.8% dimethyl sulfoxide (DMSO), and 7.2% deionized water. This fluid has the same refractive index as the non-aqueous (non-wetting) fluid employed in our experiments, which results in clear imaging of the immiscible fluid-fluid interfaces using confocal microscopy. The wetting fluid has an approximate density, $\rho_w = 1.16$ g/mL, the weighted average of its components, and a viscosity $\mu_w = 18.4$ mPa·s, measured using a cone-plate rheometer. It is also fluorescently dyed with 1 ppm Rhodamine Red (*Thermo Fisher Scientific*), and optically dyed with 1 mg/mL blue food coloring to improve optical contrast with the non-wetting fluid. The wetting fluid displaces air in the capillary and likely removes some previously adsorbed PS-NH_2 colloids due to the presence of a moving air-water interface. We continue to inject the wetting fluid at a flowrate $Q = 0.5$ mL/h for 3–4 h using a *Harvard Apparatus* Pump 11 Elite to further remove any unadsorbed colloidal particles from the capillary. The mean pore volume (PV) of a capillary

tube $\overline{\text{PV}} \approx 10$ µL, which corresponds to ≈ 150–200 PVs of wetting fluid injection prior to introduction of a non-wetting fluid droplet.

Finally, we inject a single non-wetting droplet comprised of a mixture of aliphatic and aromatic hydrocarbons (*Cargille* refractive index liquids) into the tubing upstream of the capillary tube. This fluid has a density $\rho_{nw} = 0.8$ g/mL and a viscosity $\mu_{nw} = 16.8$ mPa·s, as defined in previous work[105]. The droplet has a minimum length, $\ell_{d,min} = d$ to ensure that the droplet does not stick to the walls of the upstream tubing or capillary tube and can thus be advected through the channel. Droplet lengths ℓ_d vary from ≈ 1.5–2.5 mm and the interfacial tension between the wetting and non-wetting liquids is $\gamma \approx 13$ mN/m[105]. The droplet travels through the capillary tube at a controlled flowrate $Q = 50$ µL/h. Thus, we can define a Capillary number, which describes the ratio of viscous to capillary stresses, $\text{Ca} \equiv \mu u/\gamma$, at both the leading and trailing oil interfaces. Here, μ describes the impinging fluid's dynamic shear viscosity, u is the fluid velocity Q/A, where A is the cross-sectional area of the capillary tube, and γ is the interfacial tension between the two fluids. At the leading non-wetting interface, or receding wetting interface, $\text{Ca}_r = 2.3 \times 10^{-5}$, because the impinging fluid is the oil droplet. At the trailing non-wetting interface, or advancing wetting interface, $\text{Ca}_a = 2.5 \times 10^{-5}$ because the impinging fluid is the wetting fluid. Because the fluids are approximately viscosity matched, Ca at both interfaces is approximately equal and capillary forces dominate in describing the fluid flow.

We observe the interactions between deposited colloidal particles and a flowing immiscible fluid droplet using a *Nikon* A1R+ confocal fluorescence microscope to perform multiplexed imaging of the pore space (Fig. 4.1a). We visualize both the fluorescently dyed wetting fluid, which has primary excitation and emission wavelengths of 570 and 590 nm, respectively,

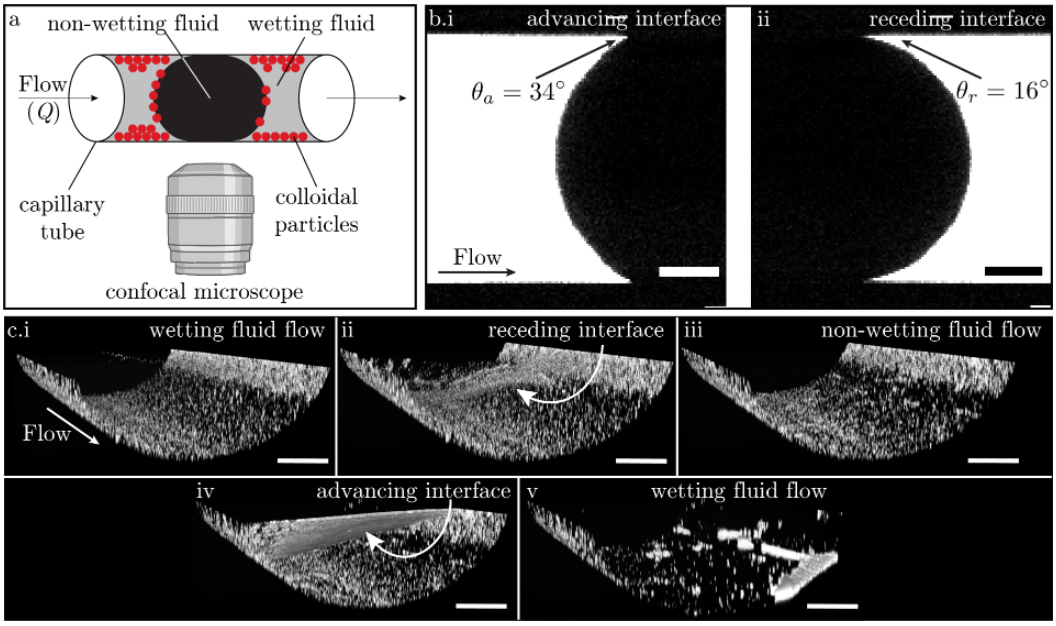


Figure 4.1: Flowing immiscible fluids adsorb deposited colloidal particles to their interfaces, changing both interfacial properties and deposition characteristics. (a) Schematic of experimental setup. Colloidal particles (red) are deposited in quartz capillary tubes before flowing a wetting fluid (gray) at a flowrate, Q. An oil droplet (black) flows through the capillary tube followed by more wetting fluid at the same flowrate. We image the flow of the oil droplet using confocal microscopy. (b) Two-dimensional (2D) images of advancing (i) and receding (ii) immiscible fluid interfaces traveling through a pristine cylindrical channel. The contact angle of the advancing interface, θ_a, remains constant as it flows through the channel at a value $\theta_a = 34 \pm 2°$ while the contact angle at the receding interface, $\theta_r = 16 \pm 2°$. Scale bars in (b) are 250 μm. (c) Three-dimensional (3D) projections of immiscible fluid flow through a cylindrical channel containing deposited colloidal particles. (i) As the wetting fluid (void space) flows through the channel containing deposited particles (white), particles remain attached to capillary walls. (ii) The receding interface enters, made visible by the colloidal particles adsorbed to it. (iii) The non-wetting fluid (void space) flows through the channel, revealing slight changes in the deposition profile from the receding interface. No changes occur during bulk non-wetting fluid flow. (iv) The advancing interface enters, made visible by colloidal particles completely saturating its surface. Curvature of the advancing interface is altered significantly from the pristine case. (v) Finally, bulk wetting fluid flow does not alter deposition. However, flow of the advancing interface has altered the deposited colloid configuration by both eroding and redepositing particles. Scale bars in (c) are 200 μm.

and fluorescein-labeled colloidal particles, which have primary excitation and emission wavelengths of 498 and 517 nm, respectively. We obtain images at several locations in the *xy* plane that are 1,272 μm × 1,272 μm in size and image a region 400 μm in depth at each *xy* location. To reconstruct flow of an immiscible fluid droplet through the capillary tube, we obtain images in 20 μm increments with an optical thickness of 16.6 μm from the bottom to the middle of the capillary tube. Together, each *z*-stack image presents a reconstruction of the bottom half of a colloidal particle-coated capillary tube. Imaging further into the capillary causes shadowing that arises from light scattering in other *z*-planes that arises from dense deposition. Continuous imaging at a single *xy*-location produces a *z*-stack in ≈ 20 s. Thus, traveling at 50 μL/h, an individual fluid-fluid interface traverses the field of view in ≈ 70 s, so each *z*-stack represents a quasi-static image of the immiscible fluid droplet.

4.2 Interactions between deposited particles and immiscible fluids

We first inject a non-wetting fluid droplet into a pristine, cylindrical quartz capillary tube containing no previously deposited colloidal particles. As the non-wetting fluid droplet travels through the capillary tube, we image both the receding and advancing wetting fluid interfaces (Movies S1 & S2). The receding interface is defined as the downstream oil droplet interface, while the advancing interface is the upstream oil droplet interface. Throughout their time in the imaging window, we observe that both the advancing (Fig. 4.1b.i) and receding (Fig. 4.1b.ii) interfaces maintain a constant shape, which can be quantified by their contact angles, θ, with the walls of the capillary. We expect each interface to have a constant contact angle

because the capillary number at both interfaces, $Ca_a \approx Ca_r << 1$. Measuring the contact angle in a two-dimensional (2D) image close to the center of the capillary ($z \approx 400$ μm) at three separate time points, we obtain values for the advancing and receding contact angles of $\theta_a = 16 \pm 2^\circ$ and $\theta_r = 34 \pm 2^\circ$, respectively. While the distinct values of θ_a and θ_r remain constant over time, we note that $\theta_a \neq \theta_r$, which may be a result of imperfect viscosity-matching in which μ_w is slightly greater than μ_{nw}. We also observe that the oil droplet does not break up or produce any non-wetting films as it flows along the length of the capillary tube.

Having characterized the flow of an oil droplet in a pristine channel, we ask: how does the presence of deposited colloidal particles alter immiscible fluid flow? To answer this question, we deposit colloidal PS-NH_2 ($d_p = 1$ μm) by injecting a 0.5 vol% suspension of particles (see Materials & Methods) before removing any excess, unadsorbed particles by flowing many pore volumes of a wetting fluid through the channel. After injection of approximately 200 PVs of wetting fluid, only deposited particles remain (Fig. 4.1c.i, Movie S3) and no additional particles are suspended in the wetting fluid. However, as the receding interface travels through the capillary, we make a surprising observation. Here, we see that colloidal particles are adsorbed to the receding interface, as evidenced by the image of the capillary tube shown in Fig. 4.1c.ii and Movie S3. Despite the fact that this image only shows fluorescence from colloidal particles, we see the shape of the receding interface due to the presence of adsorbed particles. Qualitatively, we observe that the shape of the receding interface appears consistent with that of a pristine interface. We also note that despite significant surface coverage, the receding interface is not completely saturated, or jammed, with particles. Further analysis is required to compare the radius of curvature of the particle-laden interface with a pristine interface and quantify its total surface coverage.

As the bulk of the non-wetting fluid droplet enters the imaging window, we make two additional observations (Fig. 4.1c.iii, Movie S3). First, we note that the receding interface erodes and redeposits particles from the capillary walls. Because the receding interface is not fully saturated, we expect erosion to dominate as the interface continually removes deposited particles from the capillary walls. Indeed, by quantifying the overall intensity difference between Fig. 4.1c.i and Fig. 4.1c.iii, we measure a decrease in overall deposition of about 9%, consistent with the hypothesis that the receding interface will continue to erode colloidal particles from capillary walls until it is completely saturated. Similar to Fig. 4.1c.i, we also note that as the non-wetting fluid flows through the capillary, no particles are mobilized into the bulk non-wetting fluid. The lack of particles in the bulk fluid indicates that the presence of an interface is required to mobilize deposited particles into the channel.

Next, the advancing interface travels through the field of view, as shown in Fig. 4.1c.iv and Movie S3, exhibiting stark differences from the pristine advancing interface shown in Fig. 4.1b.i. We first observe that the advancing interface appears to be completely coated with colloidal particles, as evidenced by the completely opaque sheet in the middle of the 3D projection reconstructed in Fig. 4.1c.iv. This observation that advancing fluid interfaces exhibit stronger removal of colloidal particles from solid surfaces than receding interfaces has also been shown for air-water interfaces[201,202]. Surprisingly, we also observe that the shape of the interface appears completely different to that pictured in Fig. 4.1b.i. Instead of exhibiting a hemisphere-like shape with some curvature, the advancing interface appears to lack any curvature and is almost flat. We hypothesize that this stark contrast in the shape of the advancing interface may be a result of dense colloidal adsorption that may trigger a fluid-like to solid-like transition in the interfacial rheology.

Finally, Fig. 4.1c.v shows the resulting deposition pattern following the flow of a fluid interface densely saturated with colloidal particles. Here, we see a drastic difference in the deposition profile compared to that produced by the receding interface (Fig. 4.1c.iii). Despite being almost completely coated in colloidal particles, the advancing interface continues to erode particles from capillary walls. However, redeposition of large aggregates onto the capillary walls when the fluid interface is completely saturated is also indicative of another important trait of these interfaces: once they become saturated with colloidal particles, immiscible fluid interfaces begin to shed adsorbed particles, indicating that they have a finite "carrying capacity." Prior to reaching this carrying capacity, redeposition of colloidal particles on solid surfaces is minimal. However, as interfaces reach this carrying capacity, they begin to redeposit large aggregates. Despite this redeposition event, quantification of the particle fluorescence along the walls of the capillary tube shows that the advancing interface's passage results in a net decrease in overall deposition of about 53%, indicating that the advancing interface adsorbs more particles than the receding interface, and adsorbs more particles than it sheds.

4.3 Mechanism of adsorption to immiscible fluid interfaces

In Fig. 4.1, we observe that colloidal particles adsorb to both advancing and receding immiscible fluid interfaces. Often, the key physical phenomenon that drives colloidal particles to immiscible fluid interfaces is surface activity, which causes particles to preferentially localize at these interfaces due to their surface chemistry. In particular, homogeneous par-

ticles exhibit strong surface activity when they exhibit intermediate wettability, or are neither strongly hydrophilic or hydrophobic[203]. However, previous work shows that amine-terminated polystyrene is only weakly surface active at or near neutral pH[204] and does not produce a significant decrease in interfacial tension at oil-water interfaces. Furthermore, data presented in Chapter 2 provide additional evidence that amine-terminated polystyrene colloids are not surface active in our index-matched fluids[3]. We plan to collect additional data to support the claim that amine-terminated polystyrene is not surface active in our wetting and non-wetting fluids in two ways. First, we plan to measure the interfacial tension between the wetting and non-wetting fluids *via* pendant drop tensiometry with varying concentrations of amine-terminated polystyrene nanoparticles. Next, we will also test the ability of amine-terminated polystyrene nanoparticles to stabilize emulsions of our wetting and non-wetting fluids. We hypothesize that interfacial tension will not vary significantly upon the addition of PS-NH_2 colloids and therefore will not stabilize emulsions over long periods of time, supporting our hypothesis that PS-NH_2 colloids are indeed not quiescently surface active.

Another possible mechanism for adsorption of colloidal particles to a fluid-fluid interface is the emergence of capillary forces that act on deposited particles due to the presence of a moving contact line[182]. In addition to overcoming the adhesive, friction, and hydrodynamic drag forces required to remove deposited particles from the walls, we hypothesize that capillary forces must also overcome some energetic barrier to adsorption in order to adsorb PS-NH_2 colloidal particles, which are not quiescently surface active. Previous works show that electrostatic repulsion of particles from the fluid interface due to image charges or previously adsorbed colloidal particles may play a significant role in the development of this energy barrier[205–207]. However, previous work has measured the contact angles of polystyrene (PS) and

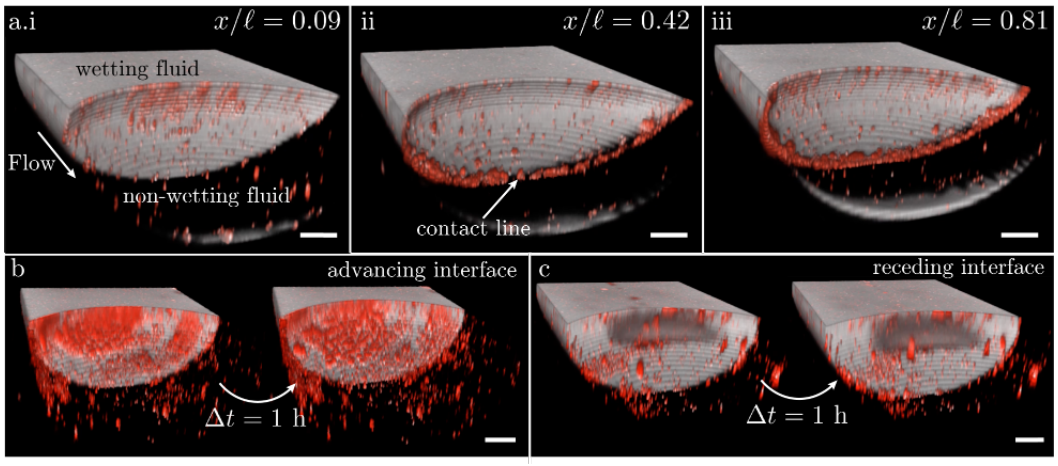


Figure 4.2: The presence of a moving three-phase contact line enables adsorption of colloidal particles to moving immiscible fluid interfaces. (a) Adsorption of deposited colloidal particles from an 8×10^{-3} vol% suspension to the advancing interface at (i) $x/\ell = 0.09$, (ii) $x/\ell = 0.42$, and (iii) $x/\ell = 0.81$ as the immiscible fluid flows show that adsorbed particles begin to aggregate at the three-phase contact line between the capillary wall and the immiscible fluid interface. Adsorption of dilute deposited colloidal particles to the (b) advancing and (c) receding interfaces without imposed flow immediately after imposed flow stops (left) and at a time $\Delta t = 1$ h later (right). Gray indicates the wetting fluid, while void space (black) indicates the non-wetting fluid. Colloidal particles are shown in red. The flow direction in all images is indicated by the white arrow and chosen to optimize visualization of particle adsorption. Scale bars in all images are 200 μm.

PS-NH_2 with water to be $\theta_{PS} = 78°$and $\theta_{PS-NH_2} = 55.5°$ [208], respectively, indicating a decrease in hydrophobicity due to the presence of amine groups. This decrease in hydrophobicity provides PS-NH_2 with intermediate wettability that may allow capillary forces to overcome an electrostatic energy barrier. Thus, we hypothesize that capillary forces that act on deposited particles drive adsorption of PS-NH_2 colloids to immiscible fluid interfaces due to the presence of a moving contact line.

To test this hypothesis, we perform the experiment shown in Fig. 4.1 again, but with one crucial change. Instead of depositing colloidal particles prior to flow and allowing them to adhere to the capillary walls for a pre- deposition time $t_p \approx 24$ h, we probe a lower concentration regime by flowing a dilute suspension (8×10^{-3} vol%) of PS-NH_2 colloidal particles immediately prior to the flow of a non-wetting fluid droplet for a suspension flow time $t_s \approx 30$ min. This difference in timescales, $\tau \equiv t_p/t_s \approx 50$, ensures minimal deposition on the capillary walls prior to the non-wetting fluid droplet flow. Because this experimental modification results in minimal pre-deposition on the capillary walls, we expect that the coverage of the immiscible fluid interface with colloidal particles will be much lower and localized to the three-phase contact line where capillary forces are largest.

Imaging three locations along the length of the capillary tube, we first observe how the interfacial coverage changes as the three-phase contact line moves. We focus on the advancing interface due to its ability to more strongly detach colloidal particles from the capillary walls. For a capillary length $\ell = 13$ mm, we first image at a position $x = 1.2$ mm, or $x/\ell = 0.09$ (Fig. 4.2a.i, Movie S4). We observe minimal deposition on the walls of the capillary tube, while most particles remain suspended in the aqueous phase. However, we do observe some adsorption to the immiscible fluid interface with some particles present at the contact line

and several large aggregates closer to the center of the capillary tube. As the immiscible fluid droplet continues to flow, we next image at a position $x/\ell = 0.42$ (Fig. 4.2a.ii, Movie S5). At this position along the capillary, we observe more adsorption to the fluid interface, indicating that movement of the contact line is necessary for interfacial adsorption. We also see that most of the adsorption occurs at the contact line, suggesting that capillary forces at the wall play a role in interfacial adsorption. Finally, at a position $x/\ell = 0.81$ (Fig. 4.2a.iii, Movie S6), we observe even more significant adsorption, most of which is localized at the contact line, providing further support that capillarity drives adsorption in these experiments. To quantify these qualitative observations, we plan to measure the total particle accumulation at the interface and analyze how the concentration varies as a function of its distance from the three-phase contact line for all three positions along the capillary.

We also perform a calculation of the settling velocity of PS-NH_2 particles in the non-wetting fluid and compare this quantity with the velocity of the immiscible fluid droplet through the capillary tube. We obtain the Stokes settling velocity by balancing hydrodynamic drag and gravitational settling as follows:

$$u_s = \frac{2(d_p/2)^2(\rho_p - \rho_f)g}{9\mu} \tag{4.1}$$

where u_s is the settling velocity, ρ_p is the particle density, ρ_f is the fluid density, and μ is the fluid viscosity. Assuming $\rho_p = 1.05$ g/cm^3, the maximum settling velocity occurs in the non-wetting fluid at a value $u_s = 0.03$ mm/h. The advection speed of the oil droplet, $u_a = Q/A$, is equal to 64 mm/h, where $Q = 50$ μL/h and $A = \pi(d/2)^2$. Thus, because $u_a/u_s \approx 2000$, we expect advection to dominate over settling and any accumulation at the contact line can be attributed to capillary forces as the contact line moves.

As a final test of our hypothesis, we repeat the experiment shown in Fig. 4.2a with one important change: once the immiscible fluid droplet enters the capillary tube, we turn off the flow. Because the contact line does not move in the absence of flow, we anticipate that no new adsorption events will occur. Indeed, at both the advancing (Fig. 4.2b, Movie S7) and receding (Fig. 4.2c, Movie S8) interfaces, we observe that particles diffuse along the fluid interface because it is not sufficiently jammed; however, the total amount of adsorbed particles when the flow is stopped at time $t = 0$ min is approximately equal to the amount of adsorbed particles at a time $\Delta t = 1$ h later. If these particles were quiescently surface active, over the course of 1 hour, we would expect approximately 1500 more particles to reach the interface, assuming a flat interface and a Stokes-Einstein diffusivity for PS-NH_2 colloids $\mathscr{D} = 2.4 \times 10^{-14}$ m^2/s. Future analysis will quantitatively measure the total fluorescence intensity at each interface over time to confirm our qualitative observations and compare the intensity evolution to what we would expect if diffusion was sufficient to overcome the energy barrier to adsorption.

As a final test of our hypothesis that capillary forces drive adsorption of PS-NH_2 colloids to immiscible fluid interfaces, we can perform a similar experiment to that shown in Fig. 4.2, instead flowing a more concentrated suspension (4×10^{-2} vol%) of PS-NH_2 colloidal particles through the channel immediately prior to the flow of a non-wetting fluid droplet. Probing this higher concentration regime allows us to evaluate the conditions required for the immiscible fluid droplet's advancing interface to become completely saturated, or jammed. We hypothesize that the flow of a more concentrated suspension will cause jamming at the immiscible fluid interface more quickly, after which point it will need to redeposit previously adsorbed particles due to its finite carrying capacity. Indeed, we observe jamming at the ad-

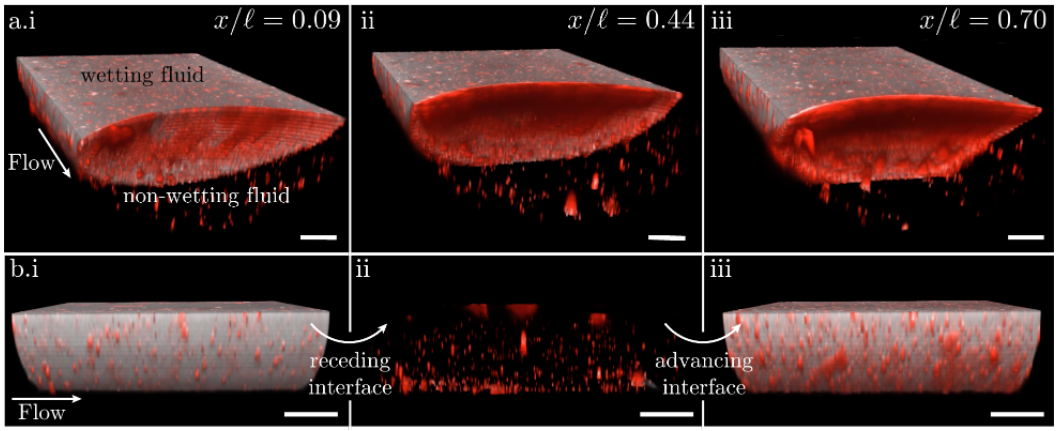


Figure 4.3: Interfaces pick up particles from solid surfaces until they reach a finite carrying capacity. (a) Adsorption of deposited colloidal particles from a 4×10^{-2} vol% suspension to the advancing interface at (i) $x/\ell = 0.09$, (ii) $x/\ell = 0.44$, and (iii) $x/\ell = 0.70$ as the immiscible fluid flows show that adsorbed particles begin to completely saturate the immiscible fluid interface, resulting in modified curvature and redeposition from the jammed interface. (b) Jamming forces interfaces to redeposit adsorbed particles in order to pick up more particles at the contact line. Side view of the deposition profile (i) before immiscible fluid flow, (ii) after the receding interface, (iii) and after the advancing interface reveals new deposition of large aggregates at $x/\ell = 0.44$. Gray indicates the wetting fluid, while void space (black) indicates the non-wetting fluid. Colloidal particles are shown in red. The flow direction in all images is indicated by the white arrow and chosen to optimize visualization. Scale bars in all images are 200 μm.

vancing interface at all three locations along the channel (Fig. 4.3a, Movies S9-S11), giving rise to two important changes in interfacial behavior. First, we observe that the advancing interface curvature more closely mimics that shown in Fig. 4.1c.iv, indicating that jamming may impact interfacial elasticity. Second, at the onset of jamming—which occurs even for small $x/\ell = 0.09$ in this experiment—particles start to get redeposited in larger quantities (Fig. 4.3b.iii) because the moving contact line continuously picks up deposited particles despite the interface's finite surface area. We show the deposition profile prior to immiscible fluid flow (Fig. 4.3b.i) and after the unsaturated receding interface passes (Fig. 4.3b.ii) for comparison. Using image analysis, we plan to quantify interfacial surface coverage with colloidal particles and measure changes in the deposition profile along the capillary walls before and after passage of the receding and advancing interfaces.

4.4 Dense deposition alters interfacial rheology

We have now established how the presence of a moving contact line enables adsorption of quiescently non-surface active particles to a fluid-fluid interface. To explore the implications of this adsorption on immiscible fluid transport, we return to our experimental setup from Fig. 4.1. In Fig. 4.1, we see that the advancing interface reaches its carrying capacity, resulting in changes to the interfacial curvature (Fig. 4.1c.iv) and subsequent redeposition (Fig. 4.1c.v). Here, we probe the impacts of even more dense predeposition of colloidal particles by injecting a 2.5 vol% suspension—five times more concentrated than that shown in Fig. 4.1—before flowing a non-wetting fluid droplet through the channel. Once again, we observe that the viscous forces due to bulk flow of both the wetting and non-wetting fluid do not result in substantial detachment of colloidal particles, while the receding interface adsorbs a small amount of colloidal particles (Movie S12). However, we hypothesize that the advancing interface will become jammed, reaching a finite carrying capacity that not only alters its radius of curvature, but drastically alters interfacial rheology.

Indeed, as the advancing interface enters the imaging window, we confirm our hypothesis that the fluid interface would become jammed in the presence of dense predeposition (Fig. 4.4a, Movie S12). However, we also note that the shape of the interface deviates significantly from that given in the pristine, particle-free case. Specifically, we observe that the fluid interface makes $\approx 90^\circ$ angle with the left wall of the capillary and curves backward to travel parallel to the right wall. For purely Newtonian fluid-fluid interfaces, we expect contact angles on both walls to be symmetrical. However, this abnormal curvature provides qualitative ev-

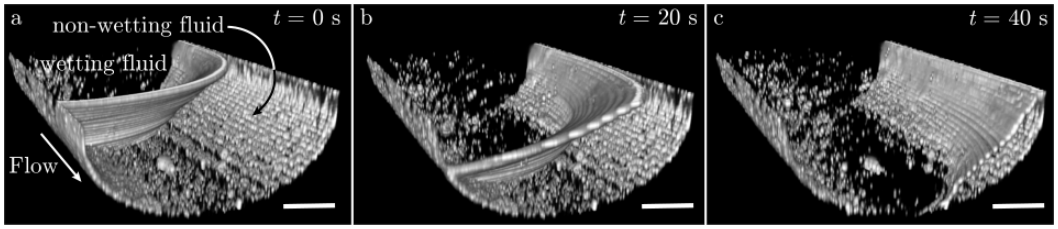


Figure 4.4: Interfaces that have reached their carrying capacity display altered interfacial rheology. Three-dimensional (3D) projections of the advancing interface as it travels through a channel with concentrated predeposition at times (a) $t = 0$ s, (b) $t = 20$ s, and (c) $t = 40$ s. Particles (white) coat the advancing interface in all three frames. The fluid upstream of the advancing interface (void space) is the wetting fluid, while the downstream fluid (void space) is the non-wetting fluid. The advancing interface enters at an angle $\approx 90^\circ$ to the left wall and curves to travel parallel to the right wall, resulting in complex curvature that could not be obtained by a Newtonian fluid-fluid interface alone. The flow direction is indicated by the white arrow. Scale bars in all images are 200 μm.

idence that colloidal jamming at the fluid interface endows it with solid-like properties. This change from fluid-like to more solid-like behavior also allows the interface to behave similarly to an elastic sheet, which we do not see for immiscible fluid interfaces. The images shown in Figs. 4.4b and 4.4c further support our observation of enhanced elasticity, revealing that as the interface travels along the left wall and bottom of the capillary, it continues to erode and redeposit colloidal particles. Meanwhile, on the right side of the channel, the interface does not make complete contact with the wall, eventually trapping at least part of the immiscible fluid droplet as a thin film between the capillary wall and the fluid interface.

4.5 Conclusions and next steps

Thus far, we have established a clear picture of the mechanism driving colloidal adsorption to immiscible fluid interfaces. As a moving contact line passes over deposited colloidal particles, we found that capillary forces drive PS-NH_2 colloids to immiscible fluid interfaces, overcom-

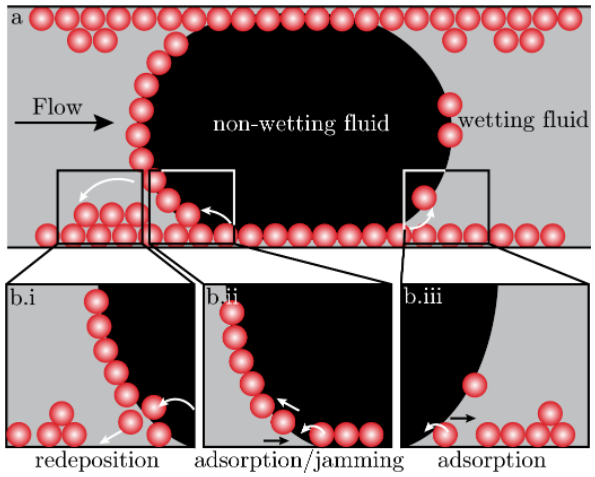


Figure 4.5: Schematic of capillarity-driven colloidal adsorption to fluid-fluid interfaces. (a) Macroscopic schematic of an oil droplet in a colloidal particle-coated capillary tube. Flow is from left to right. Call-out boxes indicate key phenomena that we hypothesize lead to the proposed observations in this chapter. White arrows show direction of particle motion and black arrows show direction of fluid motion. (b.i) Redeposition of colloidal particles onto capillary walls. After the advancing interface becomes jammed, particles continue to accumulate at the contact line. These particles get wedged between adsorbed particles, eventually forcing them off the interface and into the bulk fluid as more particles accumulate there. (b.ii) Jamming at the advancing fluid interface. Jamming occurs when the advancing interface becomes saturated with colloidal particles due to adsorption. As particles accumulate at the contact line, they push previously adsorbed particles up until the interface is completely saturated. (b.iii) Colloidal adsorption at the receding interface. Colloidal particles accumulate at the contact line, but more weakly at the receding interface than the advancing interface. We hypothesize that this phenomenon is due to stronger PS-NH_2 adsorption to capillary walls in the presence of the wetting fluid than in the non-wetting fluid.

ing particle attachment forces and the electrostatic energy barrier to their adsorption (Fig. 4.5). Consistent with previous studies, we also observed significantly higher adsorption of colloidal particles to advancing fluid interfaces, owing to stronger detachment forces than those at receding fluid interfaces[201]. In channels with significant colloidal deposition, adsorption of particles to flowing advancing fluid interfaces eventually resulted in their near complete coverage, or jamming. As these jammed advancing interfaces continued to flow and pick up colloidal particles at the moving three-phase contact line, we observed that they began to redeposit previously adsorbed particles for the first time, indicating that interfaces have a finite carrying capacity. Finally, we noted that the onset of jamming alters rheology

of immiscible fluid interfaces, providing them with elasticity that alters their flow behavior at the pore scale. The onset of more solid-like interfacial rheology likely also has important implications for immiscible fluid flow and trapping in more complex, 3D porous media. A summary of these findings is shown in Fig. 4.5.

While our preliminary results highlight several important findings, important next steps for this work will be required to quantify the qualitative observations presented in this chapter. Specifically, we will need to perform image analysis that quantifies coverage of fluid interfaces and solid surfaces with colloidal particles and measures curvature for fluid interfaces with non-uniform shapes. We also plan to perform additional experiments utilizing pendant drop tensiometry to further probe the quiescent surface activity of PS-NH_2 colloidal particles. Additional experiments could also explore the strength of the electrostatic energy barrier to adsorption by probing particle charge and charge screening effects.

4.6 Supplementary Movie Captions

The movies corresponding to data in this chapter can be found in the repository at: https://github.com/joannaclaireschneider/dissertation-movies.

Movie S1. Flow of an immiscible fluid droplet through a pristine channel. Two-dimensional (2D) slice at $z \approx 400$ μm shows the center of a non-wetting fluid droplet (black) as it travels through the channel surrounded by wetting fluid (gray). The radius of curvature at the receding and advancing interfaces remain constant as the droplet traverses the channel. Scale

bar is 200 μm and video plays at 80× faster than real time.

Movie S2. Flow of an immiscible fluid droplet through a pristine channel. Three-dimensional (3D) projection of a non-wetting fluid droplet (black) as it travels through the channel surrounded by wetting fluid (gray). The radius of curvature at the receding and advancing interfaces remain constant as the droplet traverses the channel. Scale bar is 200 μm and video plays at 80× faster than real time.

Movie S3. Flow of an immiscible fluid droplet through a channel with pre-deposited colloidal particles. Three-dimensional projection of a non-wetting fluid (black) as it travels through a channel containing pre-deposited colloidal particles (red) surrounded by wetting fluid (gray). The receding interface shows some adsorption of colloidal particles, while the advancing interface appears nearly saturated, resulting in changes in curvature and the resultant deposition profile on the capillary walls. The bottom video is identical but only shows the fluorescence from colloidal particles (white), so both wetting and non-wetting fluids are represented by void space. Scale bar is 200 μm and video plays at 80× faster than real time.

Movie S4. Flow of an immiscible fluid droplet through a channel containing an 8×10^{-3} vol% suspension of colloidal particles. Three-dimensional projection of a non-wetting fluid (black) as it travels through a channel containing a colloidal suspension (colloids shown in red, wetting fluid shown in gray) at a position $x/\ell = 0.09$ along the channel shows minimal colloidal adsorption to both the advancing and receding interfaces. Scale bar is 200 μm and video plays at 80× faster than real time.

Movie S5. Flow of an immiscible fluid droplet through a channel containing an 8×10^{-3}

vol% suspension of colloidal particles. Three-dimensional projection of a non-wetting fluid (black) as it travels through a channel containing a colloidal suspension (colloids shown in red, wetting fluid shown in gray) at a position $x/\ell = 0.42$ along the channel shows minimal colloidal adsorption to the receding interface. However, particles begin to accumulate strongly at the three-phase contact line of the advancing interface. Scale bar is 200 μm and video plays at 80× faster than real time.

Movie S6. Flow of an immiscible fluid droplet through a channel containing an 8×10^{-3} vol% suspension of colloidal particles. Three-dimensional projection of a non-wetting fluid (black) as it travels through a channel containing a colloidal suspension (colloids shown in red, wetting fluid shown in gray) at a position $x/\ell = 0.81$ along the channel shows minimal colloidal adsorption to the receding interface. However, particles continue to accumulate strongly at the three-phase contact line of the advancing interface. Scale bar is 200 μm and video plays at 80× faster than real time.

Movie S7. Time lapse of the advancing interface of a static immiscible fluid droplet surrounded by an 8×10^{-3} vol% suspension of colloidal particles. Particles are localized at the advancing interface prior to flow being stopped. Over time, particles diffuse along the interface, but the overall amount of particles adsorbed to the interface remains relatively constant. We attribute movement of the advancing interface to fluid relaxation after flow is stopped. Scale bar is 200 μm and video plays at 80× faster than real time.

Movie S8. Time lapse of the receding interface of a static immiscible fluid droplet surrounded by an 8×10^{-3} vol% suspension of colloidal particles. Particles are localized at the receding interface prior to flow being stopped. Over time, particles diffuse along the interface, but the

overall amount of particles adsorbed to the interface remains relatively constant. We attribute movement of the receding interface to fluid relaxation after flow is stopped. Scale bar is 200 μm and video plays at 80× faster than real time.

Movie S9. Flow of an immiscible fluid droplet through a channel containing an 4×10^{-2} vol% suspension of colloidal particles. Three-dimensional projection of a non-wetting fluid (black) as it travels through a channel containing a colloidal suspension (colloids shown in red, wetting fluid shown in gray) at a position $x/\ell = 0.09$ along the channel shows minimal colloidal adsorption to the receding interface, but the advancing interface is nearly saturated. Bottom video shows the same experiment at an angle that highlights changes in deposition as the receding and advancing interfaces pass through the field of view. Flow direction in this video is from left to right. Scale bar is 200 μm and video plays at 80× faster than real time.

Movie S10. Flow of an immiscible fluid droplet through a channel containing an 4×10^{-2} vol% suspension of colloidal particles. Three-dimensional projection of a non-wetting fluid (black) as it travels through a channel containing a colloidal suspension (colloids shown in red, wetting fluid shown in gray) at a position $x/\ell = 0.44$ along the channel shows minimal colloidal adsorption to the receding interface, but the advancing interface is saturated. Bottom video shows the same experiment at an angle that highlights changes in deposition as the receding and advancing interfaces pass through the field of view. Flow direction in this video is from left to right. Scale bar is 200 μm and video plays at 80× faster than real time.

Movie S11. Flow of an immiscible fluid droplet through a channel containing an 4×10^{-2} vol% suspension of colloidal particles. Three-dimensional projection of a non-wetting fluid (black) as it travels through a channel containing a colloidal suspension (colloids shown in

red, wetting fluid shown in gray) at a position $x/\ell = 0.70$ along the channel shows that the advancing interface is saturated. Bottom video shows the same experiment at an angle that highlights changes in deposition as the advancing interface passes through the field of view. Flow direction in this video is from left to right. Video taken at this position does not capture flow of the receding interface. Scale bar is 200 μm and video plays at 80× faster than real time.

Movie S12. Flow of an immiscible fluid droplet through a channel with dense pre-deposited colloidal particles. Three-dimensional projection of a non-wetting fluid (black) as it travels through a channel containing pre-deposited colloidal particles (red) surrounded by wetting fluid (gray). The receding interface shows some adsorption of colloidal particles, while the advancing interface appears completely saturated, resulting in drastic changes in curvature and the resultant deposition profile on the capillary walls. The bottom video is identical but only shows the fluorescence from colloidal particles (white), so both wetting and non-wetting fluids are represented by void space. Scale bar is 200 μm and video plays at 80× faster than real time.

You, who are on the road

must have a code that you can live by.

And so, become yourself

because the past is just a goodbye.

Crosby, Stills, Nash, & Young, Teach Your Children

5

Predicting immiscible fluid flow in erodible porous media

In Chapter 4, we used pore-scale experiments to highlight the impacts of deposited colloidal particles on traveling immiscible fluid interfaces in a porous medium. Namely, we

observed that capillary forces at a traveling three-phase contact line overcome particle attachment forces and the electrostatic energy barrier to adsorption to drive deposited, non-surface active colloidal particles to immiscible fluid interfaces. Eventually, this ability of fluid interfaces to pick up colloidal particles *via* capillary forces resulted in jamming of these particles at fluid-fluid interfaces. As they continued to flow, we observed that these interfaces began to redeposit previously adsorbed particles, indicating a finite carrying capacity. Indeed, this ability of immiscible fluid interfaces to both pick up and drop off colloidal particles has important implications not only on pore-scale phenomena, as explored in Chapter 4, but on macroscopic flow as well.

Real world porous media are often coated in layers of colloidal particles, inorganic precipitates, and organic matter[2,34,113,121,137,209–214]. However, despite their common occurrence, the influence of solid erosion & deposition on fluid drainage—and vice versa—has, to our knowledge, never been studied. Extensive research has expanded predictions of fluid drainage in a porous medium[142,215], most of which builds on the seminal model of *invasion percolation* proposed by Wilkinson and Willemsen four decades ago[216]. In this model, a porous medium is assumed to be composed of a static solid matrix of uniform wettability (with a prescribed three-phase contact angle θ) that houses an interconnected network of pores with randomly varying sizes. The immiscible, or non-wetting fluid is taken to be much more viscous than the wetting fluid, and its flow is considered to be very slow; in this limit, which characterizes

This chapter has been adapted from a pre-print by Joanna Schneider, Christopher A. Browne, Malcolm Slutzky, Cecilia A. Quirk, Daniel B. Amchin, and Sujit S. Datta. Fluid drainage in erodible porous media. *arXiv pre-print*, arXiv:2303.01260, 2023.[4] **Author Contributions:** J.S., C.A.B., and D.B.A. designed simulations; J.S., M.S., and C.A.Q. performed all simulations; J.S., C.A.B., and S.S.D. designed and performed the theoretical analysis; S.S.D. designed and supervised the overall project. All authors discussed the results. J.S. and S.S.D. wrote the manuscript.

many real-world processes, capillary forces at the immiscible fluid interface dictate the resulting displacement pathway. In particular, the non-wetting fluid cannot invade a pore of entrance radius r until the capillary pressure difference across the interface reaches a threshold $\Delta p_c \equiv 2\gamma \cos\theta / r$, where γ is the interfacial tension between the two fluids. Hence, the fluid displacement proceeds one pore at a time—with the non-wetting fluid invading the largest pore accessible to it, and therefore the lowest capillary pressure threshold, successively. The fluid displacement pathway is then determined by random local variations in pore size, resulting in a characteristic ramified and disordered displacement pattern known as *capillary fingering* (CF) [124,155,217–226].

Here, we incorporate the physics of solid erosion & redeposition into the classic framework of invasion percolation. Using numerical simulations, we reveal two new drainage behaviors whose fluid displacement and solid deposition patterns differ dramatically from standard CF: *rapid clogging*, in which redeposited material rapidly clogs the pore space and arrests subsequent flow, and *erosion-enhanced fingering*, in which constriction of some pores by deposition unexpectedly enables the non-wetting fluid to invade a greater fraction of the medium. Furthermore, we use calculations to delineate the conditions under which these different behaviors arise, governed by two dimensionless parameters that quantify how much of, and how easily, the solid matrix can be eroded. Our results thereby help expand current understanding of these rich physics, with implications for applications of drainage in industry and the environment.

To begin to unravel the complex physics underlying this problem, we examine a simple, but illustrative, example. Following the typical approach of pore-network modeling[227–229], we consider fluid drainage in a 2D network of $N \times N$ nodes, which represent the pore "bodies", with locations defined by an adjacency matrix with network connectivity c (Fig. 5.1a). The edges between nodes are indexed serially by i and represent the constrictions ("throats") between pores. Because p_c is locally maximum at these constrictions, they control both pore invasion and solid erosion. We thus focus our attention on the edges of the network; for simplicity, we assume that they compose the entirety of the pore space volume, and approximate them as cylinders of uniform length L and pristine radii $r_{i,p}$ drawn randomly from a given distribution $\rho(r_{i,p})$.

To impart erodibility to this static matrix, we consider the inner wall of each pore throat to also be coated by a layer of erodible material, initially of constant thickness t_d (Fig. 5.1b–c) distributed uniformly throughout the medium. The effective radius of throat i is then given by $r_i = r_{i,p} - t_d$, with a corresponding capillary pressure threshold $\Delta p_c(r_i) = 2\gamma \cos\theta / r_i$; without loss of generality, we take $\theta = 0$. Motivated by studies in single pores[123,180–183], we account for drainage-induced erosion using a simple rule: if a pore is invaded by the non-wetting fluid, the moving immiscible fluid interface erodes material from the wall (Fig. 5.1d) when $\Delta p_c(r_i)$ exceeds a threshold stress σ_y that quantifies the material's durability, analogous to a yield stress. For ease of notation, we indicate dimensionless quantities by overtildes ($\tilde{}$), and nondimensionalize all length scales by $r_{p,\max} \equiv \max\{r_{i,p}\}$. The ratio $\tilde{\Sigma} \equiv \Delta p_c(r_{p,\max})/\sigma_y$ then compares the smallest capillary pressure that can possibly arise in the porous medium

to the threshold erosion stress; that is, it describes the relative ease with which the immiscible fluid interface erodes material from the pore walls as it moves. We therefore call this dimensionless parameter the medium's *erodibility*.

Hence, as the non-wetting fluid invades a pore with throat radius r_i, the amount of material eroded from its walls depends on $\tilde{\Sigma}$. If $\tilde{\Sigma} < \tilde{r}_i$, erosion does not occur, and the dimensions of the pore remains unchanged after drainage; the radius after the entire drainage process has completed, $\tilde{r}'_i$, remains equal to $\tilde{r}_i$. Above the threshold $\tilde{\Sigma} \geq \tilde{r}_i$, erosion causes the radius to increase to a new value $r'_i = 2\gamma/\sigma_y$ at which the corresponding capillary pressure becomes balanced by the threshold stress for erosion, or equivalently, $\tilde{r}'_i = \tilde{\Sigma}$. However, there is a limit to how much material can be eroded from a pore: if the erodibility is so large that this new value $2\gamma/\sigma_y$ exceeds the pristine radius $r_{i,p}$ (that is, if $\tilde{\Sigma} > \tilde{r}_{i,p}$), then the pore throat radius saturates at its largest possible value, $\tilde{r}'_i = \tilde{r}_{i,p}$.

Finally, we also incorporate the subsequent deposition of the eroded material in the non-drained throats j directly connected to a drained, eroded throat i. To estimate how much material eroded from drained throat i is redeposited into the non-drained throats j that are directly connected to it, we consider the pressure drop δp_j across each of j. Because the length of an individual pore throat, assumed to be uniform throughout the network, is much smaller than the overall length of the pore network (i.e., $N \gg 1$), we assume that δp_j is approximately constant across each downstream pore j, as given by the Hagen–Poiseuille equation. Thus, the flux of material into each throat j is proportionate to r_j^4; we therefore assume that the new volume added to each of the n connected throats j, δV_j, after a volume V_{erode} is eroded by drainage in throat i is given by $\delta V_j = \frac{r_j^4}{\sum_{k=1}^{n} r_k^4} V_{\text{erode}}$, reducing the values of $\tilde{r}'_j$ accordingly. However, if δV_j causes $\tilde{r}_j < 0$, the excess volume is returned to the drained throat i to conserve

mass and the throat is removed from the network to prevent subsequent flow through it.

5.2 Model implementation

To characterize the influence of solid erosion & deposition on fluid drainage, we perform numerical simulations of this model with $N = 200$, $c = 4$, and $\rho(\tilde{r}_{i,p})$ given by a uniform distribution spanning $\tilde{r}_{i,p} \in [0.83, 1]$; we find similar results to those described below when exploring other values of N, c, and forms of $\rho(\tilde{r}_{i,p})$, including those obtained from real-world media (Figs. 5.5-5.8). For each simulation condition tested, parameterized by prescribed input values of $(\tilde{t}_d, \tilde{\Sigma})$, we run 100 unique iterations, each with $\tilde{r}_{i,p}$ randomly sampled from the same $\rho(\tilde{r}_{i,p})$. In each simulation, the pore bodies and throats all start saturated with the wetting fluid, and drainage is initiated by introducing the non-wetting fluid at the four central pore bodies. During each time step, we then determine the connected component clusters of undrained pore bodies; the boundaries with these clusters delineate the invading non-wetting fluid interface or trapped wetting fluid regions. Following standard invasion percolation, we then identify the largest pore throat i, with the smallest capillary pressure threshold $\Delta p_c \sim 1/\tilde{r}_i$, along the invading non-wetting fluid interface. We fill the corresponding pore throat and body, keeping trapped wetting fluid regions unchanged to model an incompressible fluid, and incorporating solid erosion & deposition following the rules described above. We then iterate through time steps until the non-wetting fluid reaches the periphery of the network or is completely surrounded by clogged pores.

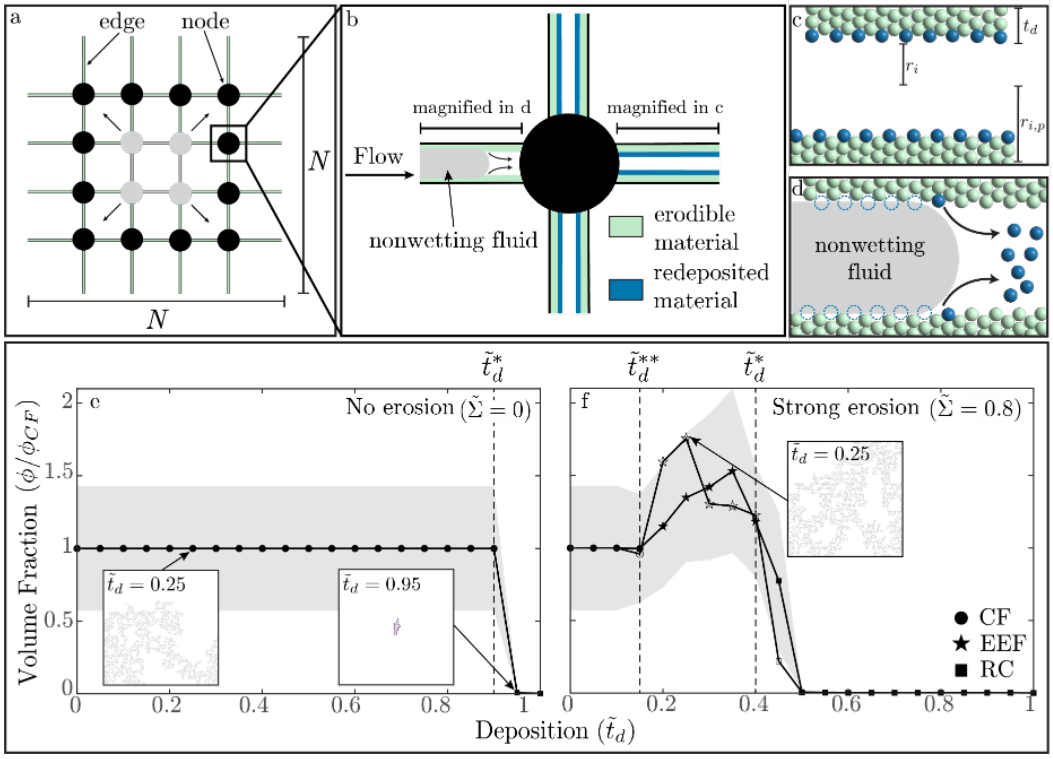


Figure 5.1: Network modeling of fluid drainage in an erodible porous medium reveals new drainage behaviors. (a) Schematic of the 2D network model, with $N \times N$ nodes representing the pore bodies, and the edges representing the interconnecting pore throats. (b) Magnified view of a single pore body. (c) Pore throats initially have a pristine radius $r_{i,p}$, with an initial layer (mint) of erodible material t_d thick. (d) As the non-wetting fluid enters a pore during drainage, it erodes some of this material, redepositing it into connected throats (blue). Numerical simulations reveal new drainage behaviors arising from solid erosion & deposition; we characterize these behaviors in (e–f) using the volume fraction of the pore space filled by the non-wetting fluid after drainage completes, φ, normalized by the case of standard capillary fingering (CF), φ_{CF}. Open symbols show the results for the single network used to generate the simulations shown in the insets. Closed symbols and gray shading show the average and standard deviation, respectively, of results obtained over 100 different, but statistically-identical, networks. (e) Without erosion ($\tilde{\Sigma} = 0$), drainage proceeds by CF (magnified view in left inset) until $\tilde{t}_d > \tilde{t}_d^* \approx 0.9$, above which the medium starts with so much erodible material that pores near the inlet are clogged. The medium transitions to rapid clogging (RC), shown by the magnified view in the right inset; circular gray and purple markers indicate invaded and clogged pore throats, respectively, while gray $+$ symbols denote invaded pore bodies. (f) With strong erosion ($\tilde{\Sigma} = 0.8$), drainage proceeds by CF only until $\tilde{t}_d > \tilde{t}_d^{**} \approx 0.15$, above which the non-wetting fluid unexpectedly explores *more* of the pore space than in CF. Drainage proceeds by erosion-enhanced fingering (EEF), shown by the magnified view in the inset. With increasing $\tilde{t}_d > \tilde{t}_d^* \approx 0.4$, clogging increasingly dominates, and drainage transitions back to RC.

As a baseline, we first establish the classic case of invasion percolation without any erosion ($\tilde{t}_d = 0, \tilde{\Sigma} = 0$). As expected, drainage occurs through a series of successive bursts along a ramified, disordered pathway characteristic of typical CF (Movie S1). The resulting non-wetting fluid pathway fills a fraction $\varphi = \varphi_{CF} = 0.10 \pm 0.04$ of the total pore space volume and has a fractal dimension[230] $d_f = 1.86 \pm 0.04$, in good agreement with previous studies of CF[142,215,218]. Furthermore, slightly increasing the amount of erodible material, but without any erosion ($0 < \tilde{t}_d < 0.9, \tilde{\Sigma} = 0$), still results in CF (Fig. 5.1e, left & Movie S2)—as expected, since in this case, all pores are simply constricted uniformly. However, increasing further above a threshold value $\tilde{t}_d = \tilde{t}_d^* \approx 0.9$ causes a precipitous drop in φ (Fig. 5.1e, right) as pores near the inlet clog, preventing fluid drainage from occurring (Movie S3). We therefore call this behavior *rapid clogging* (RC).

Next, we explore the case of high erodibility ($\tilde{\Sigma} = 0.8$). When the amount of material that can be eroded is small ($\tilde{t}_d \leq 0.1$), the influence of erosion & deposition is minimal, and drainage again proceeds through typical CF (Fig. 5.1f, circles). We observe dramatically different behavior with increasing $\tilde{t}_d$. Above a threshold value $\tilde{t}_d = \tilde{t}_d^{**} \approx 0.15$, the non-wetting fluid volume fraction is *larger* than in CF ($\varphi/\varphi_{CF} > 1$, Fig. 5.1f, stars)—that is, as *more* erodible material is added to the pore space, the non-wetting fluid is somehow able to form new, ramified fingers and thereby drain *more* of the pore space (Fig. 5.1f, inset & Movie S4). We therefore call this behavior *erosion-enhanced fingering* (EEF). This surprising behavior persists with increasing $\tilde{t}_d$ until it eventually becomes suppressed by pore clogging; in this case, we again observe a transition to RC, characterized by a precipitous drop in φ/φ_{CF},

above a threshold value $\tilde{t}_d = \tilde{t}_d^* \approx 0.4$ (Fig. 5.1f, squares).

5.4 Origins of these new drainage behaviors

Why do these fascinating new drainage behaviors arise in erodible porous media? Inspecting changes in the distribution of pore sizes after drainage, which quantifies how the nonwetting fluid displacement has reshaped the pore space structure, provides a clue. In particular, we examine the distributions of $\tilde{r}_i'/(1-\tilde{t}_d) = \tilde{r}_i'/\tilde{r}_{i,\max}$, which describe the pore sizes after drainage relative to the largest starting pore size $\tilde{r}_{i,\max} \equiv \max\{\tilde{r}_i\}$. We focus on the highly erodible case of $\tilde{\Sigma} = 0.8$ described in Fig. 5.1f as a representative example. When the medium only has a little erodible material ($\tilde{t}_d < 0.15$), the initial uniform distribution of pore sizes remains unaltered (Region II in Fig. 5.2). However, as exemplified by $\tilde{t}_d = 0.25$ in Fig. 5.2, just above the threshold $\tilde{t}_d^{**} \approx 0.15$, two sub-fractions of smaller and larger pores (Regions I and III, respectively) split off from this distribution. These reflect the increasing fraction of pore throats that have had solid material eroded from and redeposited in, respectively; indeed, the eroded pores reach a uniform size set by the balance of capillarity and erosion, with $\tilde{r}_i'/\tilde{r}_{i,\max} \approx 1.1 = \tilde{\Sigma}/(1-\tilde{t}_d)$, as expected. Notably, the smaller pores still have sizes $\tilde{r}_i > 0$, indicating that they have not yet reached the threshold for clogging. We observe similar behavior in Fig. 5.2 for the cases of $\tilde{t}_d = 0.35$ and 0.45, for which the eroded pores now reach the expected sizes $\tilde{r}_i'/\tilde{r}_{i,\max} = \tilde{\Sigma}/(1-\tilde{t}_d) \approx 1.2$ and ≈ 1.5, respectively.

Thus, we expect that EEF begins when capillary forces become just large enough to begin eroding the solid matrix—and the redeposition of this material constricts downstream

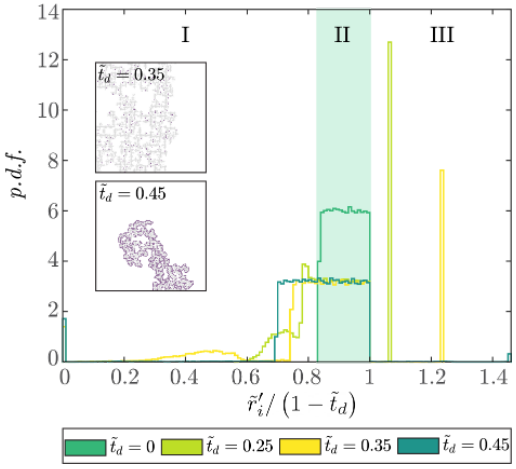


Figure 5.2: Examining the probability density function (*p.d.f.*) of $\tilde{r}_i'/(1-\tilde{t}_d)$, the pore sizes after drainage relative to the largest starting pore size, elucidates the origins of new drainage behaviors. We consider the representative case of strong erosion ($\tilde{\Sigma} = 0.8$) shown in Fig. 5.1f. The initial uniform distribution is shown in Region II for the pristine case without any erodible material ($\tilde{t}_d = 0$). Above the threshold to transition to EEF $\tilde{t}_d \approx 0.15$, two subfractions of smaller and larger pores (Regions I and III) split off—reflecting pores that have had material eroded from and redeposited in, respectively. At larger $\tilde{t}_d$ above the threshold $\tilde{t}_d \approx 0.4$, increasing clogging (peak in Region I) causes a transition to RC. Insets show magnified views of the resulting patterns of non-wetting fluid displacement (gray) and pore clogging (purple) for $\tilde{t}_d = 0.35$ and 0.45.

pores slightly, just enough to force the non-wetting fluid to explore new pathways through the pore space that it otherwise would not have. We quantify this expectation for the onset of EEF by balancing the smallest capillary pressure that can possibly be encountered during drainage, $\Delta p_c \left(r_{p,\max} - t_d^{**}\right)$, with the threshold erosion stress σ_y. In nondimensional form, our prediction is:

$$\tilde{t}_d^{**} = 1 - \tilde{\Sigma}. \tag{5.1}$$

This prediction yields $\tilde{t}_d^{**} = 0.2$, in good agreement with the value of $\tilde{t}_d^{**} \approx 0.15$ found from the simulations for the case of $\tilde{\Sigma} = 0.8$.

As $\tilde{t}_d$ increases above $\tilde{t}_d^{**}$, we expect that the increasing amount of erodible material increases the propensity of pores to become clogged—giving rise to the non-monotonic vari-

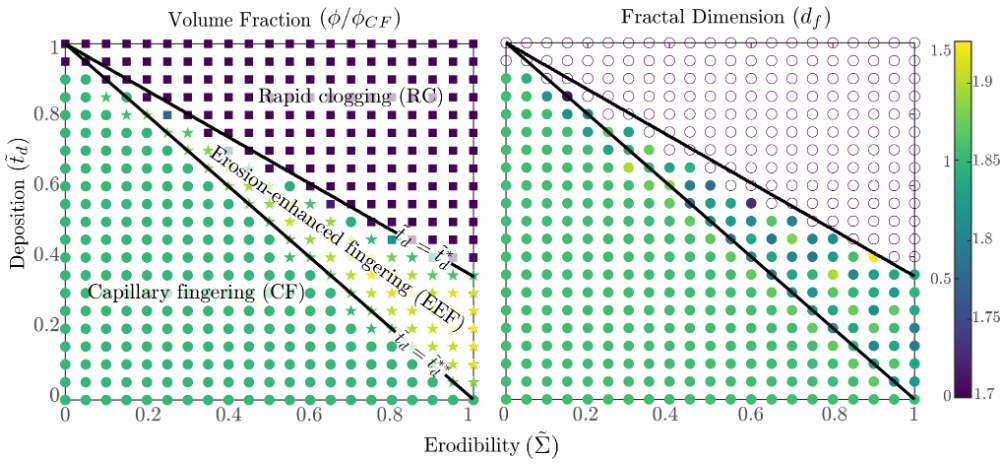


Figure 5.3: State diagrams of the normalized non-wetting fluid volume fraction (left) and fractal dimension (right) for different drainage behaviors in an erodible porous medium. Color bar left axis shows the normalized non-wetting fluid volume fraction (φ/φ_{CF}) and right axis shows the fractal dimension (d_f); each symbol shows the average of 100 different simulations testing different, but statistically-identical, networks. (left) We observe the emergence of three distinct drainage behaviors: capillary fingering (circles, $0.9 < \varphi/\varphi_{CF} < 1$), rapid clogging (squares, $\varphi/\varphi_{CF} < 0.9$), and erosion enhanced fingering (stars, $\varphi/\varphi_{CF} > 1$). (right) Fractal dimension reflects these distinct regimes. In the CF regime, $d_f = 1.86 \pm 0.04$. However, in the EEF regime, the measured fractal dimensions are more varied, indicating that different $(\tilde{\Sigma}, \tilde{t}_d)$ combinations yield non-wetting fluid patterns with more varied ramification. The empty circles indicate the rapid clogging regime, in which the filled volume fraction of the pore network is too low to accurately obtain d_f.

ation of φ shown in Fig. 5.1f. Consistent with this expectation, a larger fraction of pores in Region I becomes clogged (shown by the growing peak at $\tilde{r}_i' = 0$, also indicated by the purple points in the insets to Fig. 5.2 and Movies S5–S6). The height of the peak in Region III concomitantly decreases, indicating that fewer pores are ultimately eroded.

Thus, we expect that EEF transitions to RC when pore clogging is so prevalent that it "chokes off" fluid drainage. We quantify this expectation for the onset of RC by balancing the volume of solid material that can be eroded from a pore i, $V_{\text{erode}} \propto \left(2\gamma/\sigma_y\right)^2 - \left(r_{i,p} - t_d^*\right)^2$, with the cumulative total available volume in the adjacent connected non-drained pore throats j, $V_{\text{available}} \propto \left(r_{j,p} - t_d^*\right)^2$. For tractability of computation, we make the assumption that both $r_{i,p}$ and $r_{j,p} \sim r_{p,\max}$. Thus $V_{\text{erode}} \propto \tilde{\Sigma}^2 - (1 - \tilde{t}_d^*)^2$ and $V_{\text{available}} \propto (1 - \tilde{t}_d^*)^2$. This assump-

tion that $r_{i,p}$ and $r_{j,p} \sim r_{p,\max}$ allows us to make the approximation that fluid drainage will expand radially in sequential annular "layers" from the central injection point (Fig. 5.4)—as opposed to the ramified invasion patterns typical of invasion percolation. On a square lattice of connectivity $c = 4$, layer ℓ experiences $8\ell + 4$ invasions, yielding a total eroded volume $(8\ell+4)V_{erode}$, which gets redeposited onto $8(\ell+1)$ available pore throats with a total available volume of $8(\ell+1)V_{available}$. Thus, taking a mean-field approximation layer by layer, we expect clogging to occur at $\ell = 1$ when $(8\ell + 4)V_{erode} \sim 8(\ell + 1)V_{available}$, or $V_{erode} \sim \frac{4}{3}V_{available}$.

The same result can similarly be obtained for lattices with $c = 3$ and $c = 6$. For a lattice with connectivity $c = 3$, layer ℓ experiences $6(2\ell + 1)$ invasions, yielding a total eroded volume $6(2\ell + 1)V_{erode}$, which gets redeposited onto $6(\ell + 1)$ available pore throats with a total available volume of $6(\ell + 1)V_{available}$. If we similarly expect clogging to occur at $\ell = 1$, $V_{erode} \sim \frac{2}{3}V_{available}$ (Fig. 5.6, left). For a lattice with connectivity $c = 6$, layer ℓ experiences $6\ell + 6$ invasions, yielding a total eroded volume $(6\ell + 6)V_{erode}$, which gets redeposited onto $12(\ell + 1) + 6$ available pore throats with a total available volume of $(12(\ell + 1) + 6)V_{available}$. If we similarly expect clogging to occur at $\ell = 1$, $V_{erode} \sim \frac{5}{2}V_{available}$ (Fig. 5.6, right).

In nondimensional form, incorporating this simplification yields the following prediction:

$$\tilde{t}_d^* = 1 - \frac{\tilde{\Sigma}}{\sqrt{1+\alpha}}. \tag{5.2}$$

This prediction yields $\tilde{t}_d^* = 0.4$, in excellent agreement with the value of $\tilde{t}_d^* \approx 0.4$ found from the simulations, for the case of $\tilde{\Sigma} = 0.8$.

5.5 A unified state diagram for drainage in an erodible porous medium

As a final test of the predictions given by Eqs. (5.1) & (5.2), we perform a total of 44,100 numerical simulations over a broad range of $(\tilde{t}_d, \tilde{\Sigma})$. We characterize the drainage pattern that emerges for each condition tested using the volume fraction and fractal dimension[230] of the non-wetting fluid pathway, φ and d_f, respectively. Our results are summarized in Fig. 5.3. Consistent with the observations shown in Figs. 5.1–5.2, CF emerges for small $(\tilde{t}_d, \tilde{\Sigma})$ (circles), transitioning to EEF for $\tilde{t}_d \geq \tilde{t}_d^{**}$ (stars), and then transitioning to RC for $\tilde{t}_d \geq \tilde{t}_d^{*}$ (stars). Moreover, the boundaries between these distinct drainage behaviors agree well with the predictions given by Eqs. (5.1) & (5.2), shown by the lower and upper solid lines, respectively—despite the simplifying assumptions made therein. Thus, not only has our extended model of invasion percolation shown that the coupling between non-wetting fluid displacement and solid erosion & deposition engender fascinating new drainage behaviors, but our analysis provides quantitative principles to help predict when they arise. Future work could build on the framework developed here by exploring a broader range of fluid viscosity ratios[224] and flow rates (extending Lenormand's classic phase diagram[156]), as well as different forms of pore space structure[161,168,231–237], and different rules for erosion, clogging, and potential clog erosion—ultimately leading to improved prediction and control of coupled fluid and solid transport in diverse environmental and industrial media.

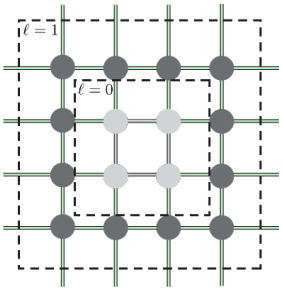


Figure 5.4: Schematic of fluid drainage proceeding from the initialization of a simulation. The light gray pore bodies connected by light gray pore throats represent the injection source used in all simulations. The pore throats in layer 0, denoted $\ell = 0$, are invaded to fill the first layer of pore bodies, shown in darker gray ($\ell = 1$). The volume eroded from the pore bodies in the first layer is then eroded into its connected pore throats, which are shown in mint green. We expect clogging to occur at $\ell = 1$, when the ratio of available pore throats to previously invaded pore bodies provides a value of $\alpha = 4/3$.

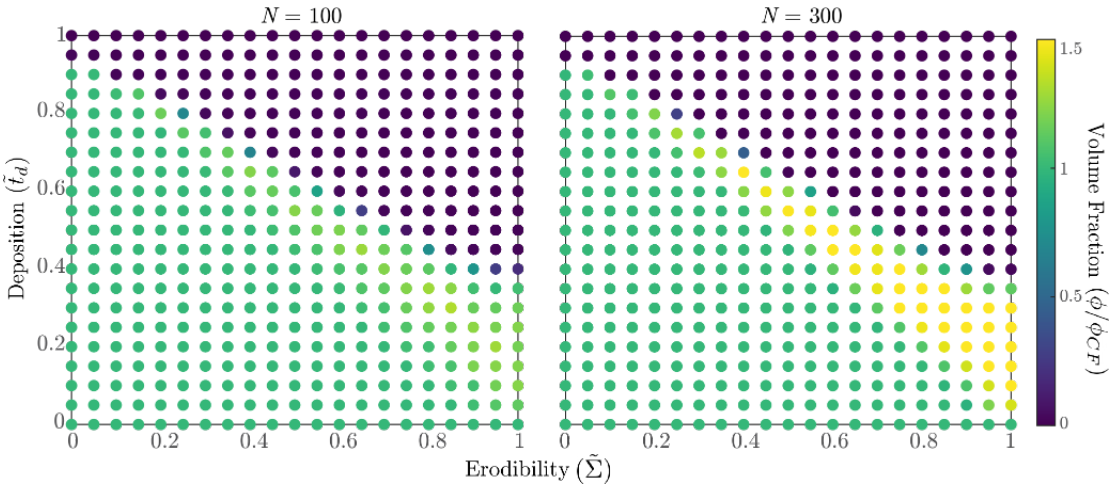


Figure 5.5: Additional state diagrams of non-wetting fluid filled volume fraction (φ/φ_{CF}) for networks with different $N = 100$ (left) and $N = 300$ (right), across the full range of deposition ($\tilde{t}_d$) and erodibility ($\tilde{\Sigma}$) values. For both system sizes, we again observe the emergence of capillary fingering, rapid clogging, and erosion enhanced fingering, with the boundaries between these different drainage behaviors remain unchanging and in good agreement with the results shown in the main text. The magnitude of φ/φ_{CF} increases slightly, and then converges to $\varphi/\varphi_{CF} \approx 1.7$, with increasing N.

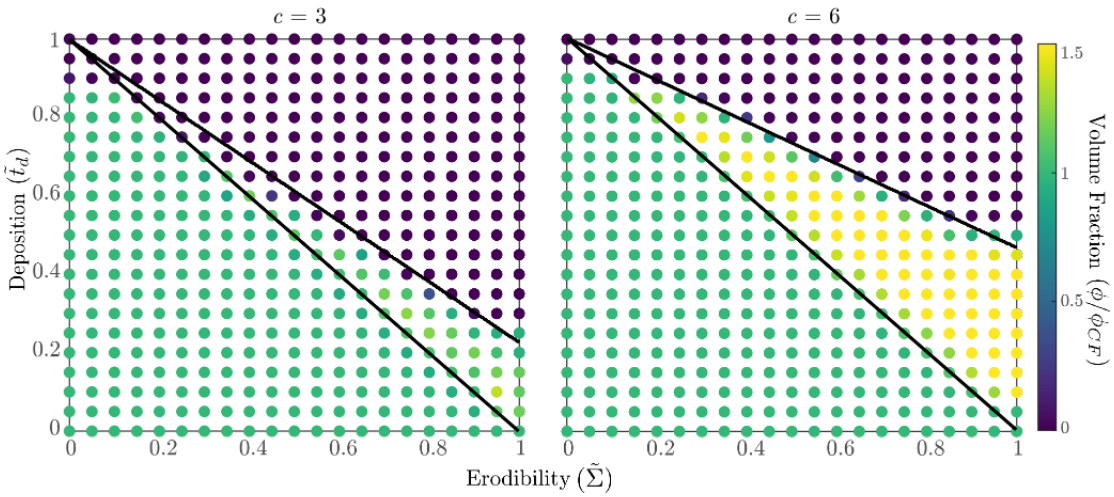


Figure 5.6: Additional state diagrams of non-wetting fluid filled volume fraction (φ/φ_{CF}) for networks with different connectivity, $c = 3$ (left) and $c = 6$ (right), across the full range of deposition ($\tilde{t}_d$) and erodibility ($\tilde{\Sigma}$) values. In both cases, we again observe the emergence of capillary fingering, rapid clogging, and erosion enhanced fingering, as in the main text. The erosion-enhanced fingering regime spans a smaller (larger) range of $(\tilde{t}_d, \tilde{\Sigma})$, and the corresponding φ/φ_{CF} is smaller (larger), for the case of $c = 3$ ($c = 6$). These changes are captured by our theory when we account for network connectivities. When $c = 3, \alpha = 2/3$, and when $c = 6, \alpha = 5/2$.

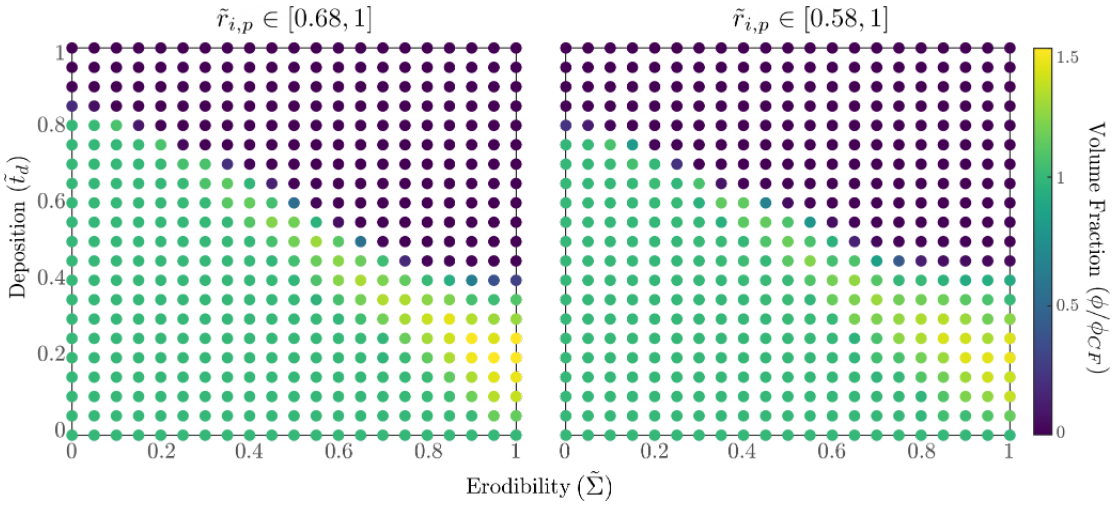


Figure 5.7: Additional state diagrams of non-wetting fluid filled volume fraction (φ/φ_{CF}) for wider uniform distributions, $\tilde{r}_{i,p} \in [0.68, 1]$ (left) and $\tilde{r}_{i,p} \in [0.58, 1]$ (right), across the full range of deposition ($\tilde{t}_d$) and erodibility ($\tilde{\Sigma}$) values. In both cases, we again observe the emergence of capillary fingering, rapid clogging, and erosion enhanced fingering, as in the main text. The erosion-enhanced fingering regime spans a smaller range of $(\tilde{t}_d, \tilde{\Sigma})$ as the distributions become wider.

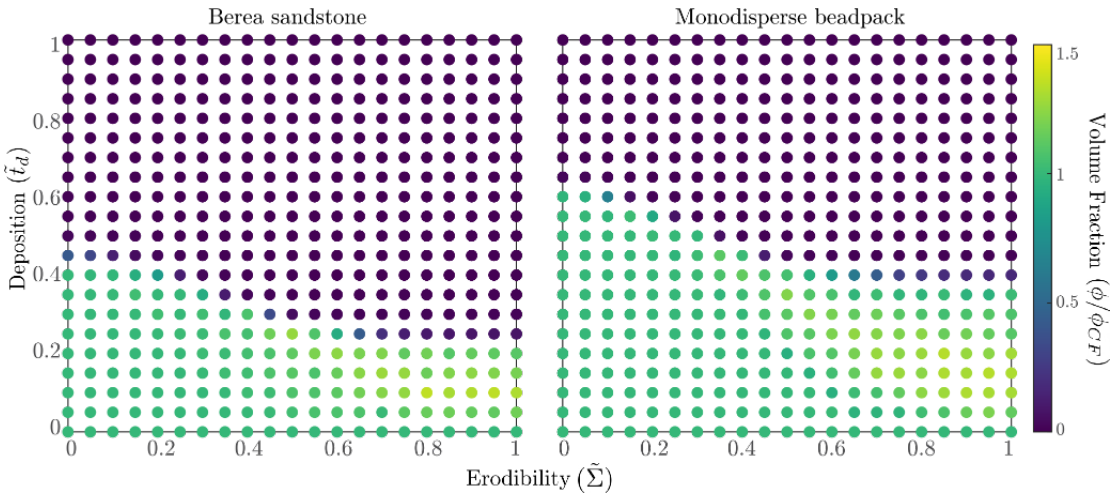


Figure 5.8: Additional state diagrams of non-wetting fluid filled volume fraction (φ/φ_{CF}) for non-uniform $\rho(r_{i,p})$ that are representative of two real-world examples as obtained from [238]: Berea sandstone (left) and a monodisperse bead packing (right). The Berea sandstone has $\rho(r_{i,p}) = \frac{15}{4(r_{max}-r_{min})}\left(1-\frac{r_{i,p}-r_{min}}{r_{max}-r_{min}}\right)\sqrt{\frac{r_{i,p}-r_{min}}{r_{max}-r_{min}}}$, with $r_{min} = 1$ µm and $r_{max} = 25$ µm. The bead packing has $\rho(r_{i,p}) = \frac{6}{(r_{max}-r_{min})}\sqrt{\frac{r_{i,p}-r_{min}}{r_{max}-r_{min}}}\sqrt{1-\frac{r_{i,p}-r_{min}}{r_{max}-r_{min}}}$, with $r_{min} = 15$ µm and $r_{max} = 40$ µm. In both cases, we again observe the emergence of capillary fingering, rapid clogging, and erosion enhanced fingering, as in the main text.

5.7 Supplementary Movie Captions

The movies corresponding to data in this chapter can be found in the repository at: https://github.com/joannaclaireschneider/dissertation-movies.

Movie S1. Invasion percolation in a pore network with $(\tilde{\Sigma}, \tilde{t}_d) = (0, 0)$ shows the traditional invasion percolation algorithm and an example of a classic capillary fingering pattern. Gray circles denote pore throats invaded by the non-wetting fluid and gray + symbols denote invaded pore bodies. The left panel shows a view of the entire network. The blue box denotes the magnified view shown in the right panel for clarity.

Movie S2. Invasion percolation in a pore network with $(\tilde{\Sigma}, \tilde{t}_d) = (0, 0.25)$ returns the traditional invasion percolation algorithm and shows an example of a classic capillary fingering pattern. Gray circles denote pore throats invaded by the non-wetting fluid and gray + symbols denote invaded pore bodies. The left panel shows a view of the entire network. The blue box denotes the magnified view shown in the right panel for clarity.

Movie S3. Invasion percolation in a pore network with $(\tilde{\Sigma}, \tilde{t}_d) = (0, 0.95)$ shows that only a few invasions occur before clogging occurs, choking off subsequent flow. Gray circles denote pore throats invaded by the non-wetting fluid and gray + symbols denote invaded pore bodies. Purple circles denote clogged pore throats. The left panel shows a view of the entire network. The blue box denotes the magnified view shown in the right panel for clarity.

Movie S4. Invasion percolation in a pore network with $(\tilde{\Sigma}, \tilde{t}_d) = (0.8, 0.25)$ shows a markedly different non-wetting fluid invasion pattern that fills more of the pore space than

capillary fingering alone. No clogging occurs during this simulation. Gray circles denote pore throats invaded by the non-wetting fluid and gray + symbols denote invaded pore bodies. The left panel shows a view of the entire network. The blue box denotes the magnified view shown in the right panel for clarity.

Movie S5. Invasion percolation in a pore network with $(\tilde{\Sigma}, \tilde{t}_d) = (0.8, 0.35)$ shows another non-wetting fluid invasion pattern that fills more of the pore space than capillary fingering alone. Intermittent clogging also occurs in this simulation. Gray circles denote pore throats invaded by the non-wetting fluid and gray + symbols denote invaded pore bodies. Purple circles denote clogged pore throats. The left panel shows a view of the entire network. The blue box denotes the magnified view shown in the right panel for clarity.

Movie S6. Invasion percolation in a pore network with $(\tilde{\Sigma}, \tilde{t}_d) = (0.8, 0.45)$ shows another non-wetting fluid invasion pattern that appears dense, but clogging chockes off flow before the non-wetting fluid can percolate through the network. Gray circles denote pore throats invaded by the non-wetting fluid and gray + symbols denote invaded pore bodies. Purple circles denote clogged pore throats. The left panel shows a view of the entire network. The blue box denotes the magnified view shown in the right panel for clarity.

We are stardust, we are golden

We are billion year old carbon

And we got to get ourselves back to the garden.

Joni Mitchell, Woodstock

6

Designing hybrid nanoparticles for groundwater remediation

In Chapters 2 through 4, we unraveled the complex physics that describe how colloids and immiscible fluids interact in porous media. Much of this work sought to address

mobilization of the immiscible fluid, either by harnessing colloids or by better understanding their innate impact on immiscible fluid flow and mobilization to make more accurate predictions. As a result, the lens under which we study these phenomena relied primarily on physical approaches. However, typical approaches to remediation of oil-based contaminants often lean heavily on the synthesis of novel materials. While many of these materials exhibit promising reactivity in bulk liquid, most widely used nanomaterials, such as zero valent iron nanoparticles (nZVI) and metal oxides, aggregate over time scales on the order of minutes, reducing their reactivity and mobility in tortuous, confined pore spaces[15–17]. Others, like gold (Au) nanoparticles, are too expensive for widespread use due to the large amounts of material that need to be injected, thus preventing their widespread implementation[18].

While most research on the use of reactive nanoparticles has focused on their stabilization through the use of surfactants or polymer coatings[46,56–59], a newer class of nanoparticles called hybrid nanoparticles (hNPs) may be of particular interest in groundwater remediation due to their ability not only to stabilize, but to *control* the loading of reactive nanomaterials. Several methods have been explored to produce nanostructured and hybrid colloids, including self-assembly[69–71], self-organized precipitation (SORP)[72–75], and Flash NanoPrecipitation (FNP)[76–78]. However, widespread use of some of these methods may be hindered by more complex, multi-step fabrication techniques[79–82]. Despite their success in producing hybrid nanostructured particles, previously reported experimental techniques often require

This chapter has been adapted from published work by Joanna Schneider, Jason X. Liu, Victoria E. Lee, Robert K. Prud'homme, Sujit S. Datta, and Rodney D. Priestley. Tuning morphologies and reactivities of hybrid organic–inorganic nanoparticles. *ACS Nano*, 16, 2022.[5] **Author Contributions:** J.S., V.E.L., and R.D.P. designed the experiments; J.S. and J.X.L. performed all experiments; J.S. analyzed the data; R.D.P. designed and supervised the overall project. All authors discussed the results. J.S., J.X.L., and R.D.P. wrote the manuscript.

modification of the metal component to be compatible with the appropriate polymeric domain and require several days to produce the final particle suspensions, presenting opportunities for improvement in total production time, and simplified, scalable fabrication.

In this chapter, we overcome these limitations by demonstrating a method to produce stable hNPs with tunable morphologies. By incubating polystyrene nanoparticles formed *via* Flash NanoPrecipitation with citrate-stabilized gold nanocatalysts, we find that gold adsorption to polystyrene nanoparticles is enabled by the presence of a good solvent for the polymer. Furthermore, changing process parameters, such as gold incubation time, and molecular parameters, such as polymer molecular weight and end-group functionality, provides control over the resultant nanocatalyst loading and dispersal atop hNPs. We classify these morphologies into three distinct regimes: aggregated, dispersed, or internalized, and we show that the emergence of these regimes has key implications for controlling reaction rates in applications such as heterogeneous catalysis or groundwater remediation. Specifically, we find that hNPs with gold nanocatalysts embedded *below* the surfaces of polystyrene nanoparticles exhibit slower bulk catalytic reduction capacity than their disperse, surface-decorated counterparts. Taken together, the results presented in this chapter demonstrate a simple way by which hNPs can be fabricated and present a unique method to control catalytic reactions using reactive nanomaterials.

Two-step hybrid nanoparticle fabrication. To prepare polystyrene nanoparticles (PS NPs), we dissolve 0.3 mg/mL uncrosslinked polystyrene with hydrophobic butyl end-groups of varying molecular weight ($M_n = 10$ kg/mol, 99 kg/mol, or 646 kg/mol, *Polymer Source*), and therefore a varying number of repeat units ($N \approx 96$, 950, and 6200, respectively) in tetrahydrofuran (*Sigma Aldrich*), which is a good solvent for the polymer. We vary surface charge by replacing pure PS with a blend of 0.1 mg/mL PS ($M_n = 10$ kg/mol) and 0.1 mg/mL amine-terminated polystyrene (PS-NH_2, $M_n = 10$ kg/mol, *Sigma Aldrich*). We then mix solutions of varying volume percentages from 0% to 50% PS-NH_2 to produce PS/PS-NH_2 colloids. Size measurements obtained from dynamic light scattering (DLS) for all PS and PS/PS-NH_2 NPs are reported in Fig. 6.12 and Fig. 6.13 (*Anton Paar Litesizer 500*). Zeta potential measurements for all samples are reported in Section 6.7.

We purchase citrate-stabilized gold nanocatalysts (Au NCs) with a diameter, $d = 5$ nm from *Nanopartz*. Citrate-stabilized Au NCs with $d = 20$ nm and $d = 40$ nm are synthesized using the method proposed by Turkevich and Frens[239,240], in which we bring a 0.01 wt% solution of chloroauric acid ($HAuCl_4$) to a rolling boil and then rapidly add a solution of 2 wt% or 0.4 wt% sodium citrate ($NaC_6H_5O_7$) to produce 20 nm or 40 nm Au NCs, respectively. The solution continues to boil until a deep red color is achieved, approximately 20 minutes. Au NCs used in this study have a diameter $d = 20.9$ nm with a PDI of 0.11 or $d = 38.0$ nm with a PDI of 0.26, measured *via* DLS (Fig. 6.14). Au NCs fabricated using this experimental method have been reported to have a zeta potential, $\zeta = -39.7 \pm 0.7$ mV at pH 9.3[241].

We perform Flash NanoPrecipitation (FNP) to produce PS or PS/PS-NH_2 NPs using a confined impinging jet (CIJ) mixer (Fig. 6.1a). The prepared PS solutions are impinged against an equal volume of deionized water, which is a poor solvent, or anti-solvent, for PS. The effluent stream is then deposited into an anti-solvent reservoir to produce NPs with sizes ranging from 200 to 500 nm, depending on the inlet PS concentration. The volume ratio of the polymer solution to the anti-solvent stream to the anti-solvent reservoir for all experiments is 1:1:1, resulting in a final solvent concentration of 33.3% THF and 66.6% deionized water. We fabricate hNPs by incubating our prepared PS or PS/PS-NH_2 NPs in 33.3% THF with excess Au NCs at a 2:1 ratio with a final solvent composition of 22.2% THF for 1 hour (Fig. 6.1a). Any excess, unadsorbed Au NCs are removed from the hNP suspension *via* centrifugation prior to imaging.

Sample preparation for imaging *via* transmission electron microscopy (TEM). To prepare particles for transmission electron microscopy (TEM), 1.5 mL hNPs are centrifuged twice to remove any unadsorbed Au NCs (16,000 g for 15-45 min, depending on PS NP size) and resuspended in 50-150 μL deionized water before dropcasting 8 μL of the washed, concentrated suspension onto carbon-coated copper TEM grids (CF-200-Cu, *Electron Microscopy Sciences*). Samples are left to dry overnight before imaging. We acquire all images using an FEI Talos F200X TEM with an accelerating voltage of 200 kV.

Electron tomography and reconstruction of 3D Au NC distributions. All tomography images are also acquired on an FEI Talos F200X TEM with an accelerating voltage of 200 kV at a -1 μm defocus. We place dried, drop cast samples on carbon-coated copper TEM grids onto a $\pm 70°$ tomography holder and take images at 1° increments from $-60°$ to $+60°$. Tomographic reconstructions are performed using the ASTRA toolbox in MATLAB[242]. We

employ a parallel beam geometry and perform reconstructions with 150 iterations of the simultaneous iterations reconstruction technique.

Image analysis and quantification of hybrid nanoparticle morphologies. To quantify Au nanocatalyst adsorption atop the surface of PS NPs, we manually isolate each imaged PS particle for a given data set (*i.e.,* unique experimental conditions and imaging specifications) and binarize using multilevel thresholding in MATLAB. We chose a global threshold level for each data set that allows for optimal isolation of the contrast obtained only from Au NCs, ignoring any contrast from PS NPs themselves. We then manually adjust thresholding that does not adequately isolate Au NC contrast for individual particles. To quantify Au NC cluster sizes and count the number of Au NCs adsorbed to each PS NP, we use a built-in MATLAB function, "bwconncomp," and normalize the obtained values by the average Au NC size measured *via* DLS. Each experimental condition represents between 40 and 100 individual PS NPs depending on the density of deposited particles on TEM grids.

6.2 Gold nanocatalyst adsorption to polystyrene nanoparticles

To produce hNPs, we mix polystyrene nanoparticles produced *via* FNP with previously fabricated gold nanocatalysts, as shown in Fig. 6.1a. Before incubation with Au NCs, we first remove tetrahydrofuran (THF) from the PS NP suspension *via* rotary evaporation because the presence of a toxic, volatile organic solvent in the final particle suspension is undesirable for many applications, such as environmental remediation and drug delivery.[243,244] However, we observe that incubating Au NCs with PS NPs in 100% water results in little to no

Au NC adsorption (Fig. 6.1b). When we quantify this observation for many transmission electron microscopy (TEM) images, we observe that most PS NPs adsorb fewer than 5 Au NCs when THF is not present during the incubation step (Fig. 6.1d, top). Furthermore, the few Au NCs that are attached appear to be caught between PS NPs while drying on TEM grids, rather than becoming embedded atop their surfaces.

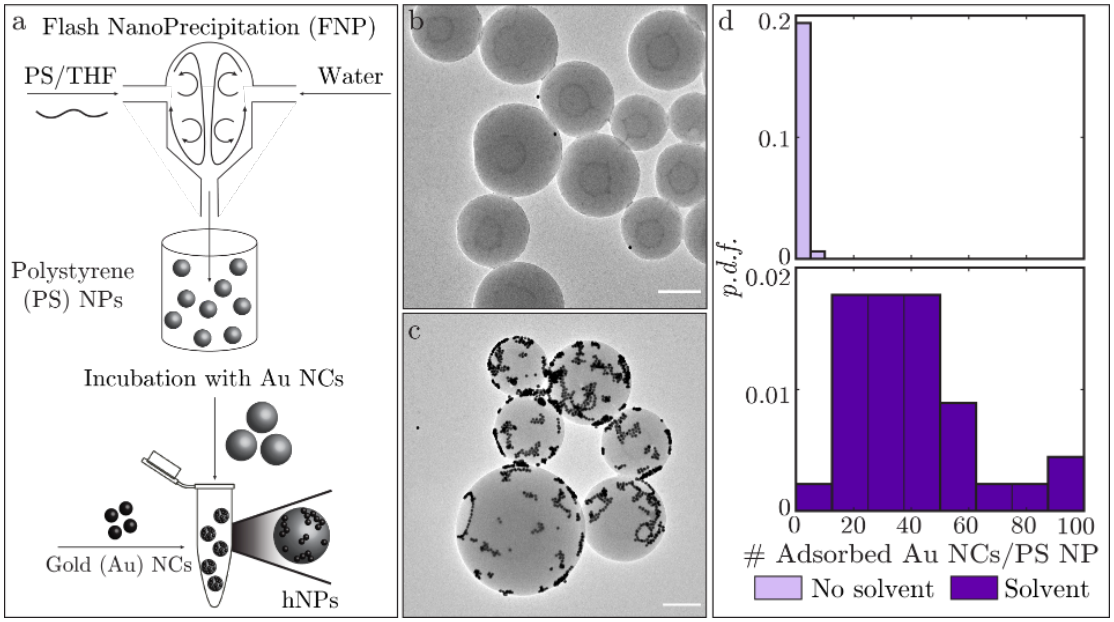


Figure 6.1: The presence of a good solvent for PS during incubation with Au NCs promotes adsorption. (a) Schematic of hNP formation via Flash NanoPrecipitation (FNP) and incubation with Au NCs. PS NPs are represented schematically and in transmission electron microscopy (TEM) images in gray, and Au NCs are represented in black. (b) Hybrid NP formation in the absence of a good solvent. When THF is removed prior to incubation of PS NPs with Au NCs, there is no appreciable adsorption of Au NCs to PS NPs. (c) Hybrid NP formation in the presence of a good solvent. When THF is present in the PS and Au NC mixture during incubation, Au NCs adsorb to PS NPs. (d) Comparison of the probability density function (*p.d.f.*) of adsorbed Au NCs per PS NP in the absence (top) or presence (bottom) of a good solvent. All PS NPs have fewer than 10 Au NCs adsorbed to their surfaces when THF is absent during incubation. When THF is present, most PS NPs have greater than 10 Au NCs adsorbed to their surfaces. Scale bars in (b) and (c) are 200 nm.

However, when residual THF from PS NP fabrication is not removed prior to incubation with Au NCs, we observe a striking difference. In a final solvent mixture of 22.2% THF and 78.8% water, Au NCs strongly adsorb atop PS NPs despite the fact that there are no known

attractive functional groups on PS NP surfaces to stabilize citrate-coated Au NCs. In one example, we observe the formation of two-dimensional (2D) Au NC aggregates atop PS NPs (Fig. 6.1c). Furthermore, across varying surface configurations of Au NCs atop PS NPs, we find that most PS NPs contained between 10 and 60 Au NCs adsorbed to their surfaces, representing considerable adsorption, which we define as number of adsorbed Au NCs per PS NP $>$ 10 (Fig. 6.1d, bottom). These results demonstrate that the presence of THF is necessary to facilitate Au NC adsorption to PS NPs.

To address the presence of THF in the final hybrid nanoparticle (hNP) suspension, we also investigate the impact of post-incubation rotary evaporation. By completing the incubation step in the previously employed solvent mixture of 22.2% THF and 78.8% water before removing THF, we find that Au NC adsorption atop PS NPs obtained through incubation in the presence of THF is retained once THF is removed (Fig. 6.2). Moreover, the number of adsorbed Au NCs per PS NP remains above the threshold for considerable adsorption ($>$ 10 Au NCs) under these conditions.

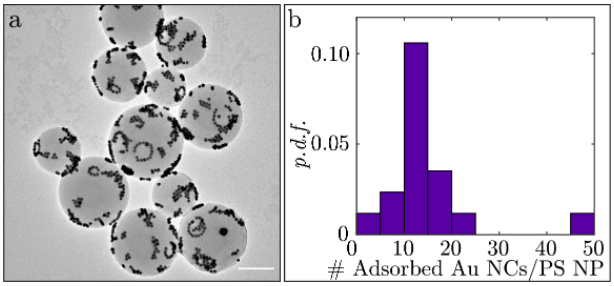


Figure 6.2: The presence of solvent during incubation is essential for adsorption. (a) Hybrid nanoparticle morphology after solvent is removed post-incubation. We see the same magnitude of Au NC adsorption to polystyrene particles when solvent is removed post-incubation versus when solvent is not removed. Scale bar is 200 nm. (b) Probability density function (*p.d.f.*) of the number of adsorbed Au NCs per PS NP. When THF is present during incubation, all PS NPs exhibit Au NC adsorption, as we see in Fig. 1d (bottom). Similarly, we also see that most PS NPs contain greater than adsorbed Au NCs, with most PS particles adsorbing between 10 and 50 Au NCs to their surfaces.

To probe the sensitivity of Au NC adsorption atop PS NPs to THF concentration, we

next investigate the ability of hNPs to form by adding Au NCs of varying diameter (5, 20, and 40 nm) to PS NP suspensions with varying solvent compositions. First, we consider the control case in which Au NCs are incubated with PS NPs without THF (Fig. 6.3(a-c)i). For all Au NC sizes, we anticipate that no adsorption should occur, which is indeed what we observe in the first column of Fig. 6.3. In all samples without THF, we observe a few Au NCs, but the number of adsorbed Au NCs per PS NP $\ll$ 10. Furthermore, TEM images reveal that most Au NCs still present after centrifugation appear to be aggregated between PS NPs rather than adsorbed atop them, which we hypothesize to be a result of drying on TEM grids.

When we increase the THF concentration to 10%, we begin to observe differences in Au NC adsorption across the tested range of Au NC sizes (Fig. 6.3(a-c)ii). Specifically, we observe hybrid NP formation when $d_{Au} = 5$ nm (Fig. 6.3a.ii), while incubation with 10% THF is insufficient to result in considerable adsorption of 20 or 40 nm Au NCs atop PS NPs (Fig. 6.3b.ii, c.ii). This difference in adsorption suggests that THF may enhance the mobility of Au NCs within PS. Ten percent THF is enough to enhance Au NC mobility within a surface layer $\geq$ 5 nm thick because we see hybrid NP formation with 5 nm Au NCs, but that layer must also be thinner than 20 nm because we do not see hybrid NP formation with Au NCs $\geq$ 20 nm (Fig. 6.3b.ii, c.ii).

Increasing the THF concentration further to 20% reveals a similar trend (Fig. 6.3(a-c)iii). Here, we observe that 20% THF is sufficient to produce hNPs in the presence of both 5 and 20 nm Au NCs, suggesting that the surface layer of PS allows for enhanced mobility within an outer radius of $\geq$ 20 nm (Fig. 6.3a.iii, b.iii). We also begin to see a change in 40 nm Au NC adsorption (Fig. 6.3c.iii), but the average number of adsorbed Au NCs remains

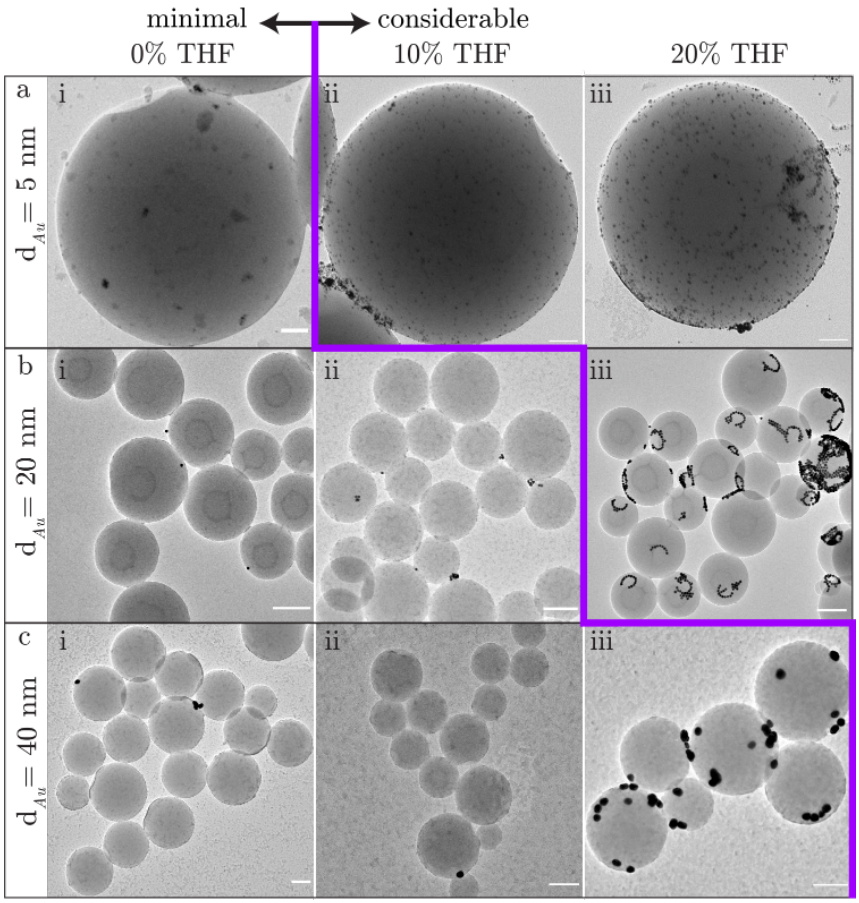


Figure 6.3: THF concentration impacts the ability of Au NCs to adsorb atop PS NPs. (a) Adsorption of 5 nm Au NCs occurs only when a minimum concentration of 10% THF is present during incubation. (b) Adsorption of 20 nm Au NCs occurs when 20% THF is present during incubation. (c) We observe slight adsorption of 40 nm Au NCs to PS NPs at a THF incubation concentration of 20%, but appreciable adsorption occurs at a threshold value of 30% THF. The purple line delineates the THF concentration above which the transition between minimal (fewer than 10 Au NCs) and considerable (greater than 10 Au NCs) adsorption occurs. Scale bars in (a) are 50 nm. Scale bars in (b) and (c) are 200 nm.

below the threshold for considerable adsorption of $>$ 10 Au NCs per PS NP (Fig. 6.4a). We believe this transition is more gradual because Au NCs are at most 2 times larger than the PS NP surface layer, potentially allowing for some favorable adsorption (Fig. 6.3c.iii). Despite this more gradual adsorption onset, we only begin to see considerable adsorption of 40 nm Au NCs at higher THF concentrations, $\geq$ 30% (Fig. 6.4b). Thus, the strong correlation between increasing THF concentration and the ability for larger Au NCs to adsorb atop PS NPs establishes a criterion for their formation, as indicated by the purple stair-step that delineates the transition between minimal and considerable adsorption of Au NCs atop PS NPs (Fig. 6.3).

6.3 Diffusion-based surface aggregation of gold nanocatalysts

We next harness the versatility of our two-step fabrication process to alter hNP surface decoration by exploring one process parameter, incubation time, and one molecular parameter, PS molecular weight. First, we investigate how incubation time of PS NPs with excess Au NCs affects the surface decoration of hNPs, for which we use a final solvent mixture of 22.2% THF and 78.8% water. Using PS with $M_n = 100$ kg/mol as our baseline, we observe disperse Au NCs on the surfaces of PS NPs (Fig. 6.5a) after 1 hour. We consider Au NCs to be disperse when a large population of Au NC clusters contains fewer than 2 Au NCs and none or few Au NC clusters exceed sizes of 10 Au NCs. For example, after 1 hour of incubation, $>$ 40% of clusters contain fewer than 2 Au NCs and $>$ 90% of clusters contain fewer than 10 Au NCs (Fig. 6.5d).

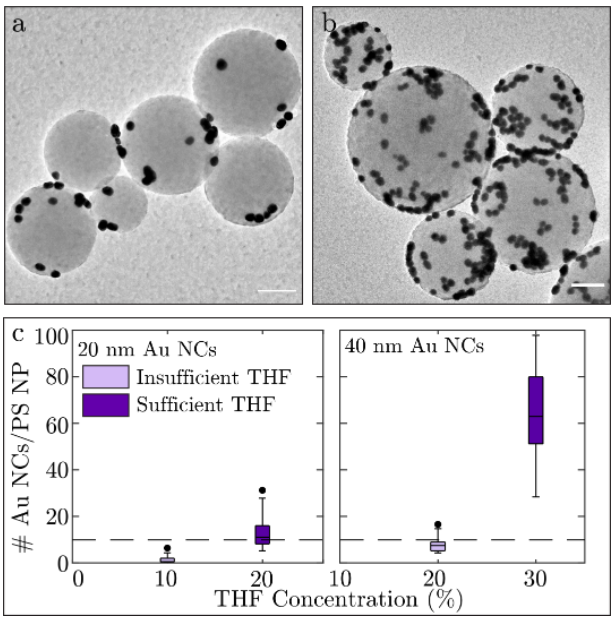


Figure 6.4: Quantification of the threshold for considerable Au NC adsorption. (a) Example of 40 nm Au NC adsorption to PS NPs in 20% THF shows minimal adsorption. On average, fewer than 10 Au NCs adsorb to PS NPs in the presence of only 20% THF for $d_{Au} = 40$ nm. (b) Example of 40 nm Au NC adsorption to PS NPs in 30% THF shows considerable adsorption. On average, more than 10 Au NCs adsorb to PS NPs in the presence of 30% THF for $d_{Au} = 40$ nm. (c) Box plots show threshold for considerable adsorption. A comparison of 20 nm Au NC adsorption and 40 nm Au NC adsorption shows that considerable adsorption (greater than 10 Au NCs, black dashed line) occurs at approximately 20% THF for 20 nm Au NCs, while the threshold for considerable 40 nm Au NC adsorption is between 20% and 30% THF. The threshold for 5 nm Au NC adsorption is determined manually because image analysis cannot discern contrast from small Au NCs. Scale bars are 200 nm.

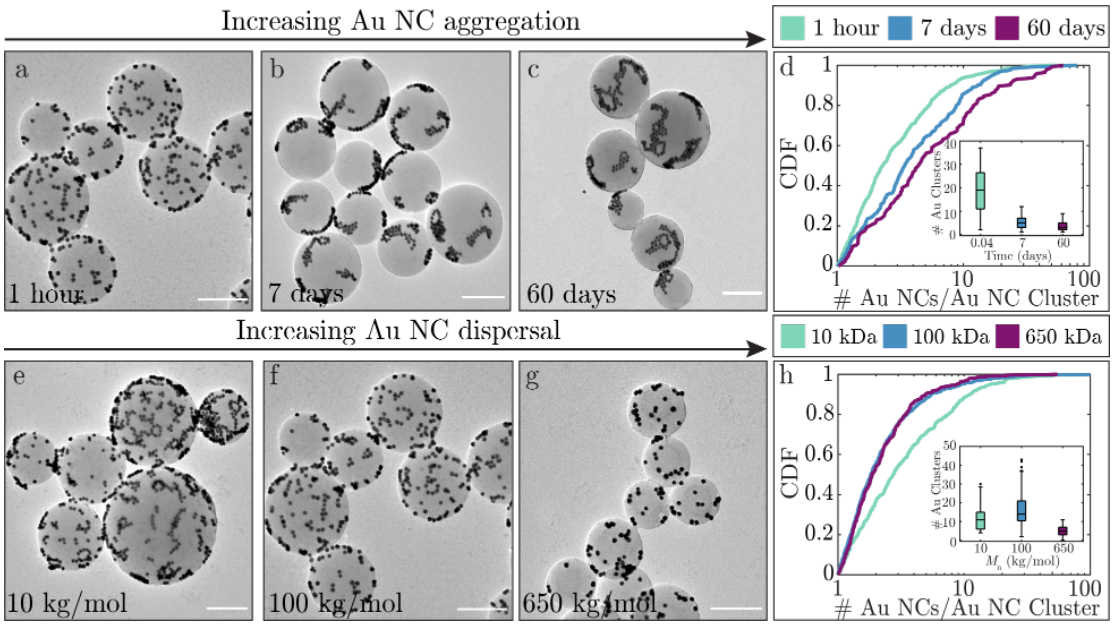


Figure 6.5: The diffusion timescale of PS chains impacts Au NC dispersal. (a) Hybrid nanoparticles fabricated with 100 kg/mol PS and incubated with Au NCs for 1 hour, (b) 7 days, and (c) 60 days reveal a transition from disperse to aggregated surface decoration. (d) Cumulative distribution function (CDF) of Au NC cluster sizes over time. The CDF indicates a shift from smaller to larger cluster sizes as time increases. Inset shows a box and whisker plot of the number of clusters per PS particle over time. As the size of clusters increases, the number of clusters decreases. (e) hNPs fabricated with 10 kg/mol PS, (f) 100 kg/mol PS, and (g) 650 kg/mol PS at a constant incubation time of 1 h indicate increasing dispersal due to longer diffusion timescales as molecular weight increases. (h) CDF of Au NC cluster sizes with varying molecular weight indicates that hNPs with low molecular weight PS exhibit greater surface aggregation. Inset shows a box and whisker plot of the number of clusters per PS particle with varying molecular weight. All scale bars are 200 nm.

However, longer incubation times with excess Au NCs do not result in greater adsorption, but rather, in greater Au NC aggregation atop PS NPs. Increasing incubation time from 1 hour to 7 days causes a 15% reduction in the population of clusters $\leq$ 2 Au NCs. This observation indicates that at intermediate incubation times between 1 and 7 days, Au NCs begin to diffuse across the surfaces of PS NPs, aggregating to increase the population of intermediate-sized clusters (Fig. 6.5b). As incubation time increases by another order of magnitude to 60 days, we observe the presence of even larger clusters (Fig. 6.5c). Between 1 hour and 60 days, the population of large clusters increases by over 20% (Fig. 6.5d), while the average number of Au NCs adsorbed per PS NP for long incubation times remains constant (Fig. 6.6), suggesting that by the 60-day point, aggregation occurs *via* coalescence of larger clusters, rather than by the motion of individual Au NCs.

This shift toward larger clusters as incubation time increases is further supported by quantification of the number of Au NC clusters on each PS NP. The inset of Fig. 6.5d shows a decrease in the median number of clusters per PS NP from 19 clusters after a 1-hour incubation, to 5 clusters after 7 days, and 3 clusters after 60 days. We hypothesize that the initial stark decrease in the number of clusters between 1 hour and 7 days occurs due to diffusion of numerous small clusters. However, once aggregates became larger, their diffusive motion becomes sluggish. While they are still able to coalesce into larger aggregates, the rate of such fusion events is reduced drastically due to both the longer diffusion times necessitated by the larger average cluster size as well as the more limited number of possible interactions due to the presence of fewer clusters.

The strong dependence of both Au NC cluster size and total number of Au NC clusters on incubation time suggests that Brownian diffusion of Au NCs is strongly influenced by the

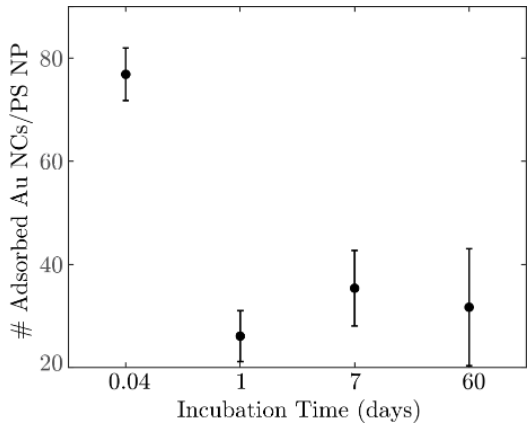


Figure 6.6: Average number of adsorbed Au NCs per 100 kg/mol PS NP. The number of Au NCs adsorbed per PS NP after 1 hour is larger than the number of Au NCs adsorbed per PS NP for all other incubation periods. However, after 1 day of incubation, the average number of Au NCs per PS NP remains approximately constant, supporting that the formation of large aggregates for longer incubation times is a result of cluster coalescence and not additional Au NC adsorption over time.

viscosity of PS NPs. To further probe this hypothesis, we alter PS NP viscosity by varying the PS molecular weight employed in the FNP solvent stream. We fabricate PS NPs using each molecular weight (M_n = 10, 100, and 650 kg/mol) and incubate them with Au NCs for 1 hour. PS NPs fabricated from 10 kg/mol PS exhibit strong aggregation, in which Au NCs formed 2D worm- and ring-like structures on PS NP surfaces (Fig. 6.5e). However, as molecular weight increases, formation of large aggregates on PS NP surfaces is suppressed, giving rise to disperse surface decoration of Au NCs on PS NP surfaces (Fig. 6.5f, g). We again quantify aggregation *via* an analysis of Au NC cluster sizes (Fig. 6.5h). When we assess the cumulative distribution function (CDF) of Au NC clusters on the surfaces of 10, 100, and 650 kg/mol PS NPs, we find that hNPs fabricated with 10 kg/mol PS exhibit 20% more Au NC clusters $>$ 2 Au NCs in size than their higher M_n counterparts, consistent with our observations.

Finally, to describe the transition from aggregated to disperse surface decoration that we

observe with increasing molecular weight, we use a simple scaling argument to compare the viscosities of the PS NPs themselves by approximating each nanoparticle as a polymer melt. Despite our hypothesis that residual THF penetrates some distance into PS NPs[245], we make this approximation because the polymer chains within PS NPs are collapsed into dense aggregates during FNP, with polymer volume fractions, x, of at least 0.58 in the precipitated 10 kg/mol particles, much greater than its respective overlap concentration, reported as a volume fraction, x^* of approximately 0.02[246,247]. For PS with a molecular weight below the entanglement molecular weight ($M_e = 17$ kg/mol) the viscosity scales as $\eta_{PS} \sim N$, where N is the number of monomers within the polymer chain. For PS with a molecular weight that exceeds M_e, $\eta_{PS} \sim \frac{N^3}{N_e^2}$, where $N_e = \frac{M_e}{m_0}$ and m_0 is the molecular weight of the PS monomer[248]. Thus, we find that $\frac{\eta_{100\,\mathrm{kDa}}}{\eta_{10\,\mathrm{kDa}}} \sim \mathcal{O}(100)$, while $\frac{\eta_{650\,\mathrm{kDa}}}{\eta_{10\,\mathrm{kDa}}} \sim \mathcal{O}(10^5)$.

This scaling provides a rationale for the Au NC aggregation observed in Fig. 6.5. For example, following the viscosity ratio, $\frac{\eta_{100\,\mathrm{kDa}}}{\eta_{10\,\mathrm{kDa}}}$, we would expect Au NCs to become aggregated atop 100 kg/mol PS at timescales 100 times longer than 10 kg/mol PS. Indeed, when we compared the morphology of 100 kg/mol hNPs at incubation times 100 times longer than 10 kg/mol hNPs, we see similar extents of aggregation when we compare Fig. 6.5b and Fig. 6.5e. Furthermore, following the viscosity ratio, $\frac{\eta_{650\,\mathrm{kDa}}}{\eta_{10\,\mathrm{kDa}}}$, we do not expect to see comparable morphologies to 10 kg/mol hNPs until timescales $\mathcal{O}(10^5$ hours) longer (Fig. 6.7).

While this scaling argument helps to link qualitative similarities in Au NC configurations atop PS NPs obtained by either changing molecular weight or incubation time, we still observe a difference in the trends between the number of Au NC clusters observed per PS NP over time versus molecular weight (insets to Fig. 6.5d, h). When we vary PS molecular weight, the number of clusters per PS NP increases between 10 kg/mol and 100 kg/mol, consistent

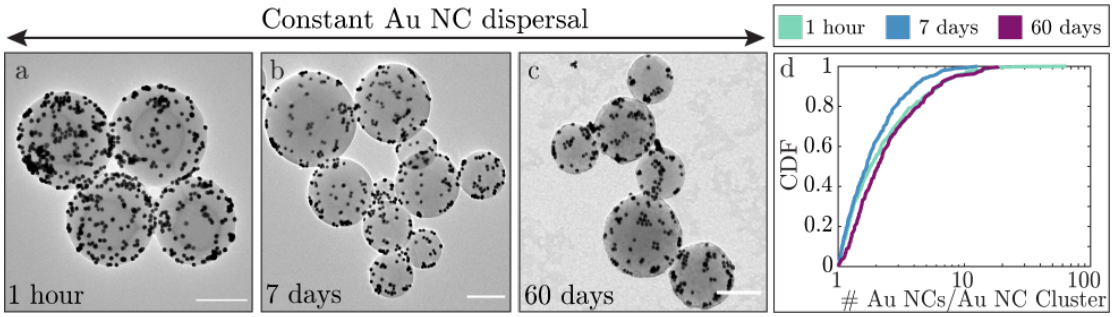


Figure 6.7: Morphologies of 650 kg/mol hybrid nanoparticles remain disperse over long times. Morphologies of hNPs fabricated with 650 kg/mol PS and incubated with Au NCs for (a) 1 hour, (b) 7 days, and (c) 60 days remain qualitatively constant. (d) Cumulative distribution function (CDF) reveals that cluster sizes remain relatively constant over 10^3 hours, which is supported by our scaling argument, which suggests that aggregation would not occur until timescales approaching 10^5 hours.

with the inset to Fig. 6.5d, but we see a sudden decrease in the number of clusters per PS NP at 650 kg/mol (inset to Fig. 6.5h). We attribute this discrepancy to our experimental method, in which we hold the inlet mass of PS during FNP constant and the volume ratio of PS NPs to Au NCs constant during incubation. Using a constant inlet mass of PS does not necessarily correspond to constant PS NP size, particularly at higher M_n. The smaller PS NP size obtained from 650 kg/mol PS ($d = 113$ nm ± 11 nm) versus those obtained from 10 kg/mol ($d = 302$ nm ± 17 nm) or 100 kg/mol ($d = 300$ nm ± 12 nm) implies that a greater number of small PS NPs are incubated with Au NCs. Thus, the PS NP surface area to Au NC mass ratio increases due to the increased surface area of 650 kg/mol PS NPs, and a smaller number of Au NCs adsorb to each PS NP as a result.

Despite the lack of attractive interactions between PS NPs and citrate-stabilized Au NCs, we observe the formation of hNPs whose surface decoration characteristics are sensitive to diffusion. We hypothesize that by adding amine-terminated polystyrene (PS-NH_2) to the FNP solvent stream, stronger interactions between the positive end-groups of PS-NH_2 and negatively charged citrate-stabilized Au NCs would hinder diffusive motion of Au NCs, promoting the presence of more disperse Au NCs atop PS NPs.

We employ PS with a molecular weight $M_n = 10$ kg/mol to assess the effect of electrostatic interactions on Au NC mobility atop PS NPs. Typically, complete aggregation occurs on hNPs made from PS with $M_n = 10$ kg/mol within a 24-hour incubation period (Fig. 6.8), so we analyze Au NC dispersal for a range of PS-NH_2 concentrations after 24 hours of incubation to assess the ability of electrostatic interactions to stabilize disperse Au NCs atop PS NPs. For comparison, we show the hNP morphology produced from 10 kg/mol PS (0% PS-NH_2) after 24 hours of incubation with Au NCs (Fig. 6.9a), which exhibits almost complete aggregation, or the formation of a single, large Au aggregate per PS NP (Fig. 6.9d and inset).

By varying PS-NH_2 concentrations from 0% to 50%, we detect two distinct morphological regimes that arise due to the presence of charged end groups, which we term "dispersal" (Fig. 6.9) and "internalization" (Fig. 6.10). We first explore the "dispersal" regime, within which we see the suppression of Au NC aggregation on the surfaces of PS NPs. When PS NPs are fabricated from 3 vol% PS-NH_2, we still see ring-like aggregates similar to those that we see in the absence of PS-NH_2 (Fig. 6.9b), but we also begin to see a much larger presence of

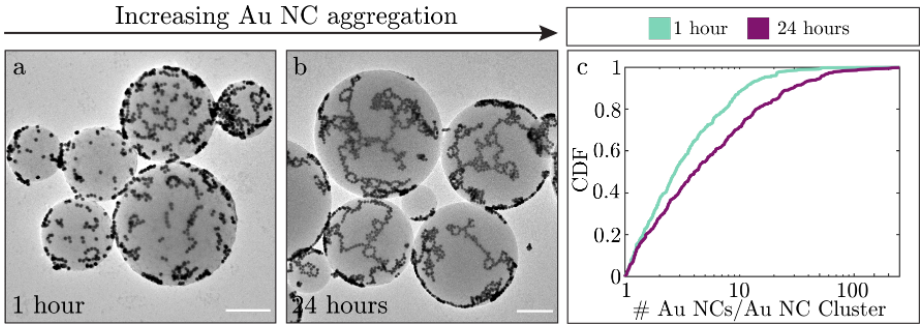


Figure 6.8: Distributions of cluster sizes on surfaces of 10 kg/mol PS NPs are similar over 24 hours. (a) Image of Au NC adsorption to 10 kg/mol PS NPs after 1 h incubation. (b) Image of Au NC adsorption to 10 kg/mol PS NPs after 24 h incubation. (c) Cumulative distribution function (CDF) of Au NC cluster sizes shows a clear shift in the distribution of cluster sizes within 24 h from smaller to larger clusters, as indicated by the gap between the green and purple lines. These data suggest that gold clusters atop 10 kg/mol hNPs approach complete aggregation over much faster timescales than their high molecular weight counterparts. Scale bars are 200 nm.

disperse, single Au NCs, as indicated by the difference between the CDFs for 0% PS-NH_2 and 3% PS-NH_2 (Fig. 6.9d). As the concentration of PS-NH_2 increases to 5%, we observe a 45% increase in the population of Au NC clusters $<$ 2 Au NCs and a concomitant 20% decrease in the population of Au NC clusters $>$ 10 Au NCs, indicating that Au NCs shift toward nearly complete surface dispersal (Fig. 6.9d).

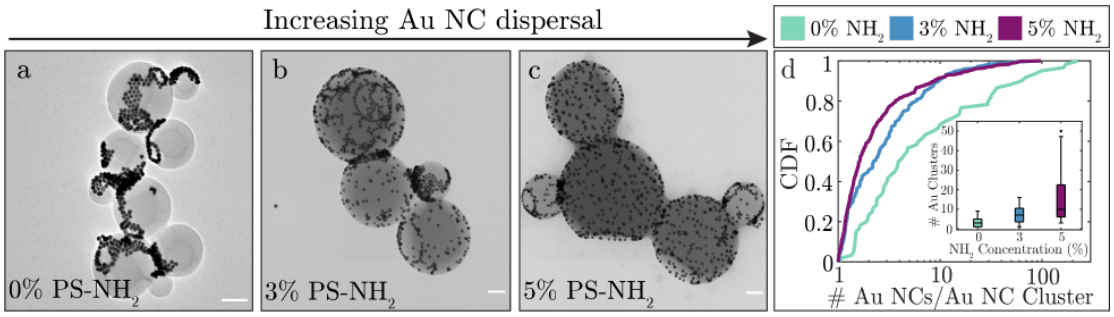


Figure 6.9: Low PS-NH_2 concentrations promote Au NC dispersal. Hybrid NPs fabricated with (a) 0%, (b) 3%, and (c) 5% 10 kg/mol PS-NH_2 reveal enhanced dispersal as PS-NH_2 content increases. (d) CDF of Au NC cluster sizes reveals a trend toward more disperse Au NCs on the surfaces of PS NPs with increasing NH_2 content. Inset shows that the number of clusters per PS NP increases concomitantly. All scale bars are 100 nm.

The approach to complete dispersal at 5% PS-NH_2 is also supported by our analysis of

the total number of clusters per PS NP. Here, we see that the distribution in the number of clusters becomes much wider at 5% PS-NH_2 than it is at 3% PS-NH_2 (inset to Fig. 6.9d). This stark difference in number of clusters per PS particle supports our observation that the diffusive process that forms mid-sized worm- and ring-like structures gives rise to smaller Au NC aggregates or single Au NCs. This nuance is further supported by the shift in the CDFs of 3% and 5% PS-NH_2 morphologies. While the entire distribution shifts toward smaller clusters between 0% and 3% PS-NH_2, between 3% and 5%, the majority of this shift occurs only in the population of mid-size clusters because worm- and ring-like structures begin to disappear.

When the PS-NH_2 volume percentage increases to 10%, we observed that Au NCs begin to embed themselves beneath the surfaces of PS NPs in a process we term "internalization" (Fig. 6.10a). While Au NCs are just beneath the surfaces of PS NPs at 10% PS-NH_2, for PS-NH_2 concentrations greater than 10%, Au NPs become completely immersed. Previous work using a two-polymer blend in the FNP process shows that when the interfacial tension, $\gamma_{polymer1-water} < \gamma_{polymer2-water}$, the resulting colloids exhibit a core-shell morphology in water.[76] Thus, because PS-NH_2 is more hydrophilic than PS ($\gamma_{PS-NH_2-water} < \gamma_{PS-water}$), it should form a core-shell structure with PS-NH_2 as the shell.

However, when PS/PS-NH_2 NPs are incubated with citrate-stabilized Au NCs, we must also consider the charge neutralization effects that occur when NH_3^+ and COO^- groups interact. We can explore the impact of the interactions between NH_3^+ and COO^- groups by quantifying the charge ratio, or the molar ratio of NH_3^+ to COO^- groups present during incubation. For example, the surfaces of hybrid NPs made with 10% PS-NH_2 become saturated with Au NCs because the charge ratio is $\ll 1$ (Fig. 6.10a). As a result, we expect that

all Au/PS-NH_2 complexes are free to exist at or close to the surface because there is NH_3^+ in excess of COO^-. Our 2D analysis of TEM images confirm this expectation (Fig. 6.10d), and also suggests that the Au/PS-NH_2 complex is still less hydrophobic than PS.

As PS-NH_2 content increases, the shell it forms becomes thicker and the NH_3^+ to COO^- charge ratio eventually exceeds 1, at a calculated crossover concentration of approximately 21% (Table 6.1). To estimate this crossover concentration, first need to calculate the concentration of NH_2 groups for hNPs produced with varying percentages of PS-NH_2. Given a total inlet concentration of 0.1 mg/mL of PS and PS-NH_2 in the FNP process, the corresponding concentrations of PS-NH_2 are calculated in Table 6.1.

PS-NH_2 (vol %)	Concentration (μmol/mL)	Molar Ratio
0	0	0
5	0.31	0.24
10	0.63	0.48
25	1.56	1.20
50	3.12	2.02

Table 6.1: Calculation of NH_2 to COOH Molar Ratio. Calculation of NH_2 to COOH Molar Ratio. The first step in calculating the crossover concentration, or the concentration at which the number of citrate groups exceeds the number of amine groups on the surfaces of hNPs, is to convert the PS-NH_2 volume percentage used during FNP to a concentration in μmol/mL. Next, with a constant concentration of 2.6 μmol/mL of citrate groups, we calculate the molar ratio of NH_2 to citrate groups using the obtained PS-NH_2 concentrations. The transition from [PS-NH_2]/[COOH] < 1 to [PS-NH_2]/[COOH] > 1 occurs between an PS-NH_2 concentration of 10% and 25%.

Next, we calculate the number of moles of COOH groups for the Au NC suspension, based on fabrication conditions, in which 100 mg sodium citrate is added to approximately 205 mL of water. In the final Au NC suspension, the concentration of citrate groups is approximately 2.6 μmol/mL. In our experiments, we mix PS NP suspensions at a 2:1 ratio with the Au NC suspension, so we calculate the final molar ratio of NH_2 groups to citrate groups for each concentration. When the molar ratio of NH_2 groups to citrate groups exceeds 1, we

expect internalization to occur, which occurs at an FNP inlet concentration of 21% PS-NH_2.

In experiments, we begin to see the predicted internalization of Au NCs above 21% PS-NH_2 (Fig. 6.10b, c). When the charge ratio eventually exceeds 1, there is free PS-NH_2 available to exist at the surface of hNPs, which we hypothesize is energetically favorable because $\gamma_{PS-water} > \gamma_{PS-NH_2/Au-water} > \gamma_{PS-NH_2-water}$, and can be seen clearly by the presence of an Au NC-free ring on the outside of 50% PS-NH_2 NPs (Fig. 6.10c). Because the charge ratio is $\gg 1$ in this case, compatibilization of Au NCs within PS via hydrophobic ion pairing enables their miscibility and is therefore also energetically favorable[249,250]. Thus, both enhanced surface wetting and miscibility act as energetic driving forces in the formation of these internalized hNPs. Our observations are further supported by the CDF of Au NC depth within PS, which shows that $> 80\%$ of hybrid NPs fabricated with 50% PS-NH_2 contain only internalized Au NCs (Fig. 6.10d).

Having quantified Au NC internalization from two-dimensional (2D) images, we also perform TEM tomography to confirm the three-dimensional (3D) structure of the hNPs. TEM images of three isolated hNPs containing 10%, 25%, and 50% PS-NH_2 are acquired at tilts ranging from $-60°$ to $+60°$. Three-dimensional tomographic reconstructions from these tilted images map the spatial distribution of Au NCs within these hNPs (Fig. 6.10e-g), showing good qualitative agreement with the Au NC placement estimated from 2D TEM images (Fig. 6.10a-c).

From these 3D reconstructions, we also quantify the radial density distribution of Au NCs embedded within PS NPs (Fig. 6.10h). Consistent with our CDFs of the approximate radial depth of Au NCs for many hNPs, 3D tomography shows that the peak density of Au NCs within PS NPs shifts deeper into PS particles with increasing PS-NH_2 content and therefore

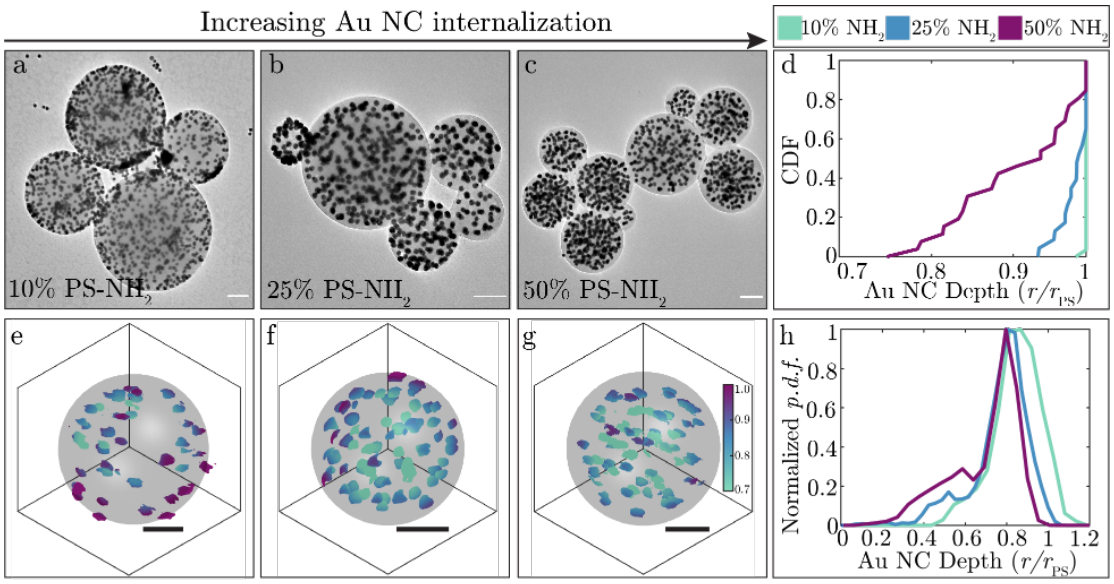


Figure 6.10: Au NCs become internalized above a threshold concentration of PS-NH_2. Hybrid NPs fabricated from 10 kg/mol PS with (a) 10%, (b) 25%, and (c) 50% 10 kg/mol PS-NH_2 reveal increasing degrees of internalization as PS-NH_2 content increases. (d) CDF of Au NC depth within PS NPs obtained from 2D images reveals that as PS-NH_2 content increases above 10%, Au NCs penetrate deeper into PS NPs. Three-dimensional (3D) tomographic reconstructions of Au NC locations within PS NPs containing (e) 10%, (f) 25%, and (g) 50% PS-NH_2 content shows increasing depth of internalization as PS-NH_2 content increases. The color scale corresponds to the depth within the PS NP that Au NCs are located, normalized to the radius of the PS NP. (h) Normalized radial density distribution plot of Au NCs within PS NPs. As PS-NH_2 content increases, the peak density shifts toward further internalization and a population of internalized Au NCs develops. Scale bars in (a), (b), and (c) are 100 nm. Scale bars in (e), (f), and (g) are 50 nm.

increasing charge ratio. At 10% PS-NH_2, several Au NCs reside on the outside of the PS NP with most just under the surface. TEM tomography also reveals that as the PS-NH_2 content increased to 25% and 50%, a substantial population of Au NCs becomes internalized to normalized radii less than 0.5. While the PS-NH_2 shell increases in thickness as PS-NH_2 content increases, it is also possible that some PS-NH_2 becomes entrained within the PS core at the highest concentration, 50%. As a result of this potential entrainment, some Au NCs became trapped deep within PS NPs.

6.5 Tuning catalytic reactions using hybrid nanoparticles

Having explored a wide parameter space to understand the emergence of aggregated, dispersed, and internalized Au NC localization atop and within PS NPs, we next test the ability of hNPs with internalized Au NCs to carry out a catalytic reduction of 4-nitrophenol to 4-aminophenol (Fig. 6.11a). We add equal volumes —and therefore approximately equal concentrations—of hNPs that are washed and concentrated *via* centrifugation with PS-NH_2 concentrations of 10%, 25%, and 50% to a reaction mixture containing 0.1 mM 4-nitrophenol and 0.067 M sodium borohydride ($NaBH_4$).

For each PS-NH_2 concentration, we measure UV-Vis absorbance spectra as a function of time over a range of wavelengths, λ, from 250 nm to 500 nm every 5 minutes for 2 hours. For the reaction that employs 10% PS-NH_2 hNPs, we see a strong peak at the primary absorbance for 4-nitrophenol ($\lambda_{abs} = 405$ nm) at time $t = 0$ min. This peak decreases in magnitude exponentially as a small peak at the primary absorbance for 4-aminophenol ($\lambda_{abs} = 294$ nm)

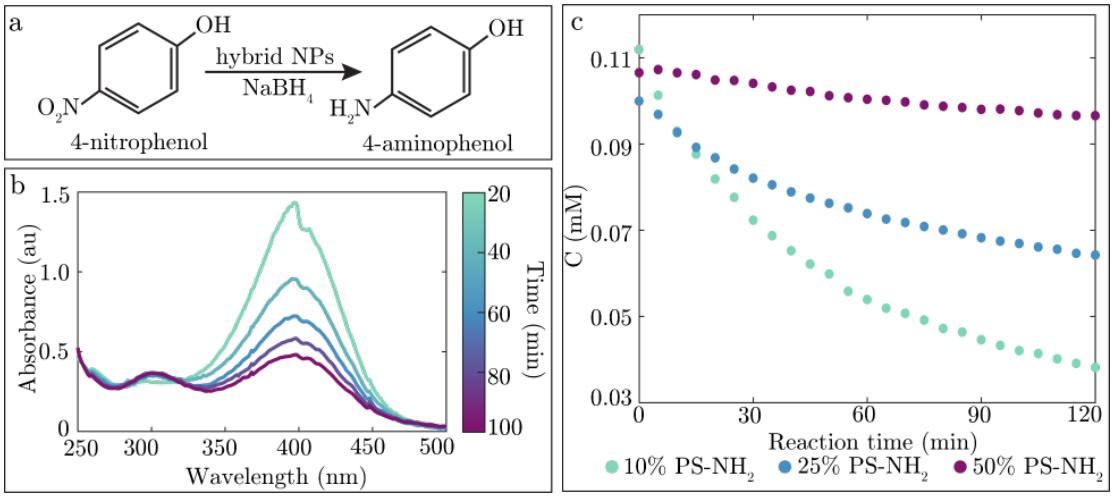


Figure 6.11: Hybrid nanoparticle morphology controls the reaction rate of a model reduction reaction. (a) Reaction scheme to produce 4-aminophenol from 4-nitrophenol is catalyzed by Au NCs. We add 100 µL of an hNP suspension to a reaction mixture containing 0.1 mM 4-nitrophenol and 0.067 M $NaBH_4$. (b) Example UV-Vis spectrum of reduction over time using 10% PS-NH_2 hNPs shows a decrease in the magnitude of the primary absorbance of 4-nitrophenol ($\lambda_{abs} = 405$ nm) and an increase in that of 4-aminophenol ($\lambda_{abs} = 294$ nm). (c) Plot of concentration (C) measured at $\lambda = 405$ nm every 5 min for 2 h demonstrates that increasing internalization slows reaction rate and efficacy.

begins to emerge (Fig. 6.11b). We run additional reduction reactions using 25% and 50% PS-NH_2 hNPs to show the reduction in 4-nitrophenol concentration over time for each hNP formulation (Fig. 6.11c). The reduction of 4-nitrophenol to 4-aminophenol is a first order reaction, $C(t) = C_0 \exp(-kt)$, where $C(t)$ is the concentration of 4-nitrophenol over time, C_0 is the initial 4-nitrophenol concentration, k is the first-order reaction rate constant, and t is time[241]. We obtain rate constants $k = 6 \times 10^{-5}$ 1/s, 2×10^{-5} 1/s, and 7×10^{-6} 1/s, for 10%, 25%, and 50% PS-NH_2 hNPs, respectively. These rate constants indicate that reactions using 25% PS-NH_2 hNPs proceed 3 times slower than those produced using 10% PS-NH_2, while reactions using 50% PS-NH_2 hNPs proceed 10 times more slowly. While a small amount of PS-NH_2 improves Au NC dispersal atop PS NPs, excess PS-NH_2 hinders the rate of reaction. Importantly, the evolution of these reactions reveals that hNPs can be fabricated such that

their reaction rates are correlated to the position of Au NCs within hybrid NPs. Additionally, the method of hNP formation presented here may be used to produce materials with varying catalytic properties.

6.6 Conclusions

Widespread deployment of novel nanomaterials for *in situ* remediation of groundwater contaminants has long been precluded by their inability to remain stable against aggregation. Additionally, complex fabrication techniques are often required to produce hybrid materials with tunable morphologies and reaction rates. The work presented in this chapter introduced a simple method to fabricate hNPs that relies only on the presence of a good solvent for the polymer to allow for gold nanocatalyst adsorption. Using this method, we showed that increasing incubation time allows for enhanced aggregation of gold nanocatalysts on polystyrene nanoparticle surfaces, while increasing polymer molecular weight increases their dispersal. We also demonstrated that electrostatic interactions could be used to overcome gold aggregation and promote surface dispersal or internalization of gold nanocatalysts. Since electrostatic interactions only occurred between the polymer end-group and nanocatalyst stabilizer, we expect that catalytic reaction rates can be tuned for various citrate-stabilized nanocatalysts, such as platinum or bimetallic nanoparticles, thus making this approach applicable for a wide range of catalytic reduction reactions. Taken together, these results shed light on an approach by which hNPs can be fabricated with tunable morphologies and reveal mechanisms by which catalytic reaction rates can be controlled.

6.7 Supplementary Information

Zeta potential measurements for PS NPs. We measure zeta potential of PS and PS/PS-NH_2 NPs by diluting NPs in 0.1 mM KCl using an Anton Paar Litesizer 500. PS NPs with no PS-NH_2 and $M_n = 10$ kg/mol have a measured zeta potential $\zeta = -35.5 \pm 1.2$ mV, while those with $M_n = 99$ kg/mol have $\zeta = -35.7 \pm 1.0$ mV and those with $M_n = 646$ kg/mol have $\zeta = -18.6 \pm 1.0$ mV. As we increase PS-NH_2 content from 5% to 10%, 25%, and 50%, we record $\zeta = -34.4 \pm 0.9$ mV, -30.6 ± 1.0 mV, -32.1 ± 0.5 mV, and -8.7 ± 0.9 mV, respectively.

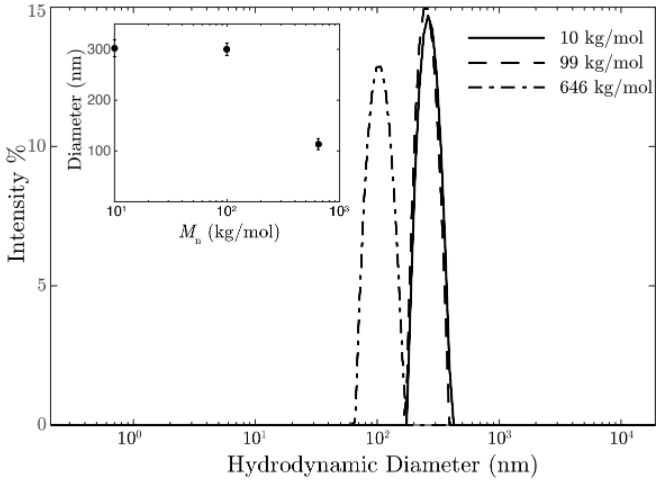


Figure 6.12: Hydrodynamic diameter measurements of PS NPs with varying molecular weights, M_n. Dynamic light scattering (DLS) plot of 10 kg/mol, 99 kg/mol, and 646 kg/mol polystyrene nanoparticles. Inset shows average hydrodynamic diameter with standard deviation for each molecular weight, $d = 302 \pm 17$ nm, $d = 300 \pm 12$ nm, and $d = 113 \pm 11$ nm in order of increasing molecular weight.

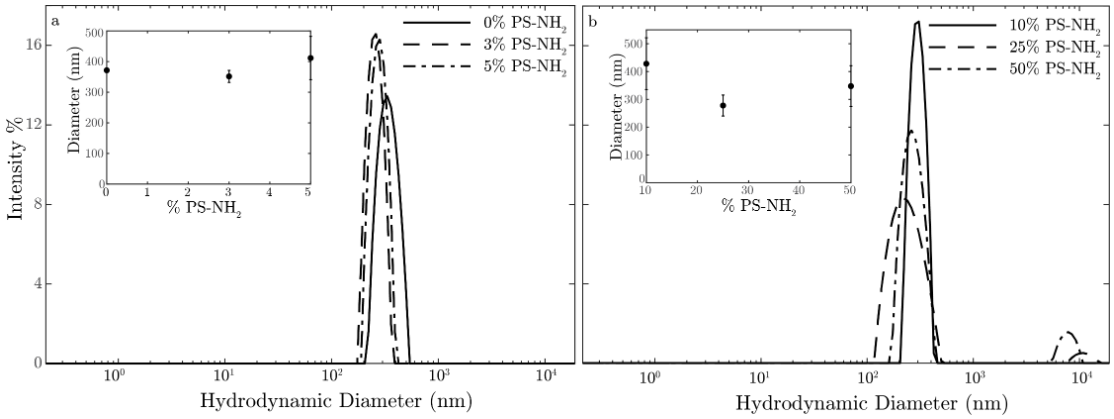


Figure 6.13: Hydrodynamic diameter measurements of PS-NH_2 NPs. (a) Dynamic light scattering (DLS) plot of surface-decorated 0%, 3%, and 5% PS/PS-NH_2 nanoparticles. Inset shows average hydrodynamic diameter with standard deviation for each formulation, $d = 371 \pm 6$ nm, $d = 351 \pm 20$ nm, and $d = 411 \pm 71$ nm in order of increasing PS-NH_2 content. (b) Dynamic light scattering (DLS) plot of internalized 10%, 25%, and 50% PS/PS-NH_2 nanoparticles. Inset shows average hydrodynamic diameter with standard deviation for each formulation, $d = 428 \pm 93$ nm, $d = 278 \pm 38$ nm, and $d = 348 \pm 73$ nm in order of increasing PS-NH_2 content.

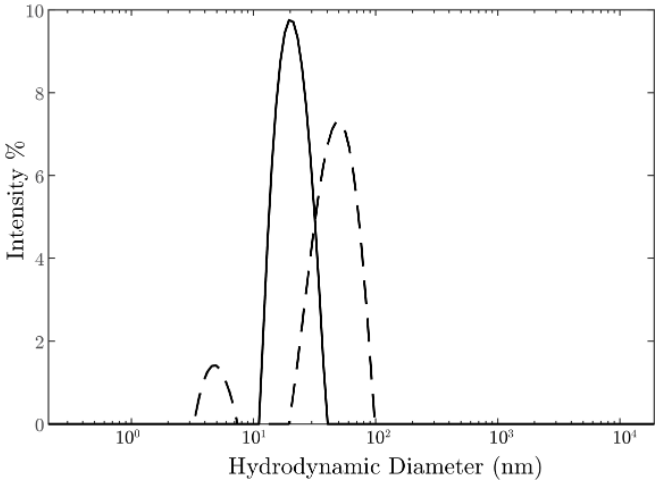


Figure 6.14: Hydrodynamic diameter measurements of citrate-stabilized Au NCs. Dynamic light scattering (DLS) plot of Au NCs produced with 0.4 wt% and 2 wt% sodium citrate, which have $d = 38.0 \pm 10$ nm and $d = 20.9 \pm 2$ nm, respectively.

Without experimentation,
a willingness to ask questions and try new things,
we shall surely become static, repetitive, and moribund.

Anthony Bourdain

7

Outlook and future directions

In this dissertation, we have thoroughly explored several ways in which immiscible fluids and colloids can interact, revealing how the interplay between these two phases impacts their flow behavior within a porous medium. Factors including flow conditions and the extent of colloidal deposition are of critical importance in understanding and predicting

these interactions. For example, when immiscible fluid flow and subsequent trapping occur *before* introduction of colloidal particles into the porous medium, we find that they can be deposited to enhance removal of trapped immiscible fluid droplets by squeezing them out. Conversely, when flow of an immiscible fluid occurs *after* colloidal deposition, deposited particles can be removed from solid surfaces by the immiscible fluid. In Chapters 4 and 5, we found that the extent of deposition alters the complexity of this capillarity-induced erosion and redeposition and may even change the rheology of fluid-fluid interfaces. In Chapter 6, we developed a systematic method of fabricating hybrid colloidal particles motivated by our understanding of how these particles flow and deposit in a porous medium, with the hope that we can explore how they may remove contaminants *in situ*.

It is clear that a complex array of behaviors emerges only when immiscible fluids and colloidal particles exist together. Though an outsider may think this an infrequent occurrence, interactions between colloids and immiscible fluids govern countless everyday processes, from something as simple as the emulsification of mayonnaise to more complex processes like wetting and drying cycles in soils, which have crucial impacts on crop retention and viability. The work presented in this dissertation has inspired countless additional questions; in this chapter, I highlight two of my most pressing remaining questions that build upon the work presented in previous chapters. First, how does dense, multilayer colloidal deposition impact immiscible fluid flow in 3D porous media? Second, how does reactivity of catalytically active colloidal particles compete with physical mechanisms of immiscible fluid removal?

This chapter is based on ongoing unpublished work by Joanna Schneider and Sujit S. Datta. **Author Contributions:** J.S. and S.S.D. designed the experiments; J.S. performed preliminary experiments and analysis. S.S.D. designed and supervised the overall project.

7.1 Immiscible fluid-enhanced erosion in 3D porous media

In Chapter 5, we explore the impacts of dense, multilayer deposition on macroscale immiscible fluid flow *via* simulations in a two-dimensional pore network model, while Chapter 4 explores a similar phenomenon experimentally at the pore scale. Both of these approaches provide key information about what drives flow-induced erosion and redeposition and the impacts of this pore scale process on macroscale flow behavior. However, both chapters present simplified approaches to studying this phenomenon. Building upon the knowledge presented in Chapters 5 and 4, we propose future work to explore these processes in 3D porous media. Thus far, to accomplish this goal, we have run preliminary experiments that explore he impacts of changing deposition and injection conditions. However, additional experiments that systematically change the extent of deposition and flow conditions must be performed to isolate the physical phenomena that give rise to new behavior in 3D media.

Impacts of dilute deposition on enhanced immiscible fluid mobilization. First, we explore an experimental setup in which a dilute concentration of colloidal particles is used to create a deposition profile along the length of the porous medium. Here, we flow a 8×10^{-3} vol% suspension of amine-terminated polystyrene particles with a diameter $d_p = 1$ μm through the porous medium at a flowrate $Q_w = 0.15$ mL/h. These flow conditions and suspension concentration result in the creation of a relatively uniform deposition profile along the length of the porous medium, as seen in Chapter 2. Next, we inject the non-wetting fluid at a fixed volumetric flow rate $Q_{nw} = 5$ mL/h, much larger than the flowrate used to create the desired deposition profile. Due to the high flow rate Q_{nw}, oil saturates the majority of

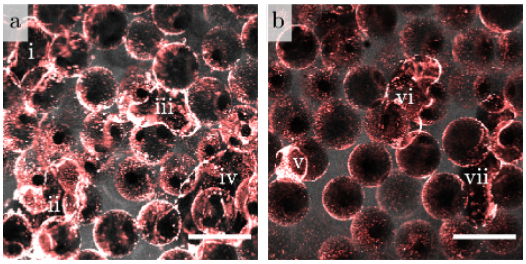


Figure 7.1: *In situ* Pickering emulsification of trapped oil droplets in a 3D porous medium. (a) and (b) show regions of a porous medium following secondary imbibition, in which a wetting fluid displaces a non-wetting fluid from a partially saturated porous medium. Here, the porous medium contains colloidal particles that can be eroded and redeposited by traveling immiscible fluid interfaces. Colloidal particles are shown in red, wetting fluid is shown in gray, and black circles show the cross-sections of spherical beads that comprise the porous medium. In these images, we observe adsorption of colloidal particles to trapped immiscible fluid droplets, resulting in a process we refer to as *in situ* Pickering emulsification. Each emulsified droplet is labeled (i) to (vii) from left to right to guide the eye. The scale bar in both images is 200 μm, and the flow direction is from left to right.

the pore space. Finally, we re-inject the wetting fluid without any colloidal particles at a high flowrate, $Q_w = 5$ mL/h, corresponding to a Capillary number, $\mathrm{Ca} = 1.3 \times 10^{-4}$, where the wetting fluid viscosity $\mu_w = 10.8$ mPa·s, the porous medium cross-sectional area $A = 9$ mm^2, and the interfacial tension between the two fluids $\gamma \approx 13$ mN/m.

Previous work using a similar experimental setup reports a precipitous drop in the maximum length of trapped oil droplets in the medium, L_{max}, and therefore the overall residual oil saturation, S_{OR} at $\mathrm{Ca} \approx 2 \times 10^{-4}$ [105], so we expect only small oil droplets with lengths $L \sim \mathcal{O}(1)$ bead diameter to remain trapped. While this is indeed what we observe in images following the final wetting fluid injection, we also observe that all of the trapped fluid droplets present are coated in colloidal particles (Fig. 7.1). From work presented in Chapters 5 and 4, we know that traveling immiscible fluid interfaces have the ability to adsorb colloidal particles *via* capillary forces. In these experiments, we hypothesize that adsorption occurs due to the same mechanism because amine-terminated polystyrene particles do not exhibit quiescent surface activity and there are no colloids present in suspension during secondary imbibition.

Thus, we refer to this process as *in situ* Pickering emulsification because oil droplets are stabilized by colloidal particles through a flow process within the porous medium.

Interestingly, this behavior contradicts an expectation about enhanced mobilization of immiscible fluid droplets. Specifically, localization of colloids at immiscible fluid interfaces is thought to significantly lower the interfacial tension between two fluids, resulting in a concomitant decrease in the value of L_{max}, whereby smaller droplets that could not be mobilized previously may be mobilized. Because droplets with lengths $L \sim \mathcal{O}(1)$ bead diameter in length remain trapped in the porous medium despite localization of colloidal particles at their interfaces, as shown in Fig. 7.1, we hypothesize that the interfacial tension reduction at these fluid interfaces is not sufficient to lower the predicted value of L_{max} substantially. One potential explanation is that interfacial tension reduction is small for amine-terminated polystyrene particles due to their lack of quiescent surface activity. Despite capillarity-induced adsorption to fluid interfaces present in the system, amine-terminated polystyrene particles exhibit a preference for the wetting fluid, resulting in a hypothesized three-phase contact angle at an oil-water interface, $\theta \ll 90^\circ$. As a result, the interfacial tension reduction achieved here is insufficient to enhance mobilization of small droplets that remain trapped at large Ca ($> 10^{-4}$).

Future experiments could examine this hypothesis by observing how changes in the wetting fluid Ca during secondary imbibition impact the preliminary results described above. For example, at lower Ca, small changes in interfacial tension could result in mobilization of additional ganglia because smaller differences in Ca are required for enhanced mobilization. However, larger ganglia require more particles for complete coverage, and therefore more effective *in situ* Pickering emulsification. This tradeoff between effective emulsification and Ca could be measured by comparing predicted and measured values of L_{max}, as demonstrated in

Chapter 2. Additional experiments could explore deposition of colloidal particles with various surface charges and chemical compositions to build upon this framework and assess how quiescent surface activity impacts the magnitude of interfacial tension reduction, and thus, overall improvement in enhanced mobilization.

Impacts of dense deposition on immiscible fluid flow. Next, we explore an experimental setup in which a denser concentration of colloidal particle is used to create a deposition profile along the length of the porous medium. In these experiments, we flow a 1.25×10^{-2} vol% suspension of amine-terminated polystyrene particles with a diameter $d_p = 1$ μm through the porous medium at a flowrate $Q_w = 0.2$ mL/h. These flow conditions and suspension concentration result in the production of a dense, localized deposition profile with significant clogging, as shown in Fig. 7.2a. Next, we inject a non-wetting fluid at a fixed volumetric flowrate $Q_{nw} = 0.8$ mL/h, corresponding to a Capillary number, $\text{Ca} = 2.9 \times 10^{-4}$, where the non-wetting fluid viscosity $\mu_{nw} = 16.8$ mPa·s, the porous medium cross-sectional area $A = 1$ mm^2, and the interfacial tension between the two fluids $\gamma \approx 13$ mN/m.

Here, instead of observing whether clogging helps or hinders mobilization of trapped immiscible fluid, we observe how colloidal deposition impacts immiscible fluid flow itself. We have previously explored this process, referred to as primary drainage, in Chapter 5. There, we show that immiscible fluids may explore more of the pore space due to the ability of fluid interfaces to rearrange deposited material as they flow. The experimental setup shown in Fig. 7.2 attempts to translate this work to 3D porous media, which may help to tailor 2D simulations to guide and predict 3D experiments. However, we have not considered the ability of the immiscible fluid to break through clogged pores, as shown in Fig. 7.2, in our 2D simulations. This phenomenon may in fact play an important role in determining immiscible fluid

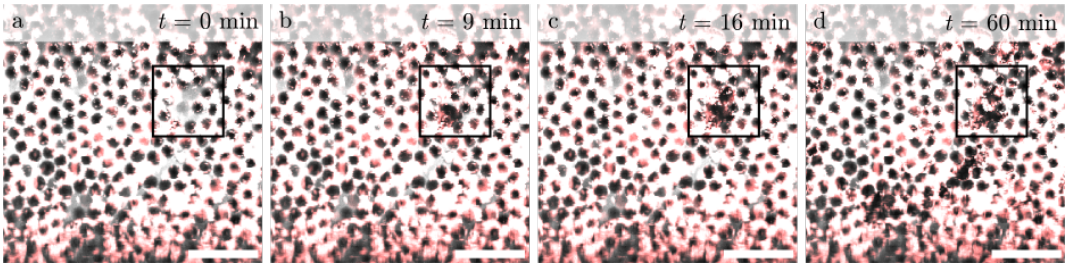


Figure 7.2: Immiscible fluid invasion during primary drainage deviates from typical Haines jumps. Magnified views of confocal micrographs showing an immiscible fluid invasion event (a) before, (b-c) during, and (d) after it breaks through a clogged pore with a critical yield stress, σ_y^*. Gray regions show pore space, black circles show the bead matrix, additional black regions show oil, and red shows dense colloidal deposits. (a) The pore space appearance immediately before the first invasion event ($t = 0$ min), which occurs in the black box, denoted in all panels. (b-c) The fluid breakthrough in the pore space occurs at several discrete times, including (b) $t = 9$ min and (c) $t = 16$ min, suggesting a strong pressure threshold to fluid invasion and potential pinning of the oil interface as it invades the pore. (d) Having invaded the pore highlighted by the black box, the fluid exhibits more traditional Haines jump-like invasion behavior as it percolates through the porous medium. The scale bar in all images is 250 μm, and the flow direction is from left to right.

flow behavior in the presence of densely deposited and clogged pores.

In this experiment, as the immiscible fluid is injected into the pore space at a constant flowrate, Q_{nw}, we do not see typical Haines jumps[251], which are fluid invasion events that occur when a non-wetting fluid passes from a small pore throat with a large capillary pressure into a larger pore body with a smaller capillary pressure. A recent study shows that Haines jumps typically occur on timescales $t \sim \mathcal{O}(10\text{ s})$ and cascade through 10 to 20 pores per Haines jump event[252]. Surprisingly, in our experiments, we see fluid invasion phenomena that exhibit different spatial and temporal characteristics than this seminal work. Fig. 7.2a shows the moment right before the first fluid invasion event ($t = 0$ min) in the porous medium. From Figs. 7.2a to 7.2b, we already see a deviation from traditional Haines jumps: it takes approximately 9 minutes for the immiscible fluid to invade the single pore highlighted in the black box, presenting a 50-fold difference in the amount of time required for the fluid to overcome the capillary pressure in a clogged pore throat versus a pristine one. This longer

invasion time suggests that there is an additional stress that the fluid must overcome in order to flow, which we call a critical yield stress, σ_y^*. We believe that this critical yield stress corresponds to a maximum colloidal deposit strength that an immiscible fluid must break through to percolate, or form a connected path, through the porous medium.

In addition to the temporal distinction from Haines jumps, we also observe that the number of pores through which the immiscible fluid travels during each invasion event is smaller. Specifically, between Figs. 7.2a and 7.2b, the immiscible fluid seems to only invade one pore before getting stuck at another clog. We observe similar behavior between Figs. 7.2b and 7.2c before the fluid breaks through another pore. In addition to the build-up of fluid pressure required to break through a deposit with σ_y^*, it is possible that additional complexities suppress typical Haines jump behavior. For example, densely deposited colloidal particles may alter the rheology of the fluid-fluid interface or pin the immiscible fluid to the solid grains of the porous medium. Further experiments are required to make generalizable statements about how clogging impacts the dynamics of Haines jumps, but this preliminary evidence suggests that immiscible fluids have the ability to break through clogged pores over extended periods of time, on the order of 10 times longer than a typical invasion event. It is not until after the fluid successfully breaks free of this clogged pore that we begin to see several larger fluid invasions more reminiscent of Haines jumps by time $t = 60$ min (Fig. 7.2d).

Another potential path for this work could incorporate the ability of an immiscible fluid to break through clogged pores into the modified invasion percolation framework presented in Chapter 5. This phenomenon could be implemented either by implementing some threshold time or characteristic pressure build-up required for breakthrough. Here, new data could determine how many of these pores must be broken through in order for the immiscible fluid

to percolate through the porous medium. Incorporating this complexity may also provide a more accurate estimate of the maximum density of clogged pores required to severely hinder or halt immiscible fluid flow. Furthermore, accounting for the occurrence of this phenomenon would generalize the results of Chapter 5 more broadly to real, 3D porous media.

7.2 Removal and degradation of trapped immiscible fluids

Having designed catalytically active hybrid nanoparticles (hNPs) with tunable morphologies in Chapter 6, another potential avenue for future work could test the ability of hNPs to degrade contaminants *in situ*, as proposed in Chapter 1. Given the multitude of physical interactions that can occur between colloids, immiscible fluids, and a porous medium, I hypothesize that there will be a trade-off between optimizing physical removal and chemical degradation of immiscible contaminants.

To test this hypothesis, it will first be necessary to make colloids fabricated *via* Flash NanoPrecipitation (FNP) visible using confocal microscopy. To accomplish this goal, a hybrophobic fluorophore must be added to the solvent stream during FNP to encapsulate it. Previous work shows the ability to encapsulate pyrene, anthracene, Nile red, and porphirine dyes within hydrophobic polymeric nanoparticles, spanning the visible light range from 370 to 720 nm[253]. Furthermore, because encapsulation happens during FNP, we do not anticipate this process to impact the surface decoration of hybrid nanoparticles with gold nanocatalysts.

Next, to test the ability of hybrid nanoparticles to degrade contaminants *in situ*, we propose two experimental setups to be probed: the first would introduce hybrid nanoparticles to

the porous medium following secondary imbibition to mimic a tertiary groundwater remediation step. From Chapter 2, we know that polystyrene nanoparticles stick to the grains of the porous medium matrix, squeezing some trapped droplets out of the medium *via* permeability reduction. However, the introduction of reactivity will address whether (i) traveling contaminants can be degraded as they navigate the pore space, and (ii) immobile contaminants make enough contact with reactive particles for sufficient degradation despite their inability to be removed. *Ex situ* testing in which the effluent is collected from the porous medium could probe the structure of model contaminants whose initial and reduced structures produce unique UV-Vis absorbance spectra. Specifically, effluent collected during experiments could test mobile contaminants' structures, while immobile contaminants could be removed following experiments to isolate differences in reduction rates and efficacy.

The second experimental setup to be probed would introduce hybrid nanoparticles to the pristine porous medium prior to primary drainage and secondary imbibition, as in the experiment described by Fig. 7.1. Here, we hypothesize that the ability of capillary forces to push hybrid nanoparticles onto fluid-fluid interfaces will improve their degradation efficiency due to prolonged contact between immiscible contaminants and hybrid nanoparticles. However, capillarity-induced adsorption may result in increased permeability in the porous medium and therefore decreased physical removal as deposited particles move from the porous medium to fluid interfaces. Future experiments could test how the extent of initial deposition impacts adsorption efficacy and track permeability changes in the porous medium over time to determine the initial deposition profile that optimizes both capillarity-induced adsorption for chemical degradation and permeability reduction for physical removal of trapped immiscible contaminants.

A

Relevant parameters

This appendix describes in more detail the relevant dimensionless quantities used in this dissertation and relevant ranges of these quantities in geological flows. Throughout this dissertation, we also assume that the minimum length of mobilized ganglia decreases as Ca increases. This appendix describes the rationale for this assumption and briefly touches upon situations where ganglia breakup would play a dominate role.

A.1 Key dimensionless quantities

In this dissertation, we develop representative model experiments by matching the key characteristics of aquifer flows in our experiments. Flows in groundwater aquifers are characterized by low ambient velocities which can be captured by the Reynolds number, $\mathrm{Re} \equiv \rho u L/\mu$. Re is a dimensionless quantity that describes the ratio of inertial to viscous forces where ρ is the fluid density, u is the wetting fluid superficial velocity in the porous medium and is equal to Q/A, μ is the fluid viscosity, and L is the characteristic length scale of the system—the pore throat diameter. Typical Re values in aquifers range from 10^{-11} to 10^{-3} [254]. Since $\mathrm{Re} \ll 1$ for these systems, flows in aquifers are laminar.

To understand the transport of nanoparticles in aquifers and develop processes that utilize them, it is important to characterize colloidal transport in porous, low Re aquifer environments. The particle Péclet number (Pe) can be used here to describe the ratio of advective to diffusive transport,

$$\mathrm{Pe} \equiv \frac{u}{\mathscr{D}/d_p} \tag{A.1}$$

where $\mathscr{D}$ is the Stokes-Einstein diffusivity of the particle and d_p is the particle diameter. Pe is particularly important for characterizing colloidal transport in groundwater aquifer flows because it is unclear whether diffusion-dominated or advection-dominated flow targets contaminants most effectively, and Pe may range anywhere from 10^{-6} to 10^{3} for different aquifers. If we consider the case where $\mathrm{Pe} \ll 1$, nanoparticles may find contaminants more effectively by diffusion, but the amount of time required for them to explore the pore space may exceed the amount of time over which they are stable. If we consider particles that deposit along the porous medium, low Pe may result in more uniform deposition of particles due

to diffusion, encouraging a permeability reduction that results in enhanced oil mobilization. However, if Pe $\gg$ 1, nanoparticles may explore more of the pore space, and therefore more of the contaminants, by advection. Alternatively, advection-dominated flow may result in colloidal transport along preferential pathways or flow redirection due to clogging. Further exploration of colloidal transport is necessary to determine which mechanisms play the most significant roles.

While Pe provides valuable information about colloidal transport, we must also capture the dynamics of immiscible fluid flow to understand and combat oil trapping in porous groundwater aquifers. Two important phenomena to consider are the invasion of oil into a saturated porous medium, as in contamination, and re-injection of water, as in EOR and remediation techniques. The mechanisms by which both of these processes occur are characterized by the capillary number, Ca. The capillary number describes the ratio of the viscous forces from flow to capillary forces due to interfacial tension between the wetting and non-wetting fluids at the pore scale,

$$\mathrm{Ca} \equiv \frac{\mu u}{\gamma} \tag{A.2}$$

where γ is the interfacial tension between the wetting and non-wetting fluids. Typical Ca values in aquifers range from approximately 10^{-10} to 10^{-4} because ambient flow velocities range from approximately 0.01 μm/s to 100 μm/s[254].

In both groundwater remediation and enhanced oil recovery (EOR) applications alike, there are many unanswered questions regarding how waterflooding-type processes can be controlled because the capillary forces present result in immiscible fluid trapping. One theory suggests that by increasing Ca (Eq. A.2), the viscous pressure drop across a trapped ganglion (Eq. 1.1) increases above the capillary pressure threshold that holds it in place and mobilizes

it[255–259]. Since the viscous pressure drop scales with length, the minimum length of mobilized ganglia decreases as Ca increases. Another theory suggests that as Ca increases, large ganglia break up into smaller ganglia, further increasing the required Ca to mobilize them[260–262].

An important distinction must be made between these two theories. Recent experimental studies show that the residual oil saturation, S_{OR}, decreases precipitously above a threshold Ca $\approx 2 \times 10^{-4}$ in homogeneous porous media[105]. In homogeneous porous media, the average pore throat size, a_t, is approximately $0.16a$, where a is the grain size, and the pore body size, $a_b \approx 0.24a$. Here, we define the pore body to pore throat size ratio, $a_t/a_b \approx 1.5$ for monodisperse sphere packs. However, in heterogeneous porous media, the range of this ratio changes, increasing the propensity for oil ganglia to break up due to a phenomenon called Roof snap-off[263]. The critical pore body to pore throat size ratio predicted for snap-off is 2 *via* a Rayleigh-Plateau instability. As ganglia get stretched into long, thin configurations to fill the pore space, it becomes favorable for them to break up to minimize the capillary forces exerted on them[142]. When this single long ganglion breaks up into two shorter ones, it increases the threshold Ca required to mobilize them because the viscous pressure drop across them decreases. Thus, while a threshold Ca is a good measure of mobilization for homogeneous media, as heterogeneities increase, oil ganglia break up, and increase the required threshold Ca, making mobilization hard to predict. In this dissertation, we only explore homogeneous porous media.

References

[1] Navid Bizmark, Joanna Schneider, Emily de Jong, and Sujit S. Datta. Chapter 9: Transport of Polymer Colloids in Porous Media. In *Polymer Colloids: Formation, Characterization and Applications*, pages 289–321. The Royal Society of Chemistry, 2020.

[2] Navid Bizmark, Joanna Schneider, Rodney D. Priestley, and Sujit S. Datta. Multiscale dynamics of colloidal deposition and erosion in porous media. *Science Advances*, 6 (46):eabc2530, 2020.

[3] Joanna Schneider, Rodney D. Priestley, and Sujit S. Datta. Using colloidal deposition to mobilize immiscible fluids from porous media. *Physical Review Fluids*, 6(1): 014001, 2021.

[4] Joanna Schneider, Christopher A Browne, Malcolm Slutzky, Cecilia A Quirk, Daniel B Amchin, and Sujit S Datta. Fluid drainage in erodible porous media. *arXiv preprint arXiv:2303.01260*, 2023.

[5] Joanna Schneider, Jason X. Liu, Victoria E. Lee, Robert K. Prud'homme, Sujit S. Datta, and Rodney D. Priestley. Tuning morphologies and reactivities of hybrid organic–inorganic nanoparticles. *ACS Nano*, 16(10):16133–16142, 2022.

[6] Christopher A. Browne, Daniel B. Amchin, Joanna Schneider, and Sujit S. Datta. Infection percolation: A dynamic network model of disease spreading. *Frontiers in Physics*, 9:645954, 2021.

[7] Barbara Karn, Todd Kuiken, and Martha Otto. Nanotechnology and in situ remediation: a review of the benefits and potential risks. *Environmental Health Perspectives*, 117(12):1813–1831, 2009.

[8] Douglas M. Mackay, Paul V. Roberts, and John A. Cherry. Transport of organic contaminants in groundwater. *Environmental Science & Technology*, 19(5):384–392, 1985.

[9] Changlin Huang and Alex S. Mayer. Pump-and-treat optimization using well locations and pumping rates as decision variables. *Water Resources Research*, 33(5):1001–1012, 1997.

[10] Daene C. McKinney and Min-Der Lin. Pump-and-treat ground-water remediation system optimization. *Journal of Water Resources Planning and Management*, 122(2): 128–136, 1996.

[11] Ling Li, Maohong Fan, Robert C. Brown, J. Van Leeuwen, Jianji Wang, Wenhua Wang, Yonghui Song, and Panyue Zhang. Synthesis, properties, and environmental applications of nanoscale iron-based materials: A review. *Critical Reviews in Environmental Science & Technology*, 36(5):405–431, 2006.

[12] Xiao-qin Li, Daniel W Elliott, and Wei-xian Zhang. Zero-valent iron nanoparticles for abatement of environmental pollutants: materials and engineering aspects. *Critical Reviews in Solid State and Materials Sciences*, 31(4):111–122, 2006.

[13] Sadott Pacheco, Martín Medina, Félix Valencia, and Josefina Tapia. Removal of inorganic mercury from polluted water using structured nanoparticles. *Journal of Environmental Engineering*, 132(3):342–349, 2006.

[14] Kiril Hristovski, Andrew Baumgardner, and Paul Westerhoff. Selecting metal oxide nanomaterials for arsenic removal in fixed bed columns: from nanopowders to aggregated nanoparticle media. *Journal of Hazardous Materials*, 147(1-2):265–274, 2007.

[15] Tanapon Phenrat, Navid Saleh, Kevin Sirk, Robert D. Tilton, and Gregory V. Lowry. Aggregation and sedimentation of aqueous nanoscale zerovalent iron dispersions. *Environmental Science & Technology*, 41(1):284–290, 2007.

[16] Arturo A. Keller, Hongtao Wang, Dongxu Zhou, Hunter S. Lenihan, Gary Cherr, Bradley J. Cardinale, Robert Miller, and Zhaoxia Ji. Stability and aggregation of metal oxide nanoparticles in natural aqueous matrices. *Environmental Science & Technology*, 44(6):1962–1967, 2010.

[17] Yiyang Lin, Yan Qiao, Yijie Wang, Yun Yan, and Jianbin Huang. Self-assembled laminated nanoribbon-directed synthesis of noble metallic nanoparticle-decorated silica nanotubes and their catalytic applications. *Journal of Materials Chemistry*, 22(35): 18314–18320, 2012.

[18] Feng Lu and Didier Astruc. Nanocatalysts and other nanomaterials for water remediation from organic pollutants. *Coordination Chemistry Reviews*, 408:213180, 2020.

[19] Sujoy B. Roy and David A Dzombak. Chemical factors influencing colloid-facilitated transport of contaminants in porous media. *Environmental Science & Technology*, 31 (3):656–664, 1997.

[20] Andrea Franzetti, Paolo Caredda, Claudio Ruggeri, Paolo La Colla, Elena Tamburini, Maddalena Papacchini, and Giuseppina Bestetti. Potential applications of surface active compounds by Gordonia sp. strain BS29 in soil remediation technologies. *Chemosphere*, 75(6):801–807, 2009.

[21] Andrea Franzetti, Elena Tamburini, and Ibrahim M. Banat. Applications of biological surface active compounds in remediation technologies. In *Biosurfactants*, pages 121–134. Springer, 2010.

[22] Luky Hendraningrat, Shidong Li, and Ole Torsæter. A coreflood investigation of nanofluid enhanced oil recovery. *Journal of Petroleum Science and Engineering*, 111: 128–138, 2013.

[23] Osamah A. Alomair, Khaled M. Matar, and Yousef H. Alsaeed. Nanofluids application for heavy oil recovery. In *SPE Asia Pacific Oil & Gas Conference and Exhibition*. Society of Petroleum Engineers, 2014.

[24] Adel M. Salem Ragab and Ahmed E. Hannora. A Comparative investigation of nano particle effects for improved oil recovery–experimental work. In *SPE Kuwait Oil and Gas Show and Conference*. Society of Petroleum Engineers, 2015.

[25] Massimiliano Magro, Stefania Domeneghetti, Davide Baratella, Petr Jakubec, Gabriella Salviulo, Emanuela Bonaiuto, Paola Venier, Ondřej Malina, Jiří Tuček, Václav Ranc, Giorgio Zoppellaro, Radek Zbořil, and Fabio Vianello. Colloidal Surface Active Maghemite Nanoparticles for Biologically Safe Cr^{VI} Remediation: from Core-Shell Nanostructures to Pilot Plant Development. *Chemistry–A European Journal*, 22(40):14219–14226, 2016.

[26] Xiaofei Sun, Yanyu Zhang, Guangpeng Chen, and Zhiyong Gai. Application of nanoparticles in enhanced oil recovery: a critical review of recent progress. *Energies*, 10(3):345, 2017.

[27] Shidong Li, Mindaugas Genys, Kun Wang, and Ole Torsæter. Experimental study of wettability alteration during nanofluid enhanced oil recovery process and its effect on oil recovery. In *Society of Petroleum Engineers - SPE Reservoir Characterisation and Simulation Conference and Exhibition, RCSC 2015*, 2015. ISBN 9781510813427. doi: 10.2118/175610-ms.

[28] Kirti Kondiparty, Alex Nikolov, Stanley Wu, and Darsh Wasan. Wetting and spreading of nanofluids on solid surfaces driven by the structural disjoining pressure: statics analysis and experiments. *Langmuir*, 27(7):3324–3335, 2011.

[29] Hua Zhang, Alex Nikolov, and Darsh Wasan. Enhanced oil recovery (EOR) using nanoparticle dispersions: underlying mechanism and imbibition experiments. *Energy & Fuels*, 28(5):3002–3009, 2014.

[30] Florian Kuhnen, Kurt Barmettler, Subir Bhattacharjee, Menachem Elimelech, and Ruben Kretzschmar. Transport of iron oxide colloids in packed quartz sand media: monolayer and multilayer deposition. *Journal of Colloid and Interface Science*, 231(1): 32–41, 2000.

[31] Mark R. Wiesner, Mae C. Grant, and Stephen R. Hutchins. Reduced permeability in groundwater remediation systems: Role of mobilized colloids and injected chemicals. *Environmental Science & Technology*, 30(11):3184–3191, 1996.

[32] Cheng Chen, Aaron I. Packman, and Jean-François Gaillard. Pore-scale analysis of permeability reduction resulting from colloid deposition. *Geophysical Research Letters*, 35(7), 2008.

[33] Faruk Civan. Non-isothermal permeability impairment by fines migration and deposition in porous media including dispersive transport. *Transport in Porous Media*, 85 (1):233–258, 2010.

[34] Luky Hendraningrat, Bjørnar Engeset, Suwarno Suwarno, Shidong Li, and Ole Torsæter. Laboratory investigation of porosity and permeability impairment in Berea sandstones due to hydrophilic nanoparticle retention. In *Paper SCA2013-062 presented at the International Symposium of the Society of Core Analysts held in Napa Valley, California, USA*, pages 16–19, 2013.

[35] Scott A. Bradford and Saeed Torkzaban. Colloid transport and retention in unsaturated porous media: A review of interface-, collector-, and pore-scale processes and models. *Vadose Zone Journal*, 7(2):667–681, 2008.

[36] Wei Zhang, Verónica L. Morales, M. Ekrem Cakmak, Anthony E. Salvucci, Larry D. Geohring, Anthony G. Hay, Jean-Yves Parlange, and Tammo S. Steenhuis. Colloid transport and retention in unsaturated porous media: Effect of colloid input concentration. *Environmental Science & Technology*, 44(13):4965–4972, 2010.

[37] Furqan Le-Hussain, Abbas Zeinijahromi, Pavel G. Bedrikovetsky, Alexander Badalyan, Themis Carageorgos, and Yildiray Cinar. An experimental study of improved oil recovery through fines-assisted waterflooding. *Journal of Petroleum Science and Engineering*, 109:187–197, 2013.

[38] Nanotechnology in Environmental Applications: The Global Market. Technical report, BCC Publishing, 2015.

[39] Global Markets for Environmental Remediation Technologies. Technical report, BCC Publishing, 2021.

[40] Leah J. Matheson and Paul G. Tratnyek. Reductive dehalogenation of chlorinated methanes by iron metal. *Environmental Science & Technology*, 28(12):2045–2053, 1994.

[41] Mauricio A.V. Ramos, Weile Yan, Xiao-qin Li, Bruce E. Koel, and Wei-xian Zhang. Simultaneous oxidation and reduction of arsenic by zero-valent iron nanoparticles: understanding the significance of the core- shell structure. *The Journal of Physical Chemistry C*, 113(33):14591–14594, 2009.

[42] Tanapon Phenrat, Hye-Jin Kim, Fritjof Fagerlund, Tissa Illangasekare, Robert D Tilton, and Gregory V Lowry. Particle size distribution, concentration, and magnetic attraction affect transport of polymer-modified feo nanoparticles in sand columns. *Environmental Science & Technology*, 43(13):5079–5085, 2009.

[43] Hans Sonntag, Klaus Strenge, and Brain Vincent. Structure formation in disperse systems. *Coagulation Kinetics and Structure Formation*, pages 127–182, 1987.

[44] Tanapon Phenrat, Navid Saleh, Kevin Sirk, Hye-Jin Kim, Robert D. Tilton, and Gregory V. Lowry. Stabilization of aqueous nanoscale zerovalent iron dispersions by anionic polyelectrolytes: adsorbed anionic polyelectrolyte layer properties and their effect on aggregation and sedimentation. *Journal of Nanoparticle Research*, 10:795–814, 2008.

[45] Hye-Jin Kim, Tanapon Phenrat, Robert D. Tilton, and Gregory V. Lowry. Fe^0 nanoparticles remain mobile in porous media after aging due to slow desorption of polymeric surface modifiers. *Environmental Science & Technology*, 43(10):3824–3830, 2009.

[46] Tanapon Phenrat, Fritjof Fagerlund, Tissa Illangasekare, Gregory V. Lowry, and Robert D. Tilton. Polymer-Modified Fe^0 Nanoparticles Target Entrapped NAPL

in Two Dimensional Porous Media: Effect of Particle Concentration, NAPL Saturation, and Injection Strategy. *Environmental Science & Technology*, 45(14):6102–6109, 2011.

[47] Feng He, Dongye Zhao, Juncheng Liu, and Christopher B. Roberts. Stabilization of fe–pd nanoparticles with sodium carboxymethyl cellulose for enhanced transport and dechlorination of trichloroethylene in soil and groundwater. *Industrial & Engineering Chemistry Research*, 46(1):29–34, 2007.

[48] Richard L. Johnson, Graham O'Brien Johnson, James T. Nurmi, and Paul G. Tratnyek. Natural organic matter enhanced mobility of nano zerovalent iron. *Environmental Science & Technology*, 43(14):5455–5460, 2009.

[49] Trishikhi Raychoudhury, Nathalie Tufenkji, and Subhasis Ghoshal. Aggregation and deposition kinetics of carboxymethyl cellulose-modified zero-valent iron nanoparticles in porous media. *Water Research*, 46(6):1735–1744, 2012.

[50] Denis O'Carroll, Brent Sleep, Magdalena Krol, Hardiljeet Boparai, and Christopher Kocur. Nanoscale zero valent iron and bimetallic particles for contaminated site remediation. *Advances in Water Resources*, 51:104–122, 2013.

[51] Adriana Zaleska-Medynska, Martyna Marchelek, Magdalena Diak, and Ewelina Grabowska. Noble metal-based bimetallic nanoparticles: the effect of the structure on the optical, catalytic and photocatalytic properties. *Advances in Colloid and Interface Science*, 229:80–107, 2016.

[52] Zhong-Jie Jiang, Chun-Yan Liu, and Lu-Wei Sun. Catalytic properties of silver nanoparticles supported on silica spheres. *The Journal of Physical Chemistry B*, 109 (5):1730–1735, 2005.

[53] Rui Liu, Chris Sosa, Yao-Wen Yeh, Fengli Qu, Nan Yao, Robert K. Prud'Homme, and Rodney D. Priestley. A one-step and scalable production route to metal nanocatalyst supported polymer nanospheres via flash nanoprecipitation. *Journal of Materials Chemistry A*, 2(41):17286–17290, 2014.

[54] Gang-Wei Wu, Shao-Bin He, Hua-Ping Peng, Hao-Hua Deng, Ai-Lin Liu, Xin-Hua Lin, Xing-Hua Xia, and Wei Chen. Citrate-capped platinum nanoparticle as a smart probe for ultrasensitive mercury sensing. *Analytical Chemistry*, 86(21):10955–10960, 2014.

[55] Sadanand Pandey and Shivani B. Mishra. Catalytic reduction of p-nitrophenol by using platinum nanoparticles stabilised by guar gum. *Carbohydrate Polymers*, 113: 525–531, 2014.

[56] Alberto Tiraferri, Kai Loon Chen, Rajandrea Sethi, and Menachem Elimelech. Reduced aggregation and sedimentation of zero-valent iron nanoparticles in the presence of guar gum. *Journal of Colloid and Interface Science*, 324(1-2):71–79, 2008.

[57] Aishuang Xiang, Weile Yan, Bruce E Koel, and Peter R Jaffé. Poly (acrylic acid) coating induced 2-line ferrihydrite nanoparticle transport in saturated porous media. *Journal of Nanoparticle Research*, 15:1–9, 2013.

[58] Weile Yan, Hsing-Lung Lien, Bruce E. Koel, and Weixian Zhang. Iron nanoparticles for environmental clean-up: Recent developments and future outlook. *Environmental Science: Processes & Impacts*, 15(1):63–77, 2013.

[59] Aishuang Xiang, Sheng Zhou, Bruce E. Koel, and Peter R. Jaffé. Transport of Poly(Acrylic Acid) Coated 2-Line Ferrihydrite Nanoparticles in Saturated Aquifer Sediments for Environmental Remediation. *Journal of Nanoparticle Research*, 16: 2294, 2014.

[60] Anna C. Balazs, Todd Emrick, and Thomas P. Russell. Nanoparticle polymer composites: Where two small worlds meet. *Science*, 314(5802):1107–1110, 2006.

[61] Matti M. Van Schooneveld, Alexandre Gloter, Odile Stephan, Luiz F. Zagonel, Rolf Koole, Andries Meijerink, Willem J.M. Mulder, and Frank M.F. De Groot. Imaging and quantifying the morphology of an organic–inorganic nanoparticle at the subnanometre level. *Nature Nanotechnology*, 5(7):538–544, 2010.

[62] Shanghua Li, Meng Meng Lin, Muhammet S Toprak, Do Kyung Kim, and Mamoun Muhammed. Nanocomposites of polymer and inorganic nanoparticles for optical and magnetic applications. *Nano Reviews*, 1(1):5214, 2010.

[63] Yiyong Mai and Adi Eisenberg. Selective localization of preformed nanoparticles in morphologically controllable block copolymer aggregates in solution. *Accounts of Chemical Research*, 45(10):1657–1666, 2012.

[64] Yi Yi, Lucero Sanchez, Yuan Gao, and Yan Yu. Janus particles for biological imaging and sensing. *Analyst*, 141(12):3526–3539, 2016.

[65] Choon Woo Lim and In Su Lee. Magnetically recyclable nanocatalyst systems for the organic reactions. *Nano Today*, 5(5):412–434, 2010.

[66] Martin A.M. Gijs, Frederic Lacharme, and Ulrike Lehmann. Microfluidic applications of magnetic particles for biological analysis and catalysis. *Chemical Reviews*, 110 (3):1518–1563, 2010.

[67] Yunqing Zhu, Lang Fan, Bo Yang, and Jianzhong Du. Multifunctional homopolymer vesicles for facile immobilization of gold nanoparticles and effective water remediation. *ACS Nano*, 8(5):5022–5031, 2014.

[68] Elad Gross, F. Dean Toste, and Gabor A. Somorjai. Polymer-encapsulated metallic nanoparticles as a bridge between homogeneous and heterogeneous catalysis. *Catalysis Letters*, 145(1):126–138, 2015.

[69] Seung-Man Yang, Shin-Hyun Kim, Jong-Min Lim, and Gi-Ra Yi. Synthesis and assembly of structured colloidal particles. *Journal of Materials Chemistry*, 18(19): 2177–2190, 2008.

[70] Alessandro Ianiro, Hanglong Wu, Mark M.J. van Rijt, M. Paula Vena, Arthur D.A. Keizer, A. Caterina C. Esteves, Remco Tuinier, Heiner Friedrich, Nico A.J.M. Sommerdijk, and Joseph P. Patterson. Liquid–liquid phase separation during amphiphilic self-assembly. *Nature Chemistry*, 11(4):320–328, 2019.

[71] Chin Ken Wong, Xiaolian Qiang, Axel H.E. Müller, and André H. Gröschel. Self-assembly of block copolymers into internally ordered microparticles. *Progress in Polymer Science*, 102:101211, 2020.

[72] Takeshi Higuchi, Atsunori Tajima, Hiroshi Yabu, and Masatsugu Shimomura. Spontaneous formation of polymer nanoparticles with inner micro-phase separation structures. *Soft Matter*, 4(6):1302–1305, 2008.

[73] June Huh, Ji Young Jung, Jea Uk Lee, Heesook Cho, Soojin Park, Cheolmin Park, and Won Ho Jo. Supramolecular assembly of end-functionalized polymer mixtures confined in nanospheres. *ACS Nano*, 5(1):115–122, 2011.

[74] Hiroshi Yabu. Self-organized precipitation: an emerging method for preparation of unique polymer particles. *Polymer Journal*, 45(3):261–268, 2013.

[75] Hiroshi Yabu. Fabrication of nanostructured composite microspheres based on the self-assembly of polymers and functional nanomaterials. *Particle & Particle Systems Characterization*, 36(9):1900178, 2019.

[76] Victoria E. Lee, Chris Sosa, Rui Liu, Robert K. Prud'homme, and Rodney D. Priestley. Scalable platform for structured and hybrid soft nanocolloids by continuous precipitation in a confined environment. *Langmuir*, 33(14):3444–3449, 2017.

[77] Chris Sosa, Victoria E. Lee, Lorena S. Grundy, Mary J. Burroughs, Rui Liu, Robert K. Prud'homme, and Rodney D. Priestley. Combining precipitation and vitrification to control the number of surface patches on polymer nanocolloids. *Langmuir*, 33(23): 5835–5842, 2017.

[78] Lorena S. Grundy, Victoria E. Lee, Nannan Li, Chris Sosa, William D. Mulhearn, Rui Liu, Richard A. Register, Arash Nikoubashman, Robert K. Prud'homme, Athanassios Z. Panagiotopoulos, and Rodney D. Priestley. Rapid production of internally structured colloids by flash nanoprecipitation of block copolymer blends. *ACS Nano*, 12(5):4660–4668, 2018.

[79] Joseph Kao, Kari Thorkelsson, Peter Bai, Benjamin J. Rancatore, and Ting Xu. Toward functional nanocomposites: Taking the best of nanoparticles, polymers, and small molecules. *Chemical Society Reviews*, 42(7):2654–2678, 2013.

[80] Dasheng Gao, Ningning Liu, Weiwei Li, and Yide Han. Fabrication of nanoporous polymeric crystalline TiO_2 composite for photocatalytic degradation of aqueous organic pollutants under visible light irradiation. *Applied Organometallic Chemistry*, 32 (3):e4119, 2018.

[81] Rituparna Duarah and Niranjan Karak. Hyperbranched polyurethane/reduced carbon dot-zinc oxide nanocomposite-mediated solar-assisted photocatalytic degradation of organic contaminant: An approach towards environmental remediation. *Chemical Engineering Journal*, 370:716–728, 2019.

[82] J. Zeng, C. Peng, X. Wang, R. Wang, N. Zhang, and S. Xiong. One-pot self-assembled TiO_2/graphene/poly (acrylamide) superporous hybrid for photocatalytic degradation of organic pollutants. *Journal of Applied Polymer Science*, 136(5):47033, 2019.

[83] Roy Shenhar, Tyler B. Norsten, and Vincent M. Rotello. Polymer-mediated nanoparticle assembly: Structural control and applications. *Advanced Materials*, 17(6):657–669, 2005.

[84] Jia Tian, Jie Jin, Fan Zheng, and Hanying Zhao. Self-assembly of gold nanoparticles and polystyrene: A highly versatile approach to the preparation of colloidal particles with polystyrene cores and gold nanoparticle coronae. *Langmuir*, 26(11):8762–8768, 2010.

[85] Chuanbo Gao, Fenglei Lyu, and Yadong Yin. Encapsulated metal nanoparticles for catalysis. *Chemical Reviews*, 121(2):834–881, 2021.

[86] Hiroshi Yabu, Kazutaka Koike, Kiwamu Motoyoshi, Takeshi Higuchi, and Masatsugu Shimomura. Preparation of core–shell organic–inorganic nanocomposite particles based on phase separation of a polymer blend. *Chemistry Letters.*, 38(10):964–965, 2009.

[87] Hiroshi Yabu, Kazutaka Koike, Kiwamu Motoyoshi, Takeshi Higuchi, and Masatsugu Shimomura. A novel route for fabricating metal-polymer composite nanoparticles with phase-separated structures. *Macromolecules Rapid Communication*, 31(14): 1267–1271, 2010.

[88] Hiroshi Yabu, Tatsuya Jinno, Kazutaka Koike, Takeshi Higuchi, and Masatsugu Shimomura. Nanoparticle arrangements in block copolymer particles with microphase-separated structures. *Journal of Polymer Science B: Polymer Physics*, 49(24):1717–1722, 2011.

[89] Brian K. Johnson and Robert K. Prud'homme. Flash nanoprecipitation of organic actives and block copolymers using a confined impinging jets mixer. *Australian Journal of Chemistry*, 56(10):1021–1024, 2003.

[90] Chris Sosa, Rui Liu, Christina Tang, Fengli Qu, Sunny Niu, Martin Z. Bazant, Robert K. Prud'homme, and Rodney D. Priestley. Soft multifaced and patchy colloids by constrained volume self-assembly. *Macromolecules*, 49(9):3580–3585, 2016.

[91] Yasuyuki Kusaka, Duval Jérôme F.L., and Yashisa Adachi. Morphology and breaking of latex particle deposits at a cylindrical collector in a microfluidic chamber. *Environmental Science & Technology*, 44(24):9413–9418, 2010.

[92] Augustin Charvet, Loïc Wingert, Nathalie Bardin-Monnier, Stéphanie Pacault, Charlotte Godoy, Quentin Ribeyre, and Dominique Thomas. Visualization of airborne nanoparticle deposits onto spherical collectors. *Separation and Purification Technology*, 172:119–129, 2017.

[93] Emilie Dressaire and Alban Sauret. Clogging of microfluidic systems. *Soft Matter*, 13 (1):37–48, 2017.

[94] Maria Auset and Arturo A. Keller. Pore-scale visualization of colloid straining and filtration in saturated porous media using micromodels. *Water Resources Research*, 42(12), 2006.

[95] Hans M. Wyss, Daniel L. Blair, Jeffrey F. Morris, Howard A. Stone, and David A. Weitz. Mechanism for clogging of microchannels. *Physical Review E*, 74(6):061402, 2006.

[96] Matthieu Robert de Saint Vincent, Manouk Abkarian, and Hervé Tabuteau. Dynamics of colloid accumulation under flow over porous obstacles. *Soft Matter*, 12(4): 1041–1050, 2016.

[97] Yu-Jiun Lin, Peng He, Mohammad Tavakkoli, Nevin Thunduvila Mathew, Yap Yit Fatt, John C. Chai, Afshin Goharzadeh, Francisco M. Vargas, and Sibani Lisa Biswal. Examining asphaltene solubility on deposition in model porous media. *Langmuir*, 32 (34):8729–8734, 2016.

[98] Yu-Jiun Lin, Peng He, Mohammad Tavakkoli, Nevin Thunduvila Mathew, Yap Yit Fatt, John C. Chai, Afshin Goharzadeh, Francisco M. Vargas, and Sibani Lisa Biswal. Characterizing asphaltene deposition in the presence of chemical dispersants in porous media micromodels. *Energy & Fuels*, 31(11):11660–11668, 2017.

[99] Scott A. Bradford, Jirka Simunek, Mehdi Bettahar, Yadata F. Tadassa, Martinus T. van Genuchten, and Scott R. Yates. Straining of colloids at textural interfaces. *Water Resources Research*, 41(10), 2005.

[100] Scott A. Bradford, Saeed Torkzaban, and Sharon L. Walker. Coupling of physical and chemical mechanisms of colloid straining in saturated porous media. *Water Research*, 41(13):3012–3024, 2007.

[101] Charmaine Q. Qiu, Jie Han, Hui Gao, Lian-Ping Wang, and Yan Jin. Pore-scale numerical and experimental investigation of colloid retention at the secondary energy minimum. *Vadose Zone Journal*, 11(1), 2012.

[102] Wanyi Fu, Likun Hua, and Wen Zhang. Experimental and modeling assessment of the roles of hydrophobicity and zeta potential in chemically modified poly (ether sulfone) membrane fouling kinetics. *Industrial & Engineering Chemistry Research*, 56(30): 8580–8589, 2017.

[103] Jikang Shen and Rui Ni. Experimental investigation of clogging dynamics in homogeneous porous medium. *Water Resources Research*, 53(3):1879–1890, 2017.

[104] Carlo Bianco, Janis Eneida Patiño Higuita, Tiziana Tosco, Alberto Tiraferri, and Rajandrea Sethi. Controlled deposition of particles in porous media for effective aquifer nanoremediation. *Scientific Reports*, 7(1):1–10, 2017.

[105] Sujit S. Datta, T.S. Ramakrishnan, and David A. Weitz. Mobilization of a trapped non-wetting fluid from a three-dimensional porous medium. *Physics of Fluids*, 26(2): 022002, 2014.

[106] Xiqing Li, Chen-Luh Lin, Jan D. Miller, and William P. Johnson. Pore-scale observation of microsphere deposition at grain-to-grain contacts over assemblage-scale porous media domains using X-ray microtomography. *Environmental Science & Technology*, 40(12):3762–3768, 2006.

[107] Gaetan Gerber, Stéphane Rodts, Patrick Aimedieu, Pamela Faure, and Philippe Coussot. Particle-size-exclusion clogging regimes in porous media. *Physical Review Letters*, 120(14):148001, 2018.

[108] Xiqing Li, Pengfei Zhang, C.L. Lin, and William P. Johnson. Role of hydrodynamic drag on microsphere deposition and re-entrainment in porous media under unfavorable conditions. *Environmental Science & Technology*, 39(11):4012–4020, 2005.

[109] Sébastien Wiederseiner, Nicolas Andreini, Gaël Epely-Chauvin, and Christophe Ancey. Refractive-index and density matching in concentrated particle suspensions: a review. *Experiments in Fluids*, 50:1183–1206, 2011.

[110] Joshua A. Dijksman, Frank Rietz, Kinga A. Lőrincz, Martin Van Hecke, and Wolfgang Losert. Invited article: Refractive index matched scanning of dense granular materials. *Review of Scientific Instruments*, 83(1):011301, 2012.

[111] Ursula S. McKnight, Simon G. Funder, Jes J. Rasmussen, Michael Finkel, Philip J. Binning, and Poul L. Bjerg. An integrated model for assessing the risk of TCE groundwater contamination to human receptors and surface water ecosystems. *Ecological Engineering*, 36(9):1126–1137, 2010.

[112] Hugh H. Russell, John E. Matthews, and W. Sewell Guy. TCE removal from contaminated soil and groundwater. *EPA Environmental Engineering Sourcebook*, pages 87–100, 1992.

[113] M. Yavuz Corapcioglu and Shiyan Jiang. Colloid-facilitated groundwater contaminant transport. *Water Resources Research*, 29(7):2215–2226, 1993.

[114] Lis Wollesen de Jonge, Charlotte Kjærgaard, and P. Moldrup. Colloids and colloid-facilitated transport of contaminants in soils: An introduction. *Vadose Zone Journal*, 3(2):321–325, 2004.

[115] Haiyang Yu, Youwei He, Peng Li, Shuang Li, Tiantian Zhang, Elena Rodriguez-Pin, Song Du, Chenglong Wang, Shiqing Cheng, Christopher W. Bielawski, Steven L. Bryant, and Chun Huh. Flow enhancement of water-based nanoparticle dispersion through microscale sedimentary rocks. *Scientific Reports*, 5:8702, 2015.

[116] Daylin Liu, Philip R. Johnson, and Menachem Elimelech. Colloid deposition dynamics in flow-through porous media: Role of electrolyte concentration. *Environmental Science & Technology*, 29(12):2963–2973, 1995.

[117] Frank-Andreas Weber, Andreas Voegelin, Ralf Kaegi, and Ruben Kretzschmar. Contaminant mobilization by metallic copper and metal sulphide colloids in flooded soil. *Nature Geoscience*, 2(4):267–271, 2009.

[118] A.B. Kersting, D.W. Efurd, D.L. Finnegan, D.J. Rokop, D.K. Smith, and J.L. Thompson. Migration of plutonium in ground water at the Nevada Test Site. *Nature*, 397 (6714):56–59, 1999.

[119] Joseph N. Ryan and Menachem Elimelech. Colloid mobilization and transport in groundwater. *Colloids and Surfaces A: Physicochemical and Engineering Aspects*, 107: 1–56, 1996.

[120] William P. Johnson and Markus Hilpert. Upscaling colloid transport and retention under unfavorable conditions: Linking mass transfer to pore and grain topology. *Water Resources Research*, 49(9):5328–5341, 2013.

[121] Gaétan Gerber, M. Bensouda, David A. Weitz, and Philippe Coussot. Self-limited accumulation of colloids in porous media. *Physical Review Letters*, 123(15):158005, 2019.

[122] Kurt VanNess, Anna Rasmuson, Cesar A. Ron, and William P. Johnson. A unified force and torque balance for colloid transport: Predicting attachment and mobilization under favorable and unfavorable conditions. *Langmuir*, 35(27):9061–9070, 2019.

[123] Robin Jäger, Miller Mendoza, and Hans Jürgen Herrmann. Channelization in porous media driven by erosion and deposition. *Physical Review E*, 95(1):013110, 2017.

[124] Amber T. Krummel, Sujit S. Datta, Stefan Münster, and David A. Weitz. Visualizing multiphase flow and trapped fluid configurations in a model three-dimensional porous medium. *AIChE Journal*, 59(3):1022–1029, 2013.

[125] K.N. Pham, G. Petekidis, D. Vlassopoulos, S.U. Egelhaaf, W.C.K. Poon, and P.N. Pusey. Yielding behavior of repulsion-and attraction-dominated colloidal glasses. *Journal of Rheology*, 52(2):649–676, 2008.

[126] Filippo Bianchi, Marcel Thielmann, Lucilla De Arcangelis, and Hans Jürgen Herrmann. Critical bursts in filtration. *Physical Review Letters*, 120(3):034503, 2018.

[127] J.F. Schijven, H.A.M. De Bruin, S.M. Hassanizadeh, and A.M. de Roda Husman. Bacteriophages and clostridium spores as indicator organisms for removal of pathogens by passage through saturated dune sand. *Water Research*, 37(9):2186–2194, 2003.

[128] Xiao Zhao, Wen Liu, Zhengqing Cai, Bing Han, Tianwei Qian, and Dongye Zhao. An overview of preparation and applications of stabilized zero-valent iron nanoparticles for soil and groundwater remediation. *Water Research*, 100:245–266, 2016.

[129] Sushil Raj Kanel, Jean-Mark Greneche, and Heechul Choi. Arsenic (V) removal from groundwater using nanoscale zero-valent iron as a colloidal reactive barrier material. *Environmental Science & Technology*, 40(6):2045–2050, 2006.

[130] G Medici, L.J. West, and S.A. Banwart. Groundwater flow velocities in a fractured carbonate aquifer-type: implications for contaminant transport. *Journal of Contaminant Hydrology*, 222:1–16, 2019.

[131] A.C. Payatakes and Madalena M. Dias. Immiscible microdisplacement and ganglion dynamics in porous media. *Reviews in Chemical Engineering*, 2(2):85–174, 1984.

[132] R.C. Walker, C. Hofstee, J.H. Dane, and W.E. Hill. Surfactant enhanced removal of PCE in a nominally two-dimensional, saturated, stratified porous medium. *Journal of Contaminant Hydrology*, 34(1-2):17–30, 1998.

[133] A. Lashanizadegan, S.H. Ayatollahi, and H. Kazemi. Experimental and theoretical investigation of LNAPL movement in stratified media during soil remediation. *Environmental Technology*, 28(7):743–750, 2007.

[134] Benjamin Dersoir, Matthieu Robert de Saint Vincent, Manouk Abkarian, and Hervé Tabuteau. Clogging of a single pore by colloidal particles. *Microfluidics and Nanofluidics*, 19(4):953–961, 2015.

[135] R.I. Al-Raoush and C.S. Willson. Extraction of physically realistic pore network properties from three-dimensional synchrotron X-ray microtomography images of unconsolidated porous media systems. *Journal of Hydrology*, 300(1-4):44–64, 2005.

[136] Karsten E. Thompson, Clinton S. Willson, Christopher D. White, Stephanie Nyman, Janok P. Bhattacharya, and Allen H. Reed. Application of a new grain-based reconstruction algorithm to microtomography images for quantitative characterization and flow modeling. Technical report, Naval Research Lab Stennis Space Center MS Marine Geoacoustics Division, 2008.

[137] Gaétan Gerber, David A. Weitz, and Philippe Coussot. Propagation and adsorption of nanoparticles in porous medium as traveling waves. *Physical Review Research*, 2(3): 033074, 2020.

[138] R.J. Kouri and J. Sohlo. Liquid and gas flow patterns in random packings. *The Chemical Engineering Journal and the Biochemical Engineering Journal*, 61(2):95–105, 1996.

[139] Hannsjörg Freund, Thomas Zeiser, Florian Huber, Elias Klemm, Gunther Brenner, Franz Durst, and Gerhard Emig. Numerical simulations of single phase reacting flows in randomly packed fixed-bed reactors and experimental validation. *Chemical Engineering Science*, 58(3-6):903–910, 2003.

[140] Sujit S. Datta, Harry Chiang, T.S. Ramakrishnan, and David A. Weitz. Spatial fluctuations of fluid velocities in flow through a three-dimensional porous medium. *Physical Review Letters*, 111(6):064501, 2013.

[141] Alice Y.L. Huang, Michelle Y.F. Huang, Hervé Capart, and Rong-Her Chen. Optical measurements of pore geometry and fluid velocity in a bed of irregularly packed spheres. *Experiments in Fluids*, 45(2):309–321, 2008.

[142] Martin J. Blunt. *Multiphase flow in permeable media: A pore-scale perspective*. Cambridge University Press, 2017.

[143] Xavier Garcia, Lateef T. Akanji, Martin J. Blunt, Stephan K. Matthai, and John Paul Latham. Numerical study of the effects of particle shape and polydispersity on permeability. *Physical Review E*, 80(2):021304, 2009.

[144] Jacob Bear. *Dynamics of fluids in porous media*. American Elsevier Publishing, 1972.

[145] Ioannis Chatzis, Norman R. Morrow, and Hau T. Lim. Magnitude and detailed structure of residual oil saturation. *Society of Petroleum Engineers Journal*, 23(02): 311–326, 1983.

[146] Norman R. Morrow, I. Chatzis, J.J. Taber, et al. Entrapment and mobilization of residual oil in bead packs. *SPE Reservoir Engineering*, 3(03):927–934, 1988.

[147] R.J. Wygal. Construction of models that simulate oil reservoirs. *Society of Petroleum Engineers Journal*, 3(4):281–286, 1963.

[148] Jonathan T. Bartley and Douglas W. Ruth. Experimental investigation of unsteady-state relative permeability in sand-packs. In *Society of Core Analysis Conference*, volume 22, pages 1–14, 2001.

[149] Mohammad Ashrafi, Yaser Souraki, and Ole Torsaeter. Effect of temperature on athabasca type heavy oil–water relative permeability curves in glass bead packs. *Energy and Environment Research*, 2(2):113–126, 2012.

[150] Behzad Ghanbarian, Marios A. Ioannidis, and Allen G. Hunt. Theoretical insight into the empirical tortuosity-connectivity factor in the burdine-brooks-corey water relative permeability model. *Water Resources Research*, 53(12):10395–10410, 2017.

[151] J.J. Taber. Dynamic and static forces required to remove a discontinuous oil phase from porous media containing both oil and water. *Society of Petroleum Engineers Journal*, 9(3):11, 1969.

[152] Dinesh Ochhavlal Shah. *Improved oil recovery by surfactant and polymer flooding*. Elsevier, 2012.

[153] Francis A.L. Dullien. *Porous media: fluid transport and pore structure*. Academic press, 2012.

[154] Ioannis Chatzis and Francis A.L. Dullien. Application of the theory of percolation for a model of drainage in porous media and relative permeability of injected non-wetting fluids. *Oil & Gas Science and Technology–Revue d'IFP*, 37:183, 1982.

[155] Roland Lenormand, Cesar Zarcone, and A. Sarr. Mechanisms of the displacement of one fluid by another in a network of capillary ducts. *Journal of Fluid Mechanics*, 135: 337–353, 1983.

[156] Roland Lenormand, Eric Touboul, and Cesar Zarcone. Numerical models and experiments on immiscible displacements in porous media. *Journal of Fluid Mechanics*, 189:165–187, 1988.

[157] Jacob Bear. *Dynamics of fluids in porous media*. Courier Corporation, 2013.

[158] William E. Galloway and David K. Hobday. *Terrigenous clastic depositional systems: Applications to fossil fuel and groundwater resources*. Springer Science & Business Media, 2012.

[159] Sarah E. Gasda and Michael Anthony Celia. Upscaling relative permeabilities in a structured porous medium. *Advances in Water Resources*, 28(5):493–506, 2005.

[160] Hubert King, Michael Sansone, Pavel Kortunov, Ye Xu, Nicole Callen, Shreerang Chhatre, Hemant Sahoo, and Antonio Buono. Microstructural investigation of stress-dependent permeability in tight-oil rocks. *Petrophysics*, 59(01):35–43, 2018.

[161] Sujit S. Datta and David A. Weitz. Drainage in a model stratified porous medium. *Europhysics Letters*, 101(1):14002, 2013.

[162] M. Reyssat, L.Y. Sangne, E.A. Van Nierop, and Howard A. Stone. Imbibition in layered systems of packed beads. *Europhysics Letters*, 86(5):56002, 2009.

[163] Dengen Zhou, F.J. Fayers, and F.M. Orr Jr. Scaling of multiphase flow in simple heterogeneous porous media. *SPE Reservoir Engineering*, 12(03):173–178, 1997.

[164] Vito J. Zapata and Larry W. Lake. A theoretical analysis of viscous crossflow. In *SPE Annual Technical Conference and Exhibition*. Society of Petroleum Engineers, 1981.

[165] Emad W. Al-Shalabi and B. Ghosh. Effect of pore-scale heterogeneity and capillary-viscous fingering on commingled waterflood oil recovery in stratified porous media. *Journal of Petroleum Engineering*, 2016, 2016.

[166] A. P. Philipse and C. Pathmamanoharan. Liquid permeation (and sedimentation) of dense colloidal hard-sphere packings. *Journal of Colloida & Interface Science*, 159:96, 1993.

[167] K.S. Sorbie, Y.Z. Wu, and S.R. McDougall. The extended washburn equation and its application to the oil/water pore doublet problem. *Journal of Colloid and Interface Science*, 174(2):289–301, 1995.

[168] Nancy B. Lu, Amir A. Pahlavan, Christopher A. Browne, Daniel B. Amchin, Howard A. Stone, and Sujit S. Datta. Forced imbibition in stratified porous media. *Physical Review Applied*, 14(5):054009, 2020.

[169] Dietrich Stauffer. Scaling theory of percolation clusters. *Physics Reports*, 54(1):1–74, 1979.

[170] Joseph Hoshen, D. Stauffer, George H. Bishop, Ralph J. Harrison, and George D. Quinn. Monte carlo experiments on cluster size distribution in percolation. *Journal of Physics A: Mathematical and General*, 12(8):1285, 1979.

[171] D.S. Gaunt. Percolation exponent δp for lattice dimensionality $d \geq 3$. *Journal of Physics A: Mathematical and General*, 10(5):807, 1977.

[172] A. Georgiadis, S. Berg, A. Makurat, G. Maitland, and H. Ott. Pore-scale micro-computed-tomography imaging: Nonwetting-phase cluster-size distribution during drainage and imbibition. *Physical Review E*, 88(3):033002, 2013.

[173] Stefan Iglauer, Stefano Favretto, Gregorio Spinelli, Gianni Schena, and Martin J. Blunt. X-ray tomography measurements of power-law cluster size distributions for the nonwetting phase in sandstones. *Physical Review E*, 82(5):056315, 2010.

[174] Stefan Iglauer, Martin A. Fernø, Paul Shearing, and Martin J. Blunt. Comparison of residual oil cluster size distribution, morphology and saturation in oil-wet and water-wet sandstone. *Journal of Colloid and Interface Science*, 375(1):187–192, 2012.

[175] Abdus Satter and Ghulam M. Iqbal. Determination of oil and gas in place: conventional and unconventional reservoirs. *Reservoir Engineering*, pages 195–210, 2016.

[176] Wei Yu, HamidReza Lashgari, and Kamy Sepehrnoori. Simulation study of CO_2 huff-n-puff process in bakken tight oil reservoirs. In *SPE Western North American and Rocky Mountain Joint Meeting*. Society of Petroleum Engineers, 2014.

[177] Alan J. Rabideau and Cass T. Miller. Two-dimensional modeling of aquifer remediation influenced by sorption nonequilibrium and hydraulic conductivity heterogeneity. *Water Resources Research*, 30(5):1457–1470, 1994.

[178] Jeremy Ingham. *Geomaterials under the microscope: a colour guide*. CRC Press, 2010.

[179] Yukie Tanino and Martin J. Blunt. Capillary trapping in sandstones and carbonates: Dependence on pore structure. *Water Resources Research*, 48(8), 2012.

[180] Sepideh Khodaparast, Minyoung Kevin Kim, Justin E. Silpe, and Howard A. Stone. Bubble-driven detachment of bacteria from confined microgeometries. *Environmental Science & Technology*, 51(3):1340–1347, 2017.

[181] Yingxian Estella Yu, Sepideh Khodaparast, and Howard A. Stone. Armoring confined bubbles in the flow of colloidal suspensions. *Soft Matter*, 13(15):2857–2865, 2017.

[182] Tianya Yin, Donglee Shin, Joelle Frechette, Carlos E. Colosqui, and German Drazer. Dynamic effects on the mobilization of a deposited nanoparticle by a moving liquid-liquid interface. *Physical Review Letters*, 121(23):238002, 2018.

[183] Deok-Hoon Jeong, Langqi Xing, Jean-Baptise Boutin, and Alban Sauret. Particulate suspension coating of capillary tubes. *Soft Matter*, 18(42):8124–8133, 2022.

[184] Craig M. Bethke, Jackie D. Reed, and Donald F. Oltz. Long-range petroleum migration in the illinois basin. *AAPG Bulletin*, 75(5):925–945, 1991.

[185] Bernard H. Kueper and Emil O. Frind. Two-phase flow in heterogeneous porous media: 1. model development. *Water Resources Research*, 27(6):1049–1057, 1991.

[186] Helen E. Dawson and Paul V. Roberts. Influence of viscous, gravitational, and capillary forces on DNAPL saturation. *Groundwater*, 35(2):261–269, 1997.

[187] Laurent C. Levy, Patricia J. Culligan, and John T. Germaine. Modelling of DNAPL behavior in vertical fractures. *International Journal of Physical Modelling in Geotechnics*, 3(1):01–18, 2003.

[188] Abhijit Y. Dandekar. *Petroleum reservoir rock and fluid properties*. CRC Press, 2006.

[189] Sally M. Benson and Franklin M. Orr. Carbon dioxide capture and storage. *MRS Bulletin*, 33(4):303–305, 2008.

[190] Luis Cueto-Felgueroso and Ruben Juanes. Nonlocal interface dynamics and pattern formation in gravity-driven unsaturated flow through porous media. *Physical Review Letters*, 101(24):244504, 2008.

[191] Jerome A. Neufeld and Herbert E. Huppert. Modelling carbon dioxide sequestration in layered strata. *Journal of Fluid Mechanics*, 625:353–370, 2009.

[192] Jacob Bear and Alexander H-D Cheng. *Modeling groundwater flow and contaminant transport*, volume 23. Springer, 2010.

[193] Christopher W. MacMinn, Michael Lawrence Szulczewski, and Ruben Juanes. CO_2 migration in saline aquifers. part 1. Capillary trapping under slope and groundwater flow. *Journal of Fluid Mechanics*, 662:329–351, 2010.

[194] Ehsan Saadatpoor, Steven L. Bryant, and Kamy Sepehrnoori. New trapping mechanism in carbon sequestration. *Transport in Porous Media*, 82:3–17, 2010.

[195] Uditha C. Bandara, Alexandre M. Tartakovsky, and Bruce J. Palmer. Pore-scale study of capillary trapping mechanism during CO_2 injection in geological formations. *International Journal of Greenhouse Gas Control*, 5(6):1566–1577, 2011.

[196] Muhammad Sahimi. *Flow and transport in porous media and fractured rock: from classical methods to modern approaches*. John Wiley & Sons, 2011.

[197] S. Berg and H. Ott. Stability of CO_2–brine immiscible displacement. *International Journal of Greenhouse Gas Control*, 11:188–203, 2012.

[198] Marcelo Carmo, David L. Fritz, Jürgen Mergel, and Detlef Stolten. A comprehensive review on PEM water electrolysis. *International Journal of Hydrogen Energy*, 38(12): 4901–4934, 2013.

[199] Chung Hyuk Lee, Rupak Banerjee, Faraz Arbabi, James Hinebaugh, and Aimy Bazylak. Porous transport layer related mass transport losses in polymer electrolyte membrane electrolysis: A review. In *International Conference on Nanochannels, Microchannels, and Minichannels*, volume 50343, page V001T07A003. American Society of Mechanical Engineers, 2016.

[200] Hanieh Bazyar, Pengyu Lv, Jeffery A/ Wood, Slawomir Porada, Detlef Lohse, and Rob G.H. Lammertink. Liquid–liquid displacement in slippery liquid-infused membranes (slims). *Soft Matter*, 14(10):1780–1788, 2018.

[201] Surachet Aramrak, Markus Flury, and James B. Harsh. Detachment of deposited colloids by advancing and receding air–water interfaces. *Langmuir*, 27(16):9985–9993, 2011.

[202] Markus Flury and Surachet Aramrak. Role of air-water interfaces in colloid transport in porous media: A review. *Water Resources Research*, 53(7):5247–5275, 2017.

[203] B.P. Binks and P.D.I. Fletcher. Particles adsorbed at the oil- water interface: A theoretical comparison between spheres of uniform wettability and "Janus" particles. *Langmuir*, 17(16):4708–4710, 2001.

[204] Chenliang Shi, Ling Lin, Yukun Yang, Wenjia Luo, Maoqing Deng, and Yujie Wu. Synthesis of aminated polystyrene and its self-assembly with nanoparticles at oil/water interface. *e-Polymers*, 20(1):317–327, 2020.

[205] S. Kutuzov, J. He, R. Tangirala, T. Emrick, T.P. Russell, and A. Böker. On the kinetics of nanoparticle self-assembly at liquid/liquid interfaces. *Physical Chemistry Chemical Physics*, 9(48):6351–6358, 2007.

[206] Kan Du, Elizabeth Glogowski, Todd Emrick, Thomas P. Russell, and Anthony D. Dinsmore. Adsorption energy of nano-and microparticles at liquid- liquid interfaces. *Langmuir*, 26(15):12518–12522, 2010.

[207] Venkateshwar Rao Dugyala, Jyothi Sri Muthukuru, Ethayaraja Mani, and Madivala G Basavaraj. Role of electrostatic interactions in the adsorption kinetics of nanoparticles at fluid–fluid interfaces. *Physical Chemistry Chemical Physics*, 18(7):5499–5508, 2016.

[208] Gunasekaran Dharanivasan, Thangavelu Rajamuthuramalingam, Denison Michael Immanuel Jesse, Nagappan Rajendiran, and Krishnan Kathiravan. Gold nanoparticles assisted characterization of amine functionalized polystyrene multiwell plate and glass slide surfaces. *Applied Nanoscience*, 5:39–50, 2015.

[209] J.C. Means and R. Wuayaratne. Role of natural colloids in the transport of hydrophobic pollutants. *Science*, 215(4535):968–970, 1982.

[210] E. Tipping and D.C. Higgins. The effect of adsorbed humic substances on the colloid stability of haematite particles. *Colloids and Surfaces*, 5(2):85–92, 1982.

[211] Ronald J. Gibbs. Effect of natural organic coatings on the coagulation of particles. *Environmental Science & Technology*, 17(4):237–240, 1983.

[212] Y. Ouyang, Dilip Shinde, R.S. Mansell, and W. Harris. Colloid-enhanced transport of chemicals in subsurface environments: A review. *Critical Reviews in Environmental Science and Technology*, 26(2):189–204, 1996.

[213] Sadok Feia, Jean Claude Dupla, Siavash Ghabezloo, Jean Sulem, Jean Canou, Atef Onaisi, Herbert Lescanne, and Eric Aubry. Experimental investigation of particle suspension injection and permeability impairment in porous media. *Geomechanics for Energy and the Environment*, 3:24–39, 2015.

[214] Lei Li, Yuliang Su, Yuting Lv, and Jiawei Tu. Asphaltene deposition and permeability impairment in shale reservoirs during CO_2 huff-n-puff EOR process. *Petroleum Science and Technology*, 38(4):384–390, 2020.

[215] Mark Knackstedt and Lincoln Paterson. Invasion percolation. *Complex Media and Percolation Theory*, pages 175–190, 2021.

[216] David Wilkinson and Jorge F. Willemsen. Invasion percolation: a new form of percolation theory. *Journal of Physics A: Mathematical and General*, 16(14):3365, 1983.

[217] Raymond P. Mayer and Robert A. Stowe. Mercury porosimetry—breakthrough pressure for penetration between packed spheres. *Journal of Colloid Science*, 20(8):893–911, 1965.

[218] Roland Lenormand and Cesar Zarcone. Invasion percolation in an etched network: measurement of a fractal dimension. *Physical Review Letters*, 54(20):2226, 1985.

[219] Geoffrey Mason and Norman Morrow. Meniscus displacement curvatures of a perfectly wetting liquid in capillary pore throats formed by spheres. *Journal of Colloid and Interface Science*, 109(1):46–56, 1986.

[220] Roland Lenormand and Cesar Zarcone. Capillary fingering: percolation and fractal dimension. *Transport in Porous Media*, 4:599–612, 1989.

[221] Nicos Martys, Marek Cieplak, and Mark O. Robbins. Critical phenomena in fluid invasion of porous media. *Physical Review Letters*, 66(8):1058, 1991.

[222] Knut Jørgen Måløy, Liv Furuberg, Jens Feder, and Torstein Jøssang. Dynamics of slow drainage in porous media. *Physical Review Letters*, 68(14):2161, 1992.

[223] Pedro G. Toledo, L.E. Scriven, and H. Ted Davis. Pore-space statistics and capillary pressure curves from volume-controlled porosimetry. *SPE Formation Evaluation*, 9 (01):46–54, 1994.

[224] B. Xu, Y.C. Yortsos, and D. Salin. Invasion percolation with viscous forces. *Physical Review E*, 57(1):739, 1998.

[225] Lei Xu, Simon Davies, Andrew B. Schofield, and David A. Weitz. Dynamics of drying in 3D porous media. *Physical Review Letters*, 101(9):094502, 2008.

[226] V. Joekar-Niasar and S.M. Hassanizadeh. Analysis of fundamentals of two-phase flow in porous media using dynamic pore-network models: A review. *Critical Reviews in Environmental Science and Technology*, 42(18):1895–1976, 2012.

[227] David Wilkinson. Percolation effects in immiscible displacement. *Physical Review A*, 34(2):1380, 1986.

[228] A. Birovljev, L. Furuberg, J. Feder, T. Jssang, K.J. Mly, and A. Aharony. Gravity invasion percolation in two dimensions: Experiment and simulation. *Physical Review Letters*, 67(5):584, 1991.

[229] Yder Masson. A fast two-step algorithm for invasion percolation with trapping. *Computers & Geosciences*, 90:41–48, 2016.

[230] Lucian Niemeyer, Luciano Pietronero, and Hans J. Wiesmann. Fractal dimension of dielectric breakdown. *Physical Review Letters*, 52(12):1033, 1984.

[231] Paul Meakin, Jens Feder, Vidar Frette, and Torstein Jøssang. Invasion percolation in a destabilizing gradient. *Physical Review A*, 46(6):3357, 1992.

[232] Roberto Nicolau Onody, A.N.D. Posadas, and S. Crestana. Experimental studies of the fingering phenomena in two dimensions and simulation using a modified invasion percolation model. *Journal of Applied Physics*, 78(5):2970–2976, 1995.

[233] Talal T. Al-Housseiny, Peichun A. Tsai, and Howard A. Stone. Control of interfacial instabilities using flow geometry. *Nature Physics*, 8(10):747–750, 2012.

[234] S.J. Jackson, H. Power, Donald Giddings, and D. Stevens. The stability of immiscible viscous fingering in hele-shaw cells with spatially varying permeability. *Computer Methods in Applied Mechanics and Engineering*, 320:606–632, 2017.

[235] Soumyajyoti Biswas, Paolo Fantinel, Oshri Borgman, Ran Holtzman, and Lucas Goehring. Drying and percolation in correlated porous media. *Physical Review Fluids*, 3(12):124307, 2018.

[236] Nancy B. Lu, Christopher A. Browne, Daniel B. Amchin, Janine K. Nunes, and Sujit S. Datta. Controlling capillary fingering using pore size gradients in disordered media. *Physical Review Fluids*, 4(8):084303, 2019.

[237] Nancy B Lu, Daniel B Amchin, and Sujit S Datta. Forced imbibition in stratified porous media: Fluid dynamics and breakthrough saturation. *Physical Review Fluids*, 6(11):114007, 2021.

[238] G.R. Jerauld and S.J. Salter. The effect of pore-structure on hysteresis in relative permeability and capillary pressure: pore-level modeling. *Transport in Porous Media*, 5 (2):103–151, 1990.

[239] John Turkevich, Peter Cooper Stevenson, and James Hillier. A study of the nucleation and growth processes in the synthesis of colloidal gold. *Discussions of the Faraday Society*, 11:55–75, 1951.

[240] Gerrit Frens. Controlled nucleation for the regulation of the particle size in monodisperse gold suspensions. *Nature Physical Science*, 241(105):20–22, 1973.

[241] Michael R. Ivanov, Heidi R. Bednar, and Amanda J. Haes. Investigations of the mechanism of gold nanoparticle stability and surface functionalization in capillary electrophoresis. *ACS Nano*, 3(2):386–394, 2009.

[242] Wim Van Aarle, Willem Jan Palenstijn, Jan De Beenhouwer, Thomas Altantzis, Sara Bals, K. Joost Batenburg, and Jan Sijbers. The astra toolbox: A platform for advanced algorithm development in electron tomography. *Ultramicroscopy*, 157:35–47, 2015.

[243] Varun Kumar and Robert K. Prud'homme. Nanoparticle stability: Processing pathways for solvent removal. *Chemical Engineering Science*, 64(6):1358–1361, 2009.

[244] Jinsong Tao, Shing Fung Chow, and Ying Zheng. Application of flash nanoprecipitation to fabricate poorly water-soluble drug nanoparticles. *Acta Pharmaceutica Sinica B*, 9(1):4–18, 2019.

[245] Arash Nikoubashman, Victoria E. Lee, Chris Sosa, Robert K. Prud'homme, Rodney D. Priestley, and Athanassios Z. Panagiotopoulos. Directed assembly of soft colloids through rapid solvent exchange. *ACS Nano*, 10(1):1425–1433, 2016.

[246] Robert F. Pagels, Jasmine Edelstein, Christina Tang, and Robert K. Prud'homme. Controlling and predicting nanoparticle formation by block copolymer directed rapid precipitations. *Nano Letters*, 18(2):1139–1144, 2018.

[247] Jason X. Liu, Navid Bizmark, Douglas M. Scott, Richard A. Register, Mikko P. Haataja, Sujit S. Datta, Craig B. Arnold, and Rodney D. Priestley. Evolution of polymer colloid structure during precipitation and phase separation. *JACS Au*, 1(7):936–944, 2021.

[248] Michael Rubinstein and Ralph H. Colby. *Polymer Physics*, volume 23. Oxford University Press New York, 2003.

[249] Hoang D. Lu, Paradorn Rummaneethorn, Kurt D. Ristroph, and Robert K. Prud'homme. Hydrophobic ion pairing of peptide antibiotics for processing into controlled release nanocarrier formulations. *Molecular Pharmaceutics*, 15(1):216–225, 2018.

[250] Kurt D. Ristroph and Robert K. Prud'homme. Hydrophobic ion pairing: Encapsulating small molecules, peptides, and proteins into nanocarriers. *Nanoscale Advances*, 1(11):4207–4237, 2019.

[251] William B. Haines. Studies in the physical properties of soil. v. the hysteresis effect in capillary properties, and the modes of moisture distribution associated therewith. *The Journal of Agricultural Science*, 20(1):97–116, 1930.

[252] Steffen Berg, Holger Ott, Stephan A. Klapp, Alex Schwing, Rob Neiteler, Niels Brussee, Axel Makurat, Leon Leu, Frieder Enzmann, Jens-Oliver Schwarz, Michael Kersten, Sarah Irvine, and Marco Stampanoni. Real-time 3d imaging of haines jumps in porous media flow. *Proceedings of the National Academy of Sciences*, 110(10):3755–3759, 2013.

[253] Mustafa Akbulut, Paul Ginart, Marian E. Gindy, Christian Theriault, Katherine H. Chin, Winston Soboyejo, and Robert K. Prud'Homme. Generic method of preparing multifunctional fluorescent nanoparticles using flash nanoprecipitation. *Advanced Functional Materials*, 19(5):718–725, 2009.

[254] Christopher A. Browne, Audrey Shih, and Sujit S. Datta. Pore-scale flow characterization of polymer solutions in microfluidic porous media. *Small*, 16(9):1903944, 2020.

[255] RG Larson, LE Scriven, and HT Davis. Percolation theory of residual phases in porous media. *Nature*, 268(5619):409–413, 1977.

[256] K.M. Ng, H.T. Davis, and L.E. Scriven. Visualization of blob mechanics in flow through porous media. *Chemical Engineering Science*, 33(8):1009–1017, 1978.

[257] K.M. Ng and A.C. Payatakes. Stochastic simulation of the motion, breakup and stranding of oil ganglia in water-wet granular porous media during immiscible displacement. *AIChE Journal*, 26(3):419–429, 1980.

[258] R.G. Larson, H.T. Davis, and L.E. Scriven. Displacement of residual nonwetting fluid from porous media. *Chemical Engineering Science*, 36(1):75–85, 1981.

[259] P. Amili and Y.C. Yortsos. Darcian dynamics: a new approach to the mobilization of a trapped phase in porous media. *Transport in Porous Media*, 64:25–49, 2006.

[260] A.C. Payatakes, K.M. Ng, and R.W. Flumerfelt. Oil ganglion dynamics during immiscible displacement: Model formulation. *AIChE Journal*, 26(3):430–443, 1980.

[261] N.C. Wardlaw and M. McKellar. Oil blob populations and mobilization of trapped oil in unconsolidated packs. *The Canadian Journal of Chemical Engineering*, 63(4): 525–532, 1985.

[262] Lirong Zhong, Alex Mayer, and Robert J. Glass. Visualization of surfactant-enhanced nonaqueous phase liquid mobilization and solubilization in a two-dimensional micromodel. *Water Resources Research*, 37(3):523–537, 2001.

[263] J.G. Roof. Snap-off of oil droplets in water-wet pores. *Society of Petroleum Engineers Journal*, 10(01):85–90, 1970.

This thesis was typeset using LaTeX, originally developed by Leslie Lamport and based on Donald Knuth's TeX. The body text is set in 11 point Egenolff-Berner Garamond, a revival of Claude Garamont's humanist typeface. A template that can be used to format a PhD thesis with this look and feel has been released under the permissive MIT (X11) license, and can be found online at github.com/suchow/Dissertate or from its author, Jordan Suchow, at suchow@post.harvard.edu.